PROJECTILE LINEAR THEORY FOR AERODYNAMICALLY ASYMMETRIC PROJECTILES

A Thesis
Presented to
The Academic Faculty

by

John W. Dykes

In Partial Fulfillment
of the Requirements for the Degree
Master of Science in the
School of Mechanical Engineering

Georgia Institute of Technology
December 2011

PROJECTILE LINEAR THEORY FOR AERODYNAMICALLY ASYMMETRIC PROJECTILES

Approved by:

Dr. Mark Costello, Committee Co-Chair
School of Aerospace Engineering
Georgia Institute of Technology

Dr. Ari Glezer, Committee Co-Chair
School of Mechanical Engineering
Georgia Institute of Technology

Dr. Wayne Whiteman
School of Mechanical Engineering
Georgia Institute of Technology

Date Approved: October 25, 2011

ACKNOWLEDGEMENTS

I would like to thank my advisor, Dr. Mark Costello for his guidance and support with this project. Many thanks for the opportunity and financial support, as well as knowledge, both engineering and otherwise.

This project would not have been possible without the support of Dr. Gene Cooper, Dr. Frank Fresconi, and Dr. Paul Weinacht of the U.S. Army Research Laboratory in Aberdeen Proving Ground, MD, to whom I am greatly indebted. Their efforts and advice were critical in much of the development of this research, and I hope they find it helpful in their own endeavors.

I would also like to thank my committee members, Dr. Ari Glezer and Dr. Wayne Whiteman, for their support, help, and encouragement. Additionally, I wish to express my gratitude to my friends and fellow grad researchers who provided abundant advice, help and encouragement: Fred Banser, Hannes Daepp, Jeff Kornuta, Edward Scheuermann, Emily Leylek, Luisa Fairfax, Carlos Montalvo, Jack Mooney, Michael Abraham, Michael Ward, Kyle French, Sam Zaravoy, Vasu Manivann, and Thomas Hermann.

Finally, I would like to acknowledge and thank my family and close friends for all the love and support: Bill, Theresa, Stephen, and Jennifer Dykes, Teresa Cotant, John Cunningham, and Katy Cunningham.

TABLE OF CONTENTS

LIST OF TABLES

LIST OF FIGURES

LIST OF SYMBOLS

$AR = b/c$	Lifting surface dimsionless aspect ratio
b	Lifting surface span length [ft]
c	lifting surface chord length [ft]
$C_{L_{C_i}}$,$C_{D_{C_i}}$	i^{th} lifting surface aerodynamic lift and drag coefficients
C_{D0}	Zero angle of attack lifting surface drag force coefficient
$C_{L\alpha}$	Lift curve slope coefficient of lifting surfaces
C_{LDD}	Roll-rate aerodynamic coefficient
C_{LP}	Roll-damping aerodynamic coefficient
C_{MQ}	Pitch-damping aerodynamic coefficient
C_{X0},C_{X2}	Axial force aerodynamic coefficients
C_{YPA}	Magnus force aerodynamic coefficient
C_{**}	Classic projectile linear theory coefficients
$\mathbb{C}_N(\cdot)$	Measure number vector operator for a coordinate system designated by N
D	Projectile reference diameter [ft]
e	Lifting surface computation point transverse location [ft]
f	Lifting surface computation point axial location [ft]
$\vec{F}$	Total externally applied force [lbf]
g	Gravitational constant [ft/sec]
I_N,J_N,K_N	Unit vectors for a coordinate system designated by N
I_R	Symmetric Projectile axial mass moment of inertia tensor [slug-ft^2]
I_P	Symmetric Projectile transverse mass moment of inertia tensor [slug-ft^2]
$\mathbf{I}$	Projectile mass moment of inertia tensor [slug-ft^2]
m	Projectile mass [slug]

$\vec{M}$	Total externally applied moment [ft-lbf]
Ma	Projectile Mach number
p,q,r	Projectile angular velocity components in the body reference frame [s^{-1}]
$\vec{r}_{O\to\oplus}$	Position vector from the origin of the inertial frame to projectile mass center [ft]
$\vec{r}_{\oplus\to COP}$	Position vector from the projectile mass center to the center of pressure [ft]
$\vec{r}_{\oplus\to MAC}$	Position vector from the projectile mass center to the Magnus aerodynamic center [ft]
$\vec{r}_{\oplus\to C_i}$	Position vector from the projectile mass center to the i^{th} lifting surface computation point [ft]
s	Dimensionless arc length independent variable
S_{C_i}	i^{th} lifting surface planform area [ft^2]
SoS	Atmospheric speed of sound [ft/sec]
$\mathbb{S}_N(\cdot)$	Vector cross-product operator in a coordinate system designated by N
$T = 2\pi/p_o$	Period of rotation for approximately constant roll rate p_o projectile [sec]
t	Time independent variable [sec]
$[\mathbf{T}_x(\gamma)]$	A single-axis transformation matrix about an axis x by angle γ
$[\mathbf{T}_{B\leftarrow I}]$	Transformation matrix from the inertial to the body frame
$[\mathbf{T}_{C_i\leftarrow B}]$	Transformation matrix from the body frame to the i^{th} lifting surface reference frame
V	Total Velocity [ft/sec]
$\vec{V}_{\oplus/I}$	Velocity vector of projectile mass center with respect to the inertial reference frame [ft/sec]

u,v,w	Mass center velocity components in the body reference frame [ft/sec]
u_{C_i},v_{C_i},w_{C_i}	i^{th} lifting surface center velocity components in the lifting surface reference frame [ft/sec]
x,y,z	Mass center position vector components in the inertial reference frame [ft]
α,β	Projectile angles of attack [deg]
α_{C_i}	i^{th} lifting surface aeridynamic angle of attack [deg]
δ_{C_i}	i^{th} lifting surface parameter cant angle [deg]
λ_j	Dynamic system j^{th} Eigenvalue
ρ	Atmospheric density [slug/ft^3]
ϕ_{C_i}	i^{th} lifting surface rotation angle about the $\vec{i}_B$ body axis [deg]
ϕ,θ,ψ	Projectile Euler roll, pitch, and yaw angles [deg]
$\vec{\omega}_{B/I}$	Angular velocity vector of the projectile body frame with respect to the inertial reference frame [rad/sec]

Superscripts

$\dot{x}$	Derivative of variable with respect to the independent variable t
x'	Derivative of variable with respect to the independent variable s
$\tilde{x}$	Variable is expressed in the no-roll reference frame
$\vec{x}$	A vector in 3-D space
$\mathbf{X}$	A matrix

LIST OF ABBREVIATIONS

B	Body-fixed reference frame
BL	Projectile buttline position component
C	Lifting surface aerodynamic model
C_i	i^{th} lifting surface reference frame
COP	Aerodynamic center of pressure
GNC	Guidance, Navigation, and Control
I	Inertial reference frame
LTI	Linear time-invariant dynamic model
LTP	Linear time-periodic dynamic model
M	Magnus aerodynamic force model
MAC	Magnus aerodynamic center
NR	No-roll reference frame
PLT	Projectile linear theory dynamic model
SA	Steady aerodynamic model
SL	Projectile stationline position component
UA	Unsteady aerodynamic model
W	Projectile weight
WL	Projectile waterline position component
6DOF	six-degree-of-freedom dynamic model

SUMMARY

Currently, there are few analytical tools within the ballistics community to aid in the design and performance evaluation of aerodynamically asymmetric projectiles. The scope of this thesis is to (1) create analytical tools that are capable of quantifying aerodynamically asymmetric projectile performance, (2) demonstrate the ability of these models to accurately account for aerodynamic asymmetries, and (3) gain insight into the flight mechanics of several aerodynamically asymmetric projectiles. First, a six-degree-of-freedom (6 DOF) flight dynamic model, which uses a point-force lifting-surface aerodynamic model, was developed to replicate flight characteristics observed from measured results of common projectiles. A quasi-linear flight dynamic model was then created using the machinery of Projectile Linear Theory (PLT). From this, flight dynamic stability models were developed for linear time-invariant (LTI) and linear time-periodic (LTP) systems. Dynamic simulation and stability trade studies were then conducted on asymmetric variants of 4-finned, 3-finned, 2-finned, and hybrid projectile configurations. First, stability of symmetric projectiles are validated and show that the classical and extended PLT model yielded identical results. Results show that aerodynamic asymmetries can sometimes cause instabilities and other times cause significant increase in dynamic mode damping and increase/decrease in mode frequency. Partially asymmetric (single plane) configurations were shown to cause epicyclic instabilities as the asymmetries became severe, while fully asymmetric (two plane) can grow unstable in either the epicyclic modes or the roll/yaw mode. Another significant result showed that the LTP stability model is able to capture aerodynamic lifting-surface periodic affects to evaluate dynamic stability requirements for asymmetric projectiles.

CHAPTER I

INTRODUCTION

1.1 Background and Motivation

A number of conditions can cause standard munitions such as mortars and artillery to miss an intended target. These conditions include variable atmospheric conditions, firing platform motion, aiming errors, and manufacturing inaccuracies of the gun tube, propellant, and projectile [35]. With the advent of smart weapons technologies, guided munitions can be used to dramatically lower dispersion error and collateral damage; however, development of these guided projectiles has presented weapons designers with numerous complex technical challenges over the past several decades [37]. Control mechanisms and onboard electronics suites must be small due to size limitations and rugged to withstand extreme acceleration loads and high spin rates. Furthermore, guided projectiles are often fired in large quantities and therefore must be relatively inexpensive to produce. To reduce cost, smart weapons developers have now begun to investigate more unconventional guided projectile concepts with passive roll control capability [17][13].

1.1.1 Control Surface Implementation

Control of flight vehicles, particularly projectiles, using lifting surfaces as control mechanisms is not a new idea and has been employed extensively in the missile community and, more recently, in the smart weapons community. A large collection of aerodynamic data for numerous canard-equipped missile configurations has been amassed by the U.S. Air Force [15] and used to develop aeroprediction semiempirical software, according to work by Moore [27]. Aeroprediction Inc.'s AP09 code [26] and Arrow Tech's PRODAS software [1] have emerged over the past decade as

industry standard projectile aerodynamic prediction tools. In the guided projectile community, several studies and development programs have considered use of canard mechanisms for flight control purposes onboard both fin- and spin-stabilized indirect fire munitions. Smith et al. [38] have explored the application of canard control to a spin-stabilized projectile for dispersion error reduction. Their design used a seeker-based guidance system and mounted canards on a rolling bearing spinning slower than the body in order to reduce canard actuator power and bandwidth. Later, Costello [8][9] investigated the use of canards onboard an artillery shell for the purpose of range extension. Example results and trade studies showed that dramatic range increases could be accomplished using reasonably sized canards.

Numerous guided artillery projectiles developed over the past three decades have employed canard control mechanisms. One of the first such development programs was Copperhead [29][30], a 155 mm artillery round that used four dithering rear tail fins for roll stabilization and maneuver control as well as four fixed canards placed forward on the body for maneuver augmentation. Another program, the Low Cost Competent Munition development effort conducted jointly by the U.S. Army and Navy [44], explored the use of extendable fixed canards for use as drag brakes as well as dithering canards for use in precise trajectory corrections. The U.S. Navy's Extended-Range Guided Munition [42][2] combined use of a rocket motor, tail fins, and forward-placed canards to significantly extend the range of a 5 in. projectile for naval guns. Most recently, the Army's Excalibur [19] and Precision Guidance Kit [28] development programs for 155 mm projectiles have demonstrated the feasibility of using canard mechanisms to successfully guide cannon-launched munitions.

Clearly, control surface implementation has proven to be a useful technology thus far; however, still more significant advancements are anticipated to be made. As control of projectiles with asymmetric control surface configurations are researched, a breakthrough in more accurate, yet cheaper, guided munitions might be achievable.

In an effort to reach this end, weapons developers are now requiring design tools, such as aero prediction methods and projectile linear theory, to be upgraded to account for these asymmetries.

1.1.2 Projectile Linear Theory

Projectile Linear Theory has long been an analytical work horse in the ballistics community [23] and is used to reduce the complexity of the flight dynamic equations of motion through application of a series of simplifications and assumptions. These *linearized* equations of motion allow the engineer to apply concepts from *Linear Systems Theory* [14][24][41], which is well understood and easily implemented. Over time, projectile linear theory has been used for stability analysis, aerodynamic coefficient estimation using range data, and fast trajectory prediction. Basic projectile linear theory has extended by various authors to handle more sophisticated aerodynamic models [32], asymmetric mass properties, [22], fluid payloads [43][34], moving internal parts [5][21][37], dual spin projectiles [39][11], extending flight [33], lateral force impulses [6][20][3], and model predictive control [35]. Recently, an extended linear theory for aerodynamically asymmetric lifting surfaces has been developed for a specific canard configuration to investigate the effects of canard dithereing [7] and canard stall on projectile roll and pitch damping [25].

1.2 Thesis Objectives

The work reported here aims to develop an extended linear theory for arbitrary asymmetric lifting surface configurations and to study flight dynamic stability by performing a series of parametric trade studies. The thesis objectives are formally stated below:

- Develop an extended projectile linear theory model for configurations with lifting surfaces that are arbitrarily located and oriented on the body. Validate the model with an industry standard code (BOOM) [10].

- Use the new projectile linear theory model to evaluate flight dynamic stability as a function of projectile parameters and lifting surface parameters. Investigate if a standard linear time-invariant (LTI) system approximation is sufficient or if a more involved linear time-periodic (LTP) stability analysis (*Floquet Theory*) is necessary.

- Use the projectile linear theory to perform a series of parametric trade studies on asymmetric projectile configurations to investigate airframe flight dynamic stability characteristics by constructing root-locus plots to track changing system poles.

1.3 Primary Thesis Contributions

This research is intended to aid in the design of smart weapons technoligies and contributes to the state-of-the-art in the following ways:

- Developed an extended projectile linear theory to account for aerodynamic effects of arbitrary lifting surface projectile configurations.

- Applied *Floquet Theory* to the extended projectile linear theory models to account for periodic effects due to aerodynamic asymmetries in the roll angle.

- Conducted a series of trade studies to investigate the effects of several common projectile lifting surface asymmetries on flight dynamic modes and mode shapes.

1.4 Projectile Testbed Description

Throughout this study, the Army-Navy basic finner will be used as the projectile testbed for all asymmetric lifting surface configurations. This projectile is commonly used in academic studies as its flight mechanics are well known and readily available [12]. The figure below shows a computer graphic of the basic finner projectile and Appendix A provides further discussion and summary.

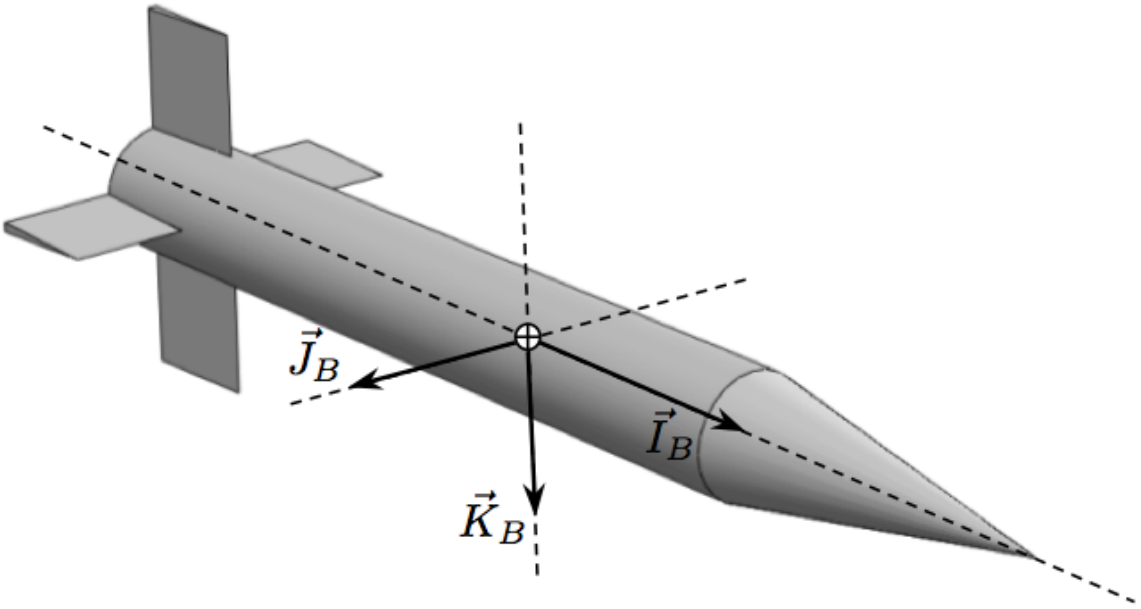

Figure 1: A 3-D renduring of the Army-Navy basic finner projectile airframe.

CHAPTER II

FLIGHT DYNAMIC THEORY

2.1 Vector Operators

To aid in the mathematical description of the flight dynamic model, two basic vector operators are first defined. Consider an arbitrary vector $\vec{A}$ with vector components (or measure numbers) expressed in some coordinate reference frame (N).

$$\vec{A} = a_x \vec{I}_N + a_y \vec{J}_N + a_z \vec{K}_N$$

The measure number operator, $\mathbb{C}_N(\cdot)$, and the vector cross-product operator, $\mathbb{S}_N(\cdot)$, are defined below in equations (1) and (2) with respect to a reference frame N.

$$\mathbb{C}_N\left(\vec{A}\right) = \left\{ \begin{array}{c} a_x \\ a_y \\ a_z \end{array} \right\} \tag{1}$$

$$\mathbb{S}_N\left(\vec{A}\right) = \left[\begin{array}{ccc} 0 & -a_z & a_y \\ a_z & 0 & -a_x \\ -a_y & a_x & 0 \end{array} \right] \tag{2}$$

These two operators provide for a very efficient mathematical description of the ensuing dynamic models. A typical example is the cross-product of two vectors, which is commonly found in velocity or acceleration expressions. The equation below illustrates an identity for the cross-product of two arbitrary vectors $\vec{B}$ and $\vec{C}$, using measure number and cross-product operators.

$$\vec{B} \times \vec{C} = \mathbb{S}_N\left(\vec{B}\right) \cdot \mathbb{C}_N\left(\vec{C}\right) \tag{3}$$

2.2 Reference Frames

Specification of references frames and rotation sequences between frames provides clarity and structure to the dynamic equations of motion and is therefore a logical starting point [18]. As is convention in the aerospace industry, the attitude (orientation) of a vehicle can be expressed by using a (3-2-1) single-axis, body-fixed composite rotation sequence. Figures 2 and 3 illustrate how this rotation sequence relates a body-fixed frame (B) to an inertial frame (I).

Rotation sequences can be thought of as representing the coordinate axes of one reference frame ($\vec{I}_{x1}$, $\vec{J}_{x1}$, $\vec{K}_{x1}$) in terms of another reference frame ($\vec{I}_{x2}$, $\vec{J}_{x2}$, $\vec{K}_{x2}$) and can be mathematically described by orthonormal matrices. Because these matrices are orthonormal, their matrix inverses are equal to the transpose - a fact that can greatly reduce computational effort. The following outline describes the (3-2-1) rotation sequence as a series of single-axis rotations, parameterized by the Euler angles: yaw - ψ, pitch - θ, roll - ϕ (see to Figure 3). *Note that single-axis transformation matrices about an axis x by angle y are notated as* $[\mathbf{T}_x(y)]$.

- Yaw - Rotate about $\vec{K}_I$ by the angle ψ. The resulting new axis is the Intermediate 1 Frame (1).

$$\begin{Bmatrix} \vec{I}_1 \\ \vec{J}_1 \\ \vec{K}_1 \end{Bmatrix} = [\mathbf{T}_K(\psi)] \cdot \begin{Bmatrix} \vec{I}_I \\ \vec{J}_I \\ \vec{K}_I \end{Bmatrix} \tag{4}$$

- Pitch - Rotate about $\vec{J}_1$ by the angle θ. The resulting new axis is the No-Roll Frame (NR).

$$\begin{Bmatrix} \vec{I}_{NR} \\ \vec{J}_{NR} \\ \vec{K}_{NR} \end{Bmatrix} = [\mathbf{T}_J(\theta)] \cdot \begin{Bmatrix} \vec{I}_1 \\ \vec{J}_1 \\ \vec{K}_1 \end{Bmatrix} \tag{5}$$

- Roll - Rotate about $\vec{I}_{NR}$ by the angle ϕ. The resulting new axis is the Body-Fixed Frame (B).

$$\left\{ \begin{array}{c} \vec{I}_B \\ \vec{J}_B \\ \vec{K}_B \end{array} \right\} = [\mathbf{T}_I(\phi)] \cdot \left\{ \begin{array}{c} \vec{I}_{NR} \\ \vec{J}_{NR} \\ \vec{K}_{NR} \end{array} \right\} \tag{6}$$

Equations (7)-(9) define the single-axis transformation matrices, where a standard shorthand for trigonometric functions is employed: $\sin(\alpha) \equiv s_\alpha$, $\cos(\alpha) \equiv c_\alpha$, and $\tan(\alpha) \equiv t_\alpha$.

$$[\mathbf{T}_K(\psi)] = \begin{bmatrix} c_\psi & s_\psi & 0 \\ -s_\psi & c_\psi & 0 \\ 0 & 0 & 1 \end{bmatrix} \tag{7}$$

$$[\mathbf{T}_J(\theta)] = \begin{bmatrix} c_\theta & 0 & -s_\theta \\ 0 & 1 & 0 \\ s_\theta & 0 & c_\theta \end{bmatrix} \tag{8}$$

$$[\mathbf{T}_I(\phi)] = \begin{bmatrix} 1 & 0 & 0 \\ 0 & c_\phi & s_\phi \\ 0 & -s_\phi & c_\phi \end{bmatrix} \tag{9}$$

Using substitution, the attitude of any reference frame can be represented with respect to another. The component equations below show the overall rotation transformation from inertial to body frame.

$$\left\{ \begin{array}{c} \vec{I}_B \\ \vec{J}_B \\ \vec{K}_B \end{array} \right\} = [\mathbf{T}_I(\phi)] \cdot [\mathbf{T}_J(\theta)] \cdot [\mathbf{T}_K(\psi)] \cdot \left\{ \begin{array}{c} \vec{I}_I \\ \vec{J}_I \\ \vec{K}_I \end{array} \right\} \tag{10}$$

Equation (10) states that the attitude of a body-fixed frame with respect to an inertial frame can be determined given knowledge of the Euler angles. For simplicity and understanding, a rotation transformation between any two arbitrary reference frames

(x1) and (x2) is now described by $[\mathbf{T}_{x2\leftarrow x1}]$, where the Euler angles relating the two frames are implicitly understood. Thus for a transformation between frame (B) and frame (I), the series of single-axis transformation matrices found in Equation (10) can be equivalently represented as follows:

$$[\mathbf{T}_{B\leftarrow I}] = [\mathbf{T}_I(\phi)] \cdot [\mathbf{T}_J(\theta)] \cdot [\mathbf{T}_K(\psi)]\,. \tag{11}$$

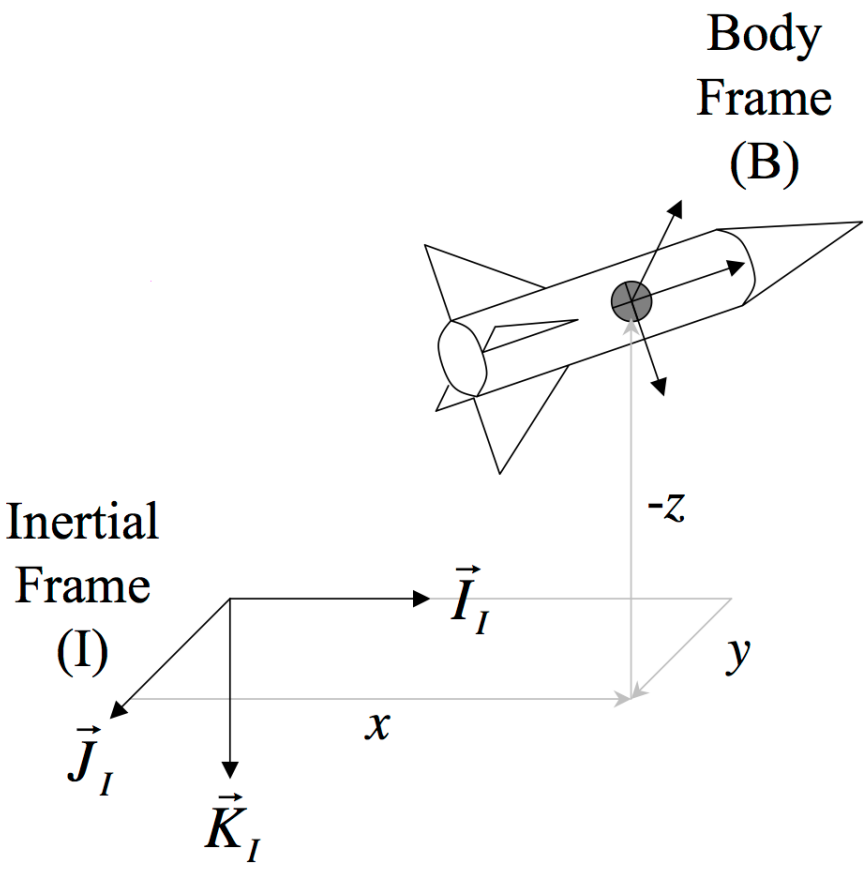

Figure 2: An illustration of an inertial reference frame to the body-fixed reference frame. The origin of frame (B) is located at the vehicle mass center and is free to rotate in space. The origin of frame (I) is arbitrarily located is space but the orientation and position of this frame is fixed in space.

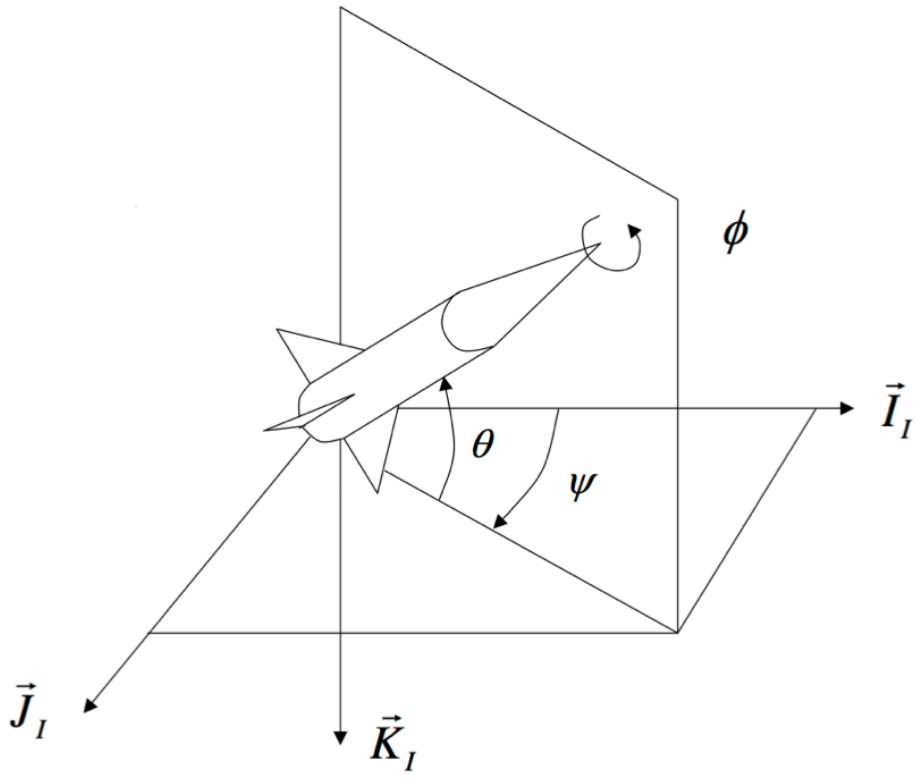

Figure 3: Illustration of Euler angle (aerospace convention) rotation sequence from inertial frame to body-fixed frame. Starting with the projectile aligned along $\vec{I}_I$, the projectile is first rotated by the angle ψ, then vertically by the angle θ, and finally rotated by the roll angle ϕ. These three angles completely describe the attitude of the projectile with respect to the inertial frame.

2.3 Important Vector Definitions

Along with the Euler angles, the dynamic behavior of a projectile in free flight will be quantified and evaluated using time history of position, velocity, and angular velocity vectors. The following vectors are defined and will be used in the construction of the dynamic equations of motion.

- $\vec{r}_{O\to\oplus}$ – position from the origin of the inertial frame O to the projectile mass center (the origin of the body frame). See Figure 2 for illustration of these vector components in regards to projectile position.

$$\vec{r}_{O\to\oplus} = x\vec{I}_I + y\vec{J}_I + z\vec{K}_I \tag{12}$$

- $\vec{V}_{\oplus/I}$ – velocity of the projectile mass center with respect to reference frame (I). Equation (13) defines the projectile velocity vector in terms of inertial frame measure numbers, while equation (14) is an equivalent expression in terms of body frame measure numbers.

$$\vec{V}_{\oplus/I} = \dot{x}\vec{I}_I + \dot{y}\vec{J}_I + \dot{z}\vec{K}_I \tag{13}$$

$$\vec{V}_{\oplus/I} = u\vec{I}_B + v\vec{J}_B + w\vec{K}_B \tag{14}$$

- $\vec{\omega}_{B/I}$ – angular velocity of the projectile body frame (B) with respect to reference frame (I). Equation (15) defines the projectile angular velocity vector in terms of Euler angle time derivatives, but note that each term is expressed with a difference reference frame vector than the other terms. Equation (16) is an equivalent expression in terms of body frame measure numbers.

$$\vec{\omega}_{B/I} = \dot{\psi}\vec{K}_I + \dot{\theta}\vec{J}_1 + \dot{\phi}\vec{I}_{NR} \tag{15}$$

$$\vec{\omega}_{B/I} = p\vec{I}_B + q\vec{J}_B + r\vec{K}_B \tag{16}$$

2.4 Nonlinear Flight Dynamic Model

2.4.1 Trajectory Equations of Motion

The nonlinear flight dynamic model used in this study is a standard six-degree-of-freedom (6DOF) model. These ordinary differential equations are widely used in computational simulation of free flight vehicles and are reported in many sources including: Carlucci [4], Etkin [14], McCoy [23], and Murphy [31]. Derived using the standard Newton-Euler approach, these 12 equations of motion are provided below.

$$\mathbb{C}_I\left(\dot{\vec{V}}_{\oplus/I}\right) = [\mathbf{T}_{B\leftarrow I}]^T \cdot \mathbb{C}_B\left(\dot{\vec{V}}_{\oplus/I}\right) \tag{17}$$

$$\left\{\begin{array}{c}\dot{\phi}\\ \dot{\theta}\\ \dot{\psi}\end{array}\right\} = \left[\begin{array}{ccc}1 & s_\phi t_\theta & c_\phi t_\theta\\ 0 & c_\phi & -s_\phi\\ 0 & s_\phi/c_\theta & c_\phi/c_\theta\end{array}\right] \cdot \mathbb{C}_B\left(\vec{\omega}_{B/I}\right) \tag{18}$$

$$\mathbb{C}_B\left(\dot{\vec{V}}_{\oplus/I}\right) = \frac{1}{m}\mathbb{C}_B\left(\vec{F}\right) - \mathbb{S}_B\left(\vec{\omega}_{B/I}\right) \cdot \mathbb{C}_B\left(\vec{V}_{\oplus/I}\right) \tag{19}$$

$$\mathbb{C}_B\left(\dot{\vec{\omega}}_{B/I}\right) = [\mathbf{I}]^{-1}\left(\mathbb{C}_B\left(\vec{M}\right) - \mathbb{S}_B\left(\vec{\omega}_{B/I}\right) \cdot [\mathbf{I}] \cdot \mathbb{C}_B\left(\vec{\omega}_{B/I}\right)\right) \tag{20}$$

Equations (17) and (18) are commonly referred to as the positional kinematic and attitude kinematic equations of motion, respectively. Equations (19) and (20) are direct applications of *Newton's* 2^{nd} *Law of Motion* in linear and angular forms. In the latter equations, the resultant externally applied force and moment vectors are represented by $\vec{F}$ and $\vec{M}$, respectively. The symbol m represents the projectile mass and $[\mathbf{I}]$ is the projectile inertia tensor matrix.

2.4.2 External Force and Moment Models

The externally applied force $\vec{F}$ in Equation (19) can be decomposed into contributions due to weight (W), body aerodynamics (B), and lifting surface aerodynamics (C). Assuming that a projectile body is axially symmetric, the body aerodynamic force

can be further split down into contributions from a steady aerodynamic (SA) force and a Magnus (M) aerodynamic force. Superposition of these forces results in Equation (21).

The externally applied moment $\vec{M}$ in Equation (20) acts about projectile the mass center and in similar fashion to Equation (21) can be broken down into contributions from steady aerodynamics, unsteady aerodynamics (UA), and moments generated by the Magnus force and the lifting surface forces. Equation (22) summarizes decomposition of the moment contributions.

$$\mathbb{C}_B\left(\vec{F}\right) = \mathbb{C}_B\left(\vec{F}_W\right) + \mathbb{C}_B\left(\vec{F}_{SA}\right) + \mathbb{C}_B\left(\vec{F}_M\right) + \mathbb{C}_B\left(\vec{F}_C\right) \tag{21}$$

$$\mathbb{C}_B\left(\vec{M}\right) = \mathbb{C}_B\left(\vec{M}_{SA}\right) + \mathbb{C}_B\left(\vec{M}_{UA}\right) + \mathbb{C}_B\left(\vec{M}_M\right) + \mathbb{C}_B\left(\vec{M}_C\right) \tag{22}$$

2.4.3 Projectile Body Force and Moment Models

Equation (23) gives the weight force in the body coordinate system.

$$\mathbb{C}_B\left(\vec{F}_W\right) = mg \begin{Bmatrix} -s_\theta \\ s_\phi c_\theta \\ c_\phi c_\theta \end{Bmatrix} \tag{23}$$

Equation (24) provides the expression for the steady aerodynamic force, which acts at the projectile aerodynamic center of pressure (COP).

$$\mathbb{C}_B\left(\vec{F}_{SA}\right) = -\frac{\pi}{8}\rho V^2 D^2 \begin{Bmatrix} C_{X_o} + C_{X_2}\left(v^2 + w^2\right)/V^2 \\ C_{\mathrm{NA}} v/V \\ C_{\mathrm{NA}} w/V \end{Bmatrix} \tag{24}$$

Equation (25) expresses the Magnus aerodynamic force acting on the projectile at the Magnus aerodynamic center (MAC).

$$\mathbb{C}_B\left(\vec{F}_M\right) = \frac{\pi}{8}\rho V^2 D^2 \begin{Bmatrix} 0 \\ pDC_{\mathrm{YPA}} w/\left(2V^2\right) \\ -pDC_{\mathrm{YPA}} v/\left(2V^2\right) \end{Bmatrix} \tag{25}$$

Given the previous definitions of the projectile velocity vector (Equations (13) and (14)), the projectile total velocity V can be computed from the following expression.

$$V = \|\vec{V}_{\oplus/I}\| \tag{26}$$

The moment due to the steady aerodynamic and Magnus forces are expressed in Equations (27) and (28).

$$\mathbb{C}_B\left(\vec{M}_{SA}\right) = \mathbb{S}_B\left(\vec{r}_{\oplus\to C_p}\right) \cdot \mathbb{C}_B\left(\vec{F}_{SA}\right) \tag{27}$$

$$\mathbb{C}_B\left(\vec{M}_{M}\right) = \mathbb{S}_B\left(\vec{r}_{\oplus\to C_p}\right) \cdot \mathbb{C}_B\left(\vec{F}_{M}\right) \tag{28}$$

The moment due to the unsteady aerodynamic force acting on the projectile is expressed in Equation (29).

$$\mathbb{C}_B\left(\vec{M}_{UA}\right) = \frac{\pi}{8}\rho V^2 D^3 \left\{ \begin{array}{c} C_{\mathrm{LDD}} + pDC_{\mathrm{LP}}/\left(2V\right) \\ qDC_{\mathrm{MQ}}/\left(2V\right) \\ rDC_{\mathrm{MQ}}/\left(2V\right) \end{array} \right\} \tag{29}$$

Note, for finned projectiles that the Magnus force and moment expressions can be small, since its effect is small for slowly rolling projectiles. It is included here for model completeness and generality.

The coefficients used in this aerodynamic model are specific functions of the projectile Mach number. All aerodynamic coefficients are estimated using standard aero-prediction techniques within the PRODAS Software Package [1].

2.4.4 Lifting Surface Aerodynamic Model

The lifting surface aerodynamic model implemented here was taken from the *BOOM* canard model [10], which treats the canard aerodynamic effects as a point force acting at the lifting surface aerodynamic center. The moment generated by this point force can then be computed via cross product between the distance vector from the projectile mass center to the canard forces application point and the canard force.

By superposition, this model can account for an arbitrary number of lifting surfaces n, positioned and oriented anywhere on a given parent projectile body.

$$\mathbb{C}_B\left(\vec{F}_C\right) = \sum_{i=1}^{n} \mathbb{C}_B\left(\vec{F}_{C_i}\right) \tag{30}$$

$$\mathbb{C}_B\left(\vec{M}_C\right) = \sum_{i=1}^{n} \mathbb{S}_B\left(\vec{r}_{\oplus\to C_i}\right) \cdot \mathbb{C}_B\left(\vec{F}_{C_i}\right) \tag{31}$$

For the i^{th} lifting surface, the point of action is defined by a position vector $\vec{r}_{\oplus\to C_i}$.

$$\mathbb{C}_B\left(\vec{r}_{\oplus\to C_i}\right) = \left\{ \begin{array}{c} \Delta SL_{C_i} \\ \Delta BL_{C_i} \\ \Delta WL_{C_i} \end{array} \right\} \tag{32}$$

Equation (32) describes the position of the i^{th} lifting surface as stationline (SL), buttline (BL), and waterline (WL) components. The orientation of this i^{th} lifting surface is defined by its own lifting surface reference frame (C_i), which is obtained by one body-fixed rotation about an axis of the parent projectile body frame. Starting with the canard axis aligned with the projectile body frame B, a lifting surface is rotated about the $\vec{I}_B$ axis by the azimuthal angle (ϕ_{C_i}). The single-axis transformation matrix used to move from the frame C_i back to frame B is shown below in Equation (33).

$$[\mathbf{T}_{B\leftarrow C_i}] = \left[\begin{array}{ccc} 1 & 0 & 0 \\ 0 & c_{\phi_{C_i}} & -s_{\phi_{C_i}} \\ 0 & s_{\phi_{C_i}} & c_{\phi_{C_i}} \end{array} \right] \tag{33}$$

Strip theory is used to compute the lift and drag aerodynamic loads [14]. Equations (34) and (35) summarize the general models, where aerodynamic prediction software is again used to estimate all coefficients as a function of Mach number only. Note that the local aerodynamic lifting surface coefficient of equation (34) is modeled as a linear function of α_{C_i} – the local aerodynamic angle of attack.

$$C_{L_{C_i}} = C_{L_\alpha}\alpha_{C_i} \tag{34}$$

$$C_{D_{C_i}} = C_{D_o} \tag{35}$$

Figure 4 illustrates how the aerodynamic angle of attack of the i^{th} lifting surface is calculated using only u_{C_i} and w_{C_i} components of the air velocity vector at the point force application point.

$$\alpha_{C_i} = \tan^{-1}\left(\frac{w_{C_i}}{u_{C_i}}\right) + \delta_{C_i} \tag{36}$$

The local air velocity vector expressed in the i^{th} lifting surface reference frame.

$$\mathbb{C}_{C_i}\left(\vec{V}_{C_i/I}\right) = \left\{ \begin{array}{c} u_{C_i} \\ v_{C_i} \\ w_{C_i} \end{array} \right\} \tag{37}$$

Given knowledge of $\vec{V}_{\oplus/I}$ and $\vec{\omega}_{B/I}$, the i^{th} lifting surface air velocity vector is computed from the following expression.

$$\mathbb{C}_{C_i}\left(\vec{V}_{C_i/I}\right) = [T_{B\leftarrow C_i}]^T \cdot \left(\mathbb{C}_B\left(\vec{V}_{\oplus/I}\right) + \mathbb{S}_B\left(\vec{\omega}_{B/I}\right) \cdot \mathbb{C}_B\left(\vec{r}_{\oplus\rightarrow C_i}\right)\right) \tag{38}$$

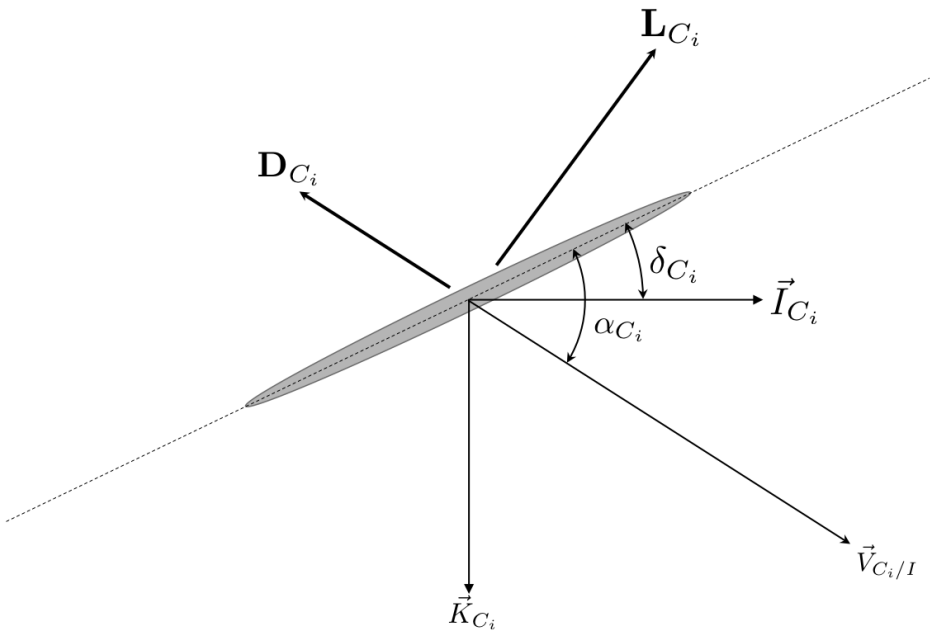

Figure 4: Lifting Surface Aerodynamic Model Force Diagram

From Figure 4, the aerodynamic force components generated by the i^{th} lifting surface can be calculated in the projectile body reference frame by Equation (39).

$$\mathbb{C}_B\left(\vec{F}_{C_i}\right) = \frac{1}{2}\rho V^2 S_{C_i}\left[\mathbf{T}_{B\leftarrow C_i}\right]\left\{\begin{array}{c} C_{L_{C_i}}\sin\left(\alpha_{C_i}-\delta_{C_i}\right) - C_{D_{C_i}}\cos\left(\alpha_{C_i}-\delta_{C_i}\right) \\ 0 \\ -C_{L_{C_i}}\cos\left(\alpha_{C_i}-\delta_{C_i}\right) - C_{D_{C_i}}\sin\left(\alpha_{C_i}-\delta_{C_i}\right) \end{array}\right\} \tag{39}$$

2.5 Linear Flight Dynamic Model

The 6DOF rigid body projectile model discussed above consists of 12 highly nonlinear differential equations for which a closed form solution has not been directly found. Significant work has been performed to simplify the equations of motion such that an accurate analytical solution can be determined.

2.5.1 Classical Projectile Linear Theory Assumptions

In order to arrive at a set of analytically solvable ordinary linear differential equations, the following assumptions and simplifications are made:

(1) Rather than employing a reference frame fixed to the projectile body, projectile linear theory uses an intermediate reference frame, which is aligned with the projectile axis of symmetry but does not roll. Lateral translational and rotational velocity components described in this frame, known as the no-roll (NR) frame or the fixed plane frame, are denoted with a ‘ ˜ ’ overscore.

$$\mathbb{C}_{NR}\left(\vec{V}_{B/I}\right) = \left\{\begin{array}{c} \tilde{u} \\ \tilde{v} \\ \tilde{w} \end{array}\right\} \tag{40}$$

Components of the linear and angular velocity in the body-fixed frame are computed from body frame components of the same vector through a single-axis rotation transformation. For example, the body frame components of the

projectile mass center velocity are transformed to the NR frame by:

$$\mathbb{C}_{NR}\left(\vec{V}_{B/I}\right) = [\mathbf{T}_{B\leftarrow NR}] \cdot \mathbb{C}_B\left(\vec{V}_{B/I}\right) \tag{41}$$

(2) A change of variables is made from the velocity along the projectile axis of symmetric, u, to the total velocity, V. Equations (42) and (43) relate V to u and their derivatives.

$$V = \sqrt{u^2 + v^2 + w^2} = \sqrt{\tilde{u}^2 + \tilde{v}^2 + \tilde{w}^2} \tag{42}$$

$$\dot{V} = \frac{u\dot{u} + v\dot{v} + w\dot{w}}{V} = \frac{u\dot{u} + \tilde{v}\dot{\tilde{v}} + \tilde{w}\dot{\tilde{w}}}{V} \tag{43}$$

(3) Dimensionless arc length, s, is used as the independent variable instead of time, t. Equation (44) defines dimensionless arc length.

$$s = \frac{1}{D}\int_0^t V dt \tag{44}$$

Equations (46) and (47) relate time and arc length derivatives of a dummy variable ζ. Dotted terms refer to time derivatives and primed terms denote arc length derivatives:

$$\dot{\zeta} = \left(\frac{V}{D}\right)\zeta' \tag{45}$$

$$\ddot{\zeta} = \left(\frac{V}{D}\right)^2\left(\zeta'' + \frac{\zeta' V'}{V}\right) \tag{46}$$

(4) The Euler yaw angle is assumed to be small so that

$$\sin(\psi) \approx \psi, \qquad \cos(\psi) \approx 1 \tag{47}$$

(5) The projectile is mass balanced such that the center of gravity lies in the rotational axis of symmetry:

$$\begin{aligned} I_{xy} &= I_{xz} = I_{yz} = 0 \\ I_R &= I_{xx} \\ I_P &= I_{yy} = I_{zz} \end{aligned} \tag{48}$$

(6) Aerodynamic angles of attack are small so that

$$\alpha \approx \frac{w}{V}, \quad \beta \approx \frac{v}{V} \tag{49}$$

(7) Quantities V and ϕ are large compared to θ, ψ, $\tilde{v}$, $\tilde{w}$, $\tilde{q}$ and $\tilde{r}$ such that products of small quantities and theory derivatives are negligible.

$$\begin{aligned} &\phi \gg \psi, \theta \\ &\tilde{u} \approx V \\ &V \gg \tilde{v}, \tilde{w} \\ &p \gg \tilde{q}, \tilde{r} \end{aligned} \tag{50}$$

A more detailed discussion of the development of classical projectile linear theory is provided by McCoy [23] and Ollerenshaw [35].

2.5.2 Extended Projectile Linear Theory Assumptions

The previous discussion is limited to projectiles that are symmetric with respect to aerodynamics and mass/inertia properties. An extension of the classical PLT assumptions applies to an arbitrary set of lifting surfaces, as proposed by Montalvo [25], which causes aerodynamic asymmetries on a projectile.

(8) The total velocities experienced by lifting surfaces are approximately equal to the projectile mass center velocity.

$$V \approx V_{C_1} \approx V_{C_2} \approx ... \approx V_{C_n} \tag{51}$$

(9) Lifting surface angles of attack are assumed small such that Equation (36) can be reduced to the following:

$$\alpha_{C_i} \approx \frac{w_{C_i}}{V} + \delta_{C_i} \tag{52}$$

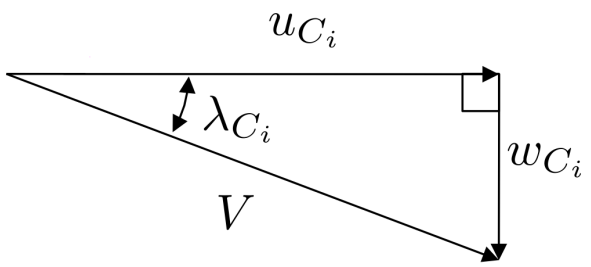

Figure 5: Lifting Surface Velocity Triangle Diagram

(10) The trigonometric functions $\sin(\alpha_{C_i} - \delta_{C_i})$ and $\cos(\alpha_{C_i} - \delta_{C_i})$ in Equation (39) can be linearized by utilizing a velocity diagram and defining an angle λ_{C_i}.

$$\lambda_{C_i} = \alpha_{C_i} - \delta_{C_i} = \tan\left(\frac{w_{C_i}}{u_{C_i}}\right) \approx \frac{w_{C_i}}{u_{C_i}} \tag{53}$$

$$\sin(\alpha_{C_i} - \delta_{C_i}) \approx \sin(\lambda_{C_i}) = \frac{w_{C_i}}{V} \tag{54}$$

$$\cos(\alpha_{C_i} - \delta_{C_i}) \approx \cos(\lambda_{C_i}) = \frac{u_{C_i}}{V} \tag{55}$$

2.5.3 Classical Linear Theory Equations of Motion

Application of assumptions (1)-(7) leads to a set of coupled linear differential equations, with the exception that the total velocity, V, the roll rate p, and the pitch angle, θ, appear in nonlinear fashion in many of the equations. To remedy this, first the assumption is made that V changes slowly with respect to the other variables and is thus considered to be constant, $V = V_o$, when it appears as a coefficient in all dynamic equations except its own. The translational and rotational kinematic equations reduce to the following expressions.

$$x' = D\cos[\theta] \tag{56}$$

$$y' = \frac{D}{V_o}\tilde{v} + D\psi\cos[\theta] \tag{57}$$

$$z' = \frac{D}{V_o}\cos[\theta]\tilde{w} - D\sin[\theta] \tag{58}$$

$$\phi' = \frac{D}{V_o}p + \frac{D}{V_o}\tilde{r}\tan[\theta] \tag{59}$$

$$\theta' = \frac{D}{V_o}\tilde{q} \tag{60}$$

$$\psi' = \frac{D}{V_o}\frac{1}{\cos[\theta]}\tilde{r} \tag{61}$$

The dynamic equations are expressed below in the quasi-linear form $x' = \mathbf{A}x + B$, where the roll rate is also held constant, $p = p_o$, in several entries of the linearized coefficients C_{**}. *(See Appendix B for a complete summary of all classical PLT coefficients.)*

$$\begin{Bmatrix} V' \\ p' \\ \tilde{v}' \\ \tilde{w}' \\ \tilde{q}' \\ \tilde{r}' \end{Bmatrix} = \begin{bmatrix} C_{VV} & 0 & 0 & 0 & 0 & 0 \\ C_{pV} & C_{pp} & 0 & 0 & 0 & 0 \\ 0 & 0 & C_{\tilde{v}\tilde{v}} & 0 & 0 & C_{\tilde{v}\tilde{r}} \\ 0 & 0 & 0 & C_{\tilde{w}\tilde{w}} & C_{\tilde{w}\tilde{q}} & 0 \\ 0 & 0 & C_{\tilde{q}\tilde{v}} & C_{\tilde{q}\tilde{w}} & C_{\tilde{q}\tilde{q}} & C_{\tilde{q}\tilde{r}} \\ 0 & 0 & C_{\tilde{q}\tilde{v}} & C_{\tilde{r}\tilde{w}} & C_{\tilde{r}\tilde{q}} & C_{\tilde{r}\tilde{r}} \end{bmatrix} \cdot \begin{Bmatrix} V \\ p \\ \tilde{v} \\ \tilde{w} \\ \tilde{q} \\ \tilde{r} \end{Bmatrix} + \begin{Bmatrix} G_V \\ 0 \\ 0 \\ G_{\tilde{w}} \\ 0 \\ 0 \end{Bmatrix} \tag{62}$$

Observe in Equation (62) the the forcing vector B is populated in the 1st and 4th entries by the coefficients, G_V and $G_{\tilde{w}}$. These coefficients account for the contributions of gravity and are not linearly dependent on any dynamic states. Here V_o and θ_o are assumed to be approximately constant through flight.

$$G_V = -\frac{Dg\sin\theta_o}{V_o} \tag{63}$$

$$G_{\tilde{w}} = \frac{Dg\cos\theta_o}{V_o} \tag{64}$$

2.5.4 Extended Projectile Linear Theory Equations of Motion

Applying the extended PLT assumptions to the lifting surface model, all six of the total lifting surface force/moment components ($\tilde{X}'_C$, $\tilde{Y}'_C$,$\tilde{Z}'_C$, $\tilde{L}'_C$,$\tilde{M}'_C$, $\tilde{N}'_C$) take a quasi-linear form. Equation (65) shows a general form for this reduction for an example force component $\tilde{F}'_C$.

$$\begin{aligned}\tilde{F}'_C = m[&F'_V V + \left(F'_p + F'_{\text{pp}} p_o\right) p + \left(F'_{\tilde{v}} + F'_{\tilde{v}p} p_o\right) \tilde{v} \\ &+ \left(F'_{\tilde{w}} + F'_{\tilde{w}p} p_o\right) \tilde{w} + \left(F'_{\tilde{q}} + F'_{\tilde{q}p} p_o\right) \tilde{q} + \left(F'_{\tilde{r}} + F'_{\tilde{r}p} p_o\right) \tilde{r}]\end{aligned} \tag{65}$$

For the above general form for a lifting surface force component expression, the coefficients F'_* are constants with respect to state variables with the exception of the projectile roll angle ϕ. These coefficients can also be functions of lifting surface parameters, such as: position components – $\mathbb{C}_B\left(\vec{r}_{\oplus \to C_i}\right)$; orientation – ϕ_{C_i} and δ_{C_i}; planform area – S_{C_i}; and aerodynamic data – $C_{L_{C_i}}$ and $C_{D_{C_i}}$. *(See Appendix C for a complete summary of all extended projectile linear theory coefficients.)*

$$F'_* = func\left(\phi, \text{lifting surface parameters}\right) \tag{66}$$

Incorporating the lifting surface force/moment components into the classical PLT model greatly increases the coupling of the dynamic equations of motion; however, the kinematic equations remain unchanged. Again, the extended linear dynamic equations are expressed in the quasi-linear form $x' = \mathbf{A}x + B$, where the coefficient matrix $\mathbf{A}$ takes the following form shown below in Equation (67).

$$\mathbf{A} = \left[\begin{array}{c|c|c|c|c|c} \tilde{X}'_V + C'_{VV} & \tilde{X}'_p + \tilde{X}'_{pp}p_o & \tilde{X}'_{\tilde{v}} + \tilde{X}'_{\tilde{v}p}p_o & \tilde{X}'_{\tilde{w}} + \tilde{X}'_{\tilde{w}p}p_o & \tilde{X}'_{\tilde{q}} + \tilde{X}'_{\tilde{q}p}p_o & \tilde{X}'_{\tilde{r}} + \tilde{X}'_{\tilde{r}p}p_o \\ \hline \tilde{L}'_V + C'_{pV} & \tilde{L}'_p + \tilde{L}'_{pp}p_o + C'_{pp} & \tilde{L}'_{\tilde{v}} + \tilde{L}'_{\tilde{v}p}p_o & \tilde{L}'_{\tilde{w}} + \tilde{L}'_{\tilde{w}p}p_o & \tilde{L}'_{\tilde{q}} + \tilde{L}'_{\tilde{q}p}p_o & \tilde{L}'_{\tilde{r}} + \tilde{L}'_{\tilde{r}p}p_o \\ \hline \tilde{Y}'_V & \tilde{Y}'_p + \tilde{Y}'_{pp}p_o & \tilde{Y}'_{\tilde{v}} + \tilde{Y}'_{\tilde{v}p}p_o + C'_{\tilde{v}\tilde{v}} & \tilde{Y}'_{\tilde{w}} + \tilde{Y}'_{\tilde{w}p}p_o & \tilde{Y}'_{\tilde{q}} + \tilde{Y}'_{\tilde{q}p}p_o & \tilde{Y}'_{\tilde{r}} + \tilde{Y}'_{\tilde{r}p}p_o + C'_{\tilde{v}\tilde{r}} \\ \hline \tilde{Z}'_V & \tilde{Z}'_p + \tilde{Z}'_{pp}p_o & \tilde{Z}'_{\tilde{v}} + \tilde{Z}'_{\tilde{v}p}p_o & \tilde{Z}'_{\tilde{w}} + \tilde{Z}'_{\tilde{w}p}p_o + C'_{\tilde{w}\tilde{w}} & \tilde{Z}'_{\tilde{q}} + \tilde{Z}'_{\tilde{q}p}p_o + C'_{\tilde{w}\tilde{q}} & \tilde{Z}'_{\tilde{r}} + \tilde{Z}'_{\tilde{r}p}p_o \\ \hline \tilde{M}'_V & \tilde{M}'_p + \tilde{M}'_{pp}p_o & \tilde{M}'_{\tilde{v}} + \tilde{M}'_{\tilde{v}p}p_o + C'_{\tilde{q}\tilde{v}} & \tilde{M}'_{\tilde{w}} + \tilde{M}'_{\tilde{w}p} + C'_{\tilde{q}\tilde{w}} & \tilde{M}'_{\tilde{q}} + \tilde{M}'_{\tilde{q}p}p_o + C'_{\tilde{q}\tilde{q}} & \tilde{M}'_{\tilde{r}} + \tilde{M}'_{\tilde{r}p}p_o + C'_{\tilde{q}\tilde{r}} \\ \hline \tilde{N}'_V & \tilde{N}'_p + \tilde{N}'_{pp}p_o & \tilde{N}'_{\tilde{v}} + \tilde{N}'_{\tilde{v}p}p_o + C'_{\tilde{q}\tilde{v}} & \tilde{N}'_{\tilde{w}} + \tilde{N}'_{\tilde{w}p} + C'_{\tilde{r}\tilde{w}} & \tilde{N}'_{\tilde{q}} + \tilde{N}'_{\tilde{q}p}p_o + C'_{\tilde{r}\tilde{q}} & \tilde{N}'_{\tilde{r}} + \tilde{N}'_{\tilde{r}p}p_o + C'_{\tilde{r}\tilde{r}} \end{array}\right] \tag{67}$$

The extended PLT coefficient matrix of Equation (67) is a significant result and offers much insight into the aerodynamic contributions of lifting surfaces during flight. The additional physics due to arbitrary lifting surface configurations fully couples all the dynamic states together; however, for simple symmetric fin configurations many of the fin coefficients shown in *Appendix C* cancel out, thus reducing the complexity of the coefficient matrix substantially. Further, if the lifting surface aerodynamic effects are converted to the symmetric projectile body force and moment models of section (2.4.3) (see example in *Appendix D*), then the classical linear theory equations of motion shown in Equation (62) can be fully recovered.

A closer look at the lifting surface coefficients of *Appendix C* reveals that the extended linear theory model is periodic with ϕ and ϕ_{C_i}. This is encouraging that the extended linear theory model accounts for this effect, since a known shortcoming of the classical linear theory model is that it fails to account for periodic effects. To illustrate this point, consider on of the coefficient expressions from *Appendix C* – the

pitching moment dimensional derivative expression with respect to total velocity M'_V.

$$M'_V = -\frac{\pi\rho D^3}{8I_P}\sum_{i=1}^{n}(-\cos[\phi+\phi_{C_i}]C_{L_\alpha}\delta_{C_i}\Delta\mathrm{SL}_{C_i} + C_{D_o}(\sin[\phi]\Delta\mathrm{BL}_{C_i} + \cos[\phi]\Delta\mathrm{WL}_{C_i})) \tag{68}$$

Notice from the equation above that $\cos[\phi+\phi_{C_i}]$, $\sin[\phi]$, and $\cos[\phi]$ are all periodic functions in ϕ, and therefore M'_V must be a periodic function as well. In the next chapter further assumptions will be stated that can allow for ϕ to be approximated as a linear function of time. These important assumptions will allow for the extend linear system of Equation (67) to be approximated as either a linear time-invariant (LTI) or a linear time-periodic (LTP) system. Once these approximations are shown to be valid, then stability analysis techniques can be used to evaluate different projectile airframe configurations.

CHAPTER III

STABILITY THEORY

Given the quasi-linear model previously described, the projectile flight dynamics can be considered from the viewpoint of *Linear Systems Theory* [14][24][41], which offers many analysis techniques for 1st-order linear ordinary differential equations, including: stability theories, analytical solutions, and control systems design.

Stability for linear ordinary differential equations is evaluated by determining the system poles for the homogeneous dynamic system below.

$$x' = \mathbf{A}x \tag{69}$$

Here, x is the PLT dynamic state vector and matrix $\mathbf{A}$ is defined by Equation (67), where the non-homogeneous gravity vector $\vec{B}$ does not contribute to system stability. The general projectile matrix is a 12x12 matrix; however, considering only the dynamic equations of motion $\mathbf{A}$ is a 6th-order system ($n = 6$). A criterion for classifying system stability is defined as follows:

- A system is **stable** and $x(t) \to \{0\}$ if:

$$Re\,(\lambda_j) < 0, \text{ for all } (1 < j < n). \tag{70}$$

- A system is **neutrally stable** if:

$$Re\,(\lambda_j) \leq 0 \text{ and } Re\,(\lambda_1) = 0. \tag{71}$$

- A system is **unstable** and $x(t)$ is unbounded if:

$$Re\,(\lambda_j) > 0, \text{ for any } (1 < j < n). \tag{72}$$

Given the stability criteria defined above, stability analysis can be used to study the changes of system poles as system parameters are varied. Plots of these studies are called the *root locus* and will be used to perform parametric trade studies in *Chapter 5*.

3.1 Stability of Linear Time-Invariant (LTI) Systems

Recall in the description of the PLT model that the dynamic states V, p, and ϕ do not appear linearly in the equations of motion. These states were assumed to change slowly over time and formatted into the coefficient matrix $\mathbf{A}$, making the dynamic system quasi-linear. To approximate a LTI system, these states will be held to constant values, thus making $\mathbf{A}$ constant. *Chapter 4* section will address further the validity of this assumption.

A standard method for determining the system poles of an LTI system is by solving the eigenvalue/eigenvector problem [16] and [40] of Equation (73).

$$AX = \lambda X \tag{73}$$

Here the vector X is an eigenvector of matrix $\mathbf{A}$ with eigenvalue (system poles) λ. In Equation (74) the eigenvalues can be calculated by solving the *characteristic equation*.

$$\det\left(\mathbf{A} - \lambda_j \mathbf{I}\right) = 0, \quad \forall \quad (1 < j < n) \tag{74}$$

Upon solving Equation (74) for λ_j, Equation (73) can then be used to find the equivalent eigenvector X_j. Calculation of X_j can be helpful in determining the influence of λ_j on system state behavior, due to the orthogonality properties of eigenvectors.

Whenever an LTI approximation is sufficient for describing a dynamic system, the above equations can be easily implemented to evaluate stability and create root locus plots.

3.2 Stability of Linear Time-Periodic (LTP) Systems

For projectiles, the roll angle ϕ is often observed to be periodic by nature and can be closely approximated as a linear function of time t.

$$\phi(t) = p_o t + \phi(0) \tag{75}$$

Assuming V and p are constant, the dynamic equations of motion can be represented by Equation (76), where $\phi(t)$ is allowed to vary within $\mathbf{A}$ from the previous equation.

$$x' = \mathbf{A}(t)x \tag{76}$$

Further investigation into the extended linear theory lifting surface coefficients in *Appendix C* reveals that $\phi(t)$ always appears inside the trigonometric periodic functions, sine and cosine. Therefore the dynamic coefficient matrix $\mathbf{A}(t)$ is also periodic by nature by the period, $T = (2\pi/p_o)$.

$$\mathbf{A}(t) = \mathbf{A}(t + NT), \quad \text{for} \quad N = 0 \pm 1, \pm 2, ..., \pm\infty \tag{77}$$

Equation (77) implies that if the independent variable t is replaced by $t+T$, the system in Equation (76) remains invariant. To evaluate the stability of this type of linear system *Floquet Theory* is employed. As with any linear system, the superposition principle can be evoked to express $x(t)$ as a linear combination of the initial state vector $x(0)$.

$$x(t) = \mathbf{\Phi}\,(t)\, x(0) \tag{78}$$

The matrix $\mathbf{\Phi}\,(t, t_o)$ is commonly referred to as the *fundamental matrix* in linear systems theory. Calculation of the fundamental matrix for any linear system can be found by solving the following initial value problem:

$$\frac{d}{dt}\mathbf{\Phi}\,(t) = \mathbf{A}(t)\mathbf{\Phi}\,(t)\,, \qquad \mathbf{\Phi}\,(0) = \mathbf{I} \tag{79}$$

were the matrix $\mathbf{I}$ is the identity matrix and is the same size as $\mathbf{A}(t)$.

Because the matrix $\mathbf{A}(t)$ is periodic, the fundamental matrix can also be expressed in a special form known as the *Floquet decomposition* [41].

$$\mathbf{\Phi}\left(t\right) = \mathbf{P}(t) \cdot e^{\mathbf{R}t} \cdot \mathbf{P}^{-1}(0) \tag{80}$$

Here the matrix $\mathbf{R}$, referred to as the *characteristic exponent matrix*, is a constant (possibly complex) matrix having the same size as $\mathbf{A}(t)$, and $\mathbf{P}(t)$ is a continuously differentiable matrix function that also has the same size and period as $\mathbf{A}(t)$ and is invertible for all t.

A principle results of Floquet theory is that the stability of Equation (76) can be ascertained from the characteristic exponent matrix R [36]. Evaluating Equation (80) at $t = T$, yields the following expression.

$$\mathbf{\Phi}\left(T\right) = \mathbf{P}(0) \cdot e^{\mathbf{R}T} \cdot \mathbf{P}^{-1}(0) \tag{81}$$

The matrix $e^{\mathbf{R}T}$ is called the *characteristic multiplier matrix*. Equation (81) is a similarity transformation and hence, the eigenvalues between $\mathbf{\Phi}\left(T\right)$ and $e^{\mathbf{R}T}$ are preserved.

$$\text{eig}\left(\mathbf{\Phi}\left(T\right)\right) = \text{eig}\left(e^{\mathbf{R}T}\right) = \mu_j, \text{ for all } (1 < j < n) \tag{82}$$

The eigenvalues of $e^{\mathbf{R}T}$ are μ_j and can be related to η_j, the eigenvalues of $\mathbf{R}$, by the relation below.

$$\mu_j = e^{\eta_j T}, \text{ for all } (1 < j < n) \tag{83}$$

Thus, the j^{th} eigenvalue of the characteristic exponent matrix $\mathbf{R}$ can be found by algebraic manipulation of Equation (83).

$$\begin{gathered} \eta_j = \frac{1}{T} ln(\mu_j) = \frac{1}{T} log|\mu_j| + \frac{1}{T}\left(arg(\mu_j) + 2\pi k\right) i \\ \text{where } k = 0, \pm 1, ..., \pm\infty \end{gathered} \tag{84}$$

According to the stability criterion previously discussed, stability of the LTP system can be determined by considering the real part of η_j. Note that imaginary part of η_j is non-unique and other consideration is need to determine the integer value k. A more detailed discussion of the development of Floquet theory is proved by [24].

CHAPTER IV

MODEL VALIDATIONS

Before using the developed linear theory codes for trade studies of projectile configurations, the different analysis methods are compared to validate the modeling approach. The following list of validation cases was designed to (1) systematically eliminate errors, (2) form a strong argument for the validity of simulation results, and (3) provide insights into results generated by LTI and LTP model approximations.

- Case 1 – Validate the in-house 6DOF and PLT codes with an industry standard flight simulation software called BOOM [10] using a projectile with an asymmetric lifting surface configuration.
- Case 2 – Compare the traditional body aerodynamic and canard aerodynamic models using a symmetric projectile.
- Case 3 – Compare both classical and extended LTI models to a 6DOF trajectory simulation for a symmetric projectile.
- Case 4 – Compare LTI and LTP models to a 6DOF trajectory simulation for an asymmetric projectile.
- Case 5 – Generate LTI and LTP stability analysis results for a symmetric projectile flying at different roll rates.
- Case 6 – Generate LTI and LTP stability analysis results for a asymmetric projectile flying at different roll rates.

4.1 Case 1 – Validation of In-House Codes

Trajectory results were generated using the standard Army-Navy finned projectile testbed, described previously in Section (1.3), with two arbitrarily placed lifting surfaces in an asymmetric configuration. Figure 6 shows the lifting surface positions and orientations along the projectile, and Table 1 summarizes the physical lifting surface parameters. The trajectory simulations for both the derived 6DOF and PLT models used the initial conditions in Table 3. Results from these simulations were then compared to an equivalent simulation generated using an industry standard flight simulation software called BOOM [10]. Figures 7–19 show the results for this directly-fired asymmetric projectile, where excellent agreement between the codes is observed.

The trajectory results of Figures 7, 8, and 9 show that the projectile follows a near parabolic path in altitude, but that the aerodynamic asymmetries cause lateral deflection in the cross range shortly after launch. The asymmetries also cause the projectile roll angle to periodically increase after a transient time as seen in Figure 10. This transient period of approximately 0.5 (sec) can be clearly seen in the no-roll fixed transverse velocity and angular velocity plots of Figures 15, 16, 17, and 18. After this transient time, the oscillatory behavior in these plots becomes steady at a near linear periodic fashion.

Table 1: Summary of asymmetric canard parameters used in Validation Case 1.

Canard 1	**Canard 2**
$\Delta SL_{C_1} = -0.1429$ (ft)	$\Delta SL_{C_2} = 0.2071$ (ft)
$\Delta BL_{C_1} = 0.0698$ (ft)	$\Delta BL_{C_2} = 0.0590$ (ft)
$\Delta WL_{C_1} = 0.0240$ (ft)	$\Delta WL_{C_2} = 0.0244$ (ft)
$\phi_{C_1} = 19$ (deg)	$\phi_{C_2} = 37$ (deg)
$\delta_{C_1} = 1.00$ (deg)	$\delta_{C_2} = -0.33$ (deg)

Table 2: Summary of initial conditions used in Validation Case 1.

Kinematic States	**Dynamic States**
$x = 0.00$ (ft)	$V = 3357.0$ (ft/sec)
$y = 0.00$ (ft)	$p = 0.00$ (rad/sec)
$z = 0.00$ (ft)	$\tilde{v} = 0.00$ (ft/sec)
$\phi = 0.00$ (deg)	$\tilde{w} = 0.00$ (ft/sec)
$\theta = 1.0286$ (deg)	$\tilde{q} = 0.00$ (rad/sec)
$\psi = 0.00$ (deg)	$\tilde{r} = 0.00$ (rad/sec)

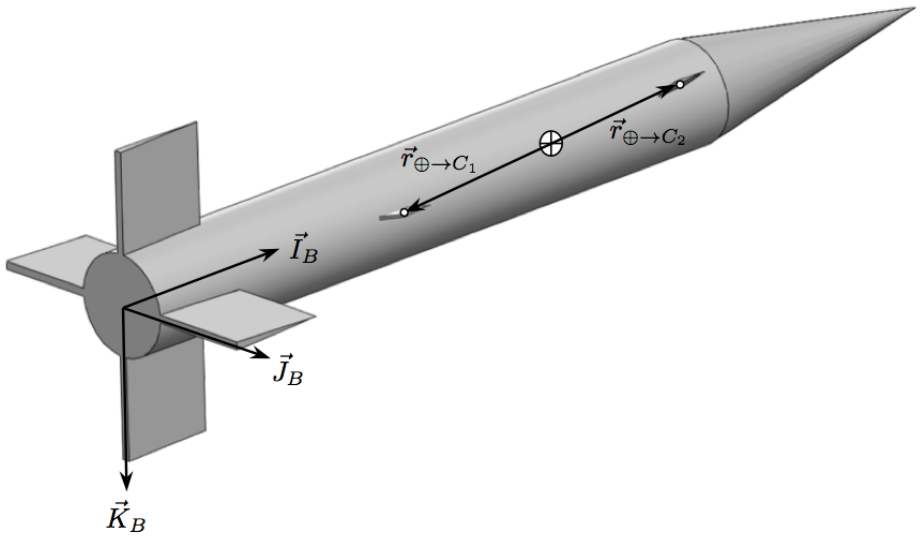

Figure 6: A schematic of the standard finned projectile configuration with two small asymmetric lifting surfaces, C1 and C2, which are superimposed aerodynamic models onto the standard finned projectile aerodynamics.

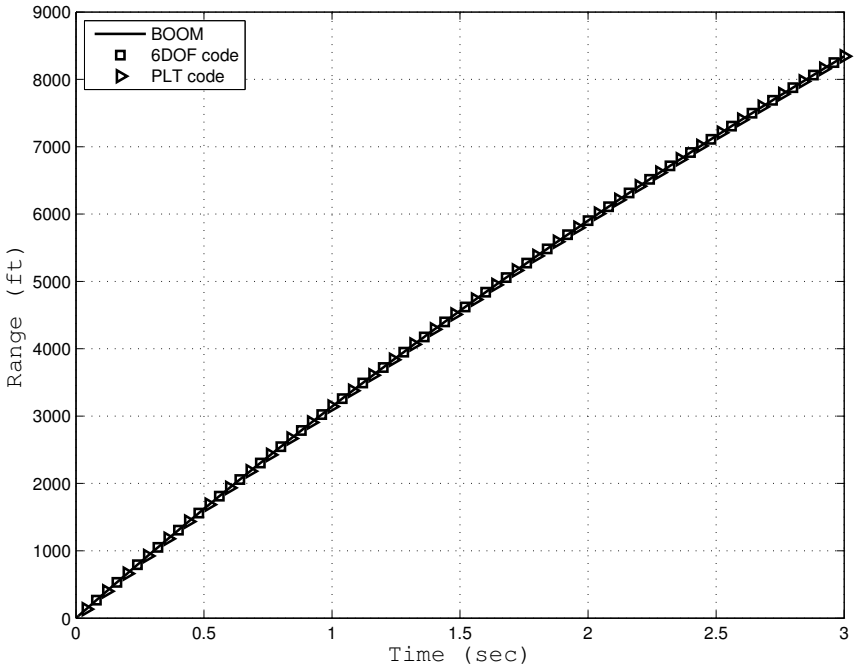

Figure 7: Validation Case 1 – Range vs Time

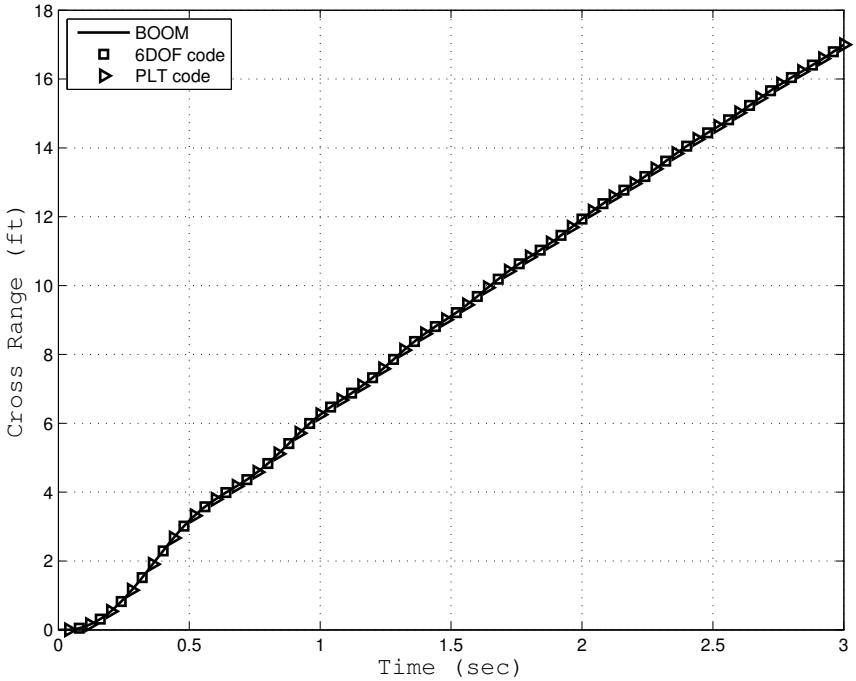

Figure 8: Validation Case 1 – Cross Range vs Time

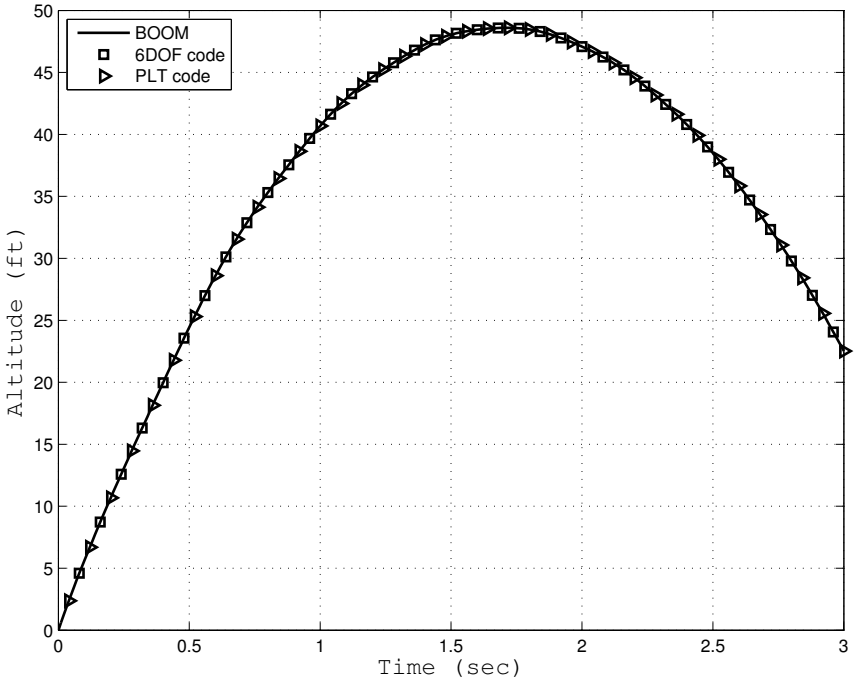

Figure 9: Validation Case 1 – Altitude vs Time

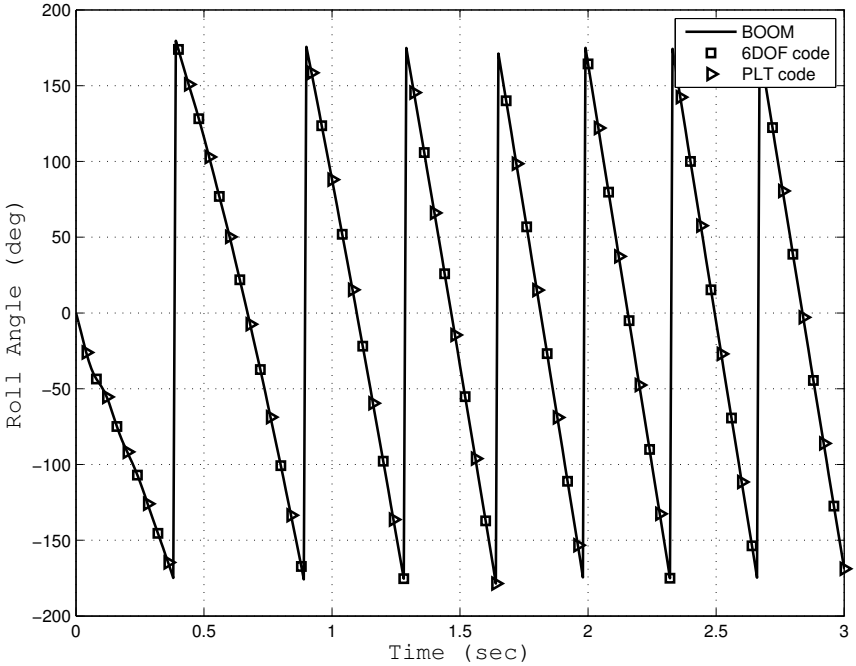

Figure 10: Validation Case 1 – Roll Angle vs Time

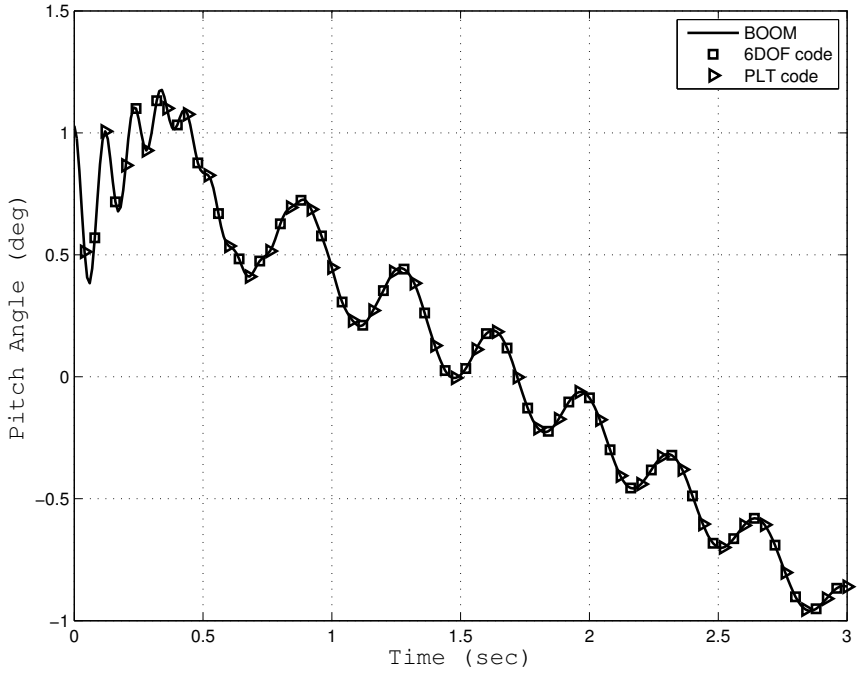

Figure 11: Validation Case 1 – Pitch Angle vs Time

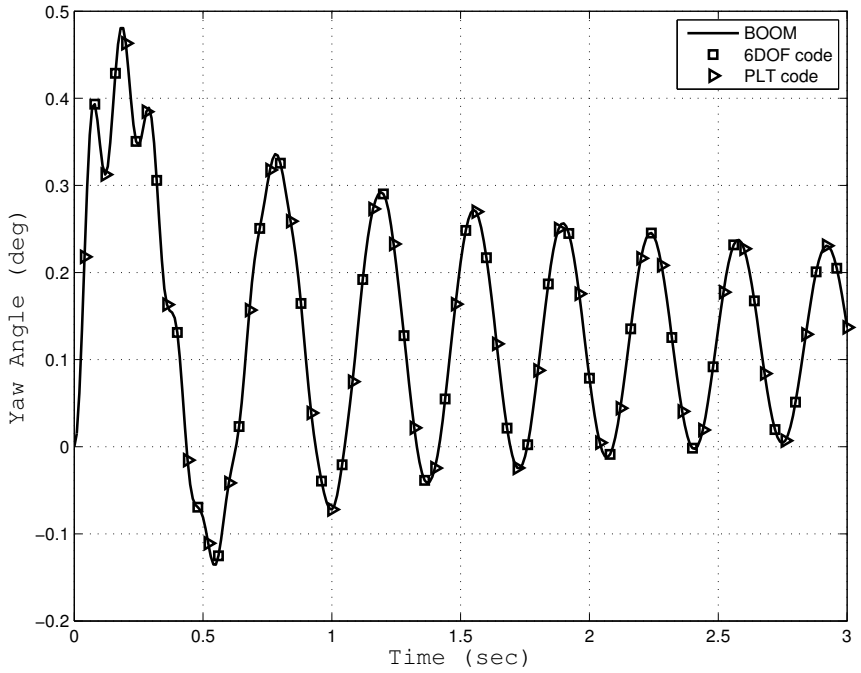

Figure 12: Validation Case 1 – Yaw Angle vs Time

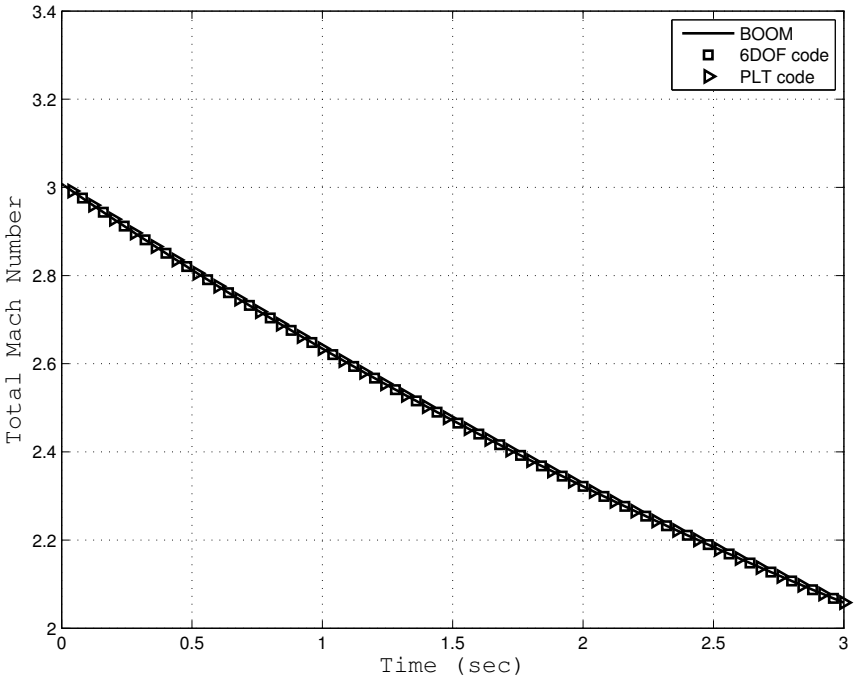

Figure 13: Validation Case 1 – Total Mach Number vs Time

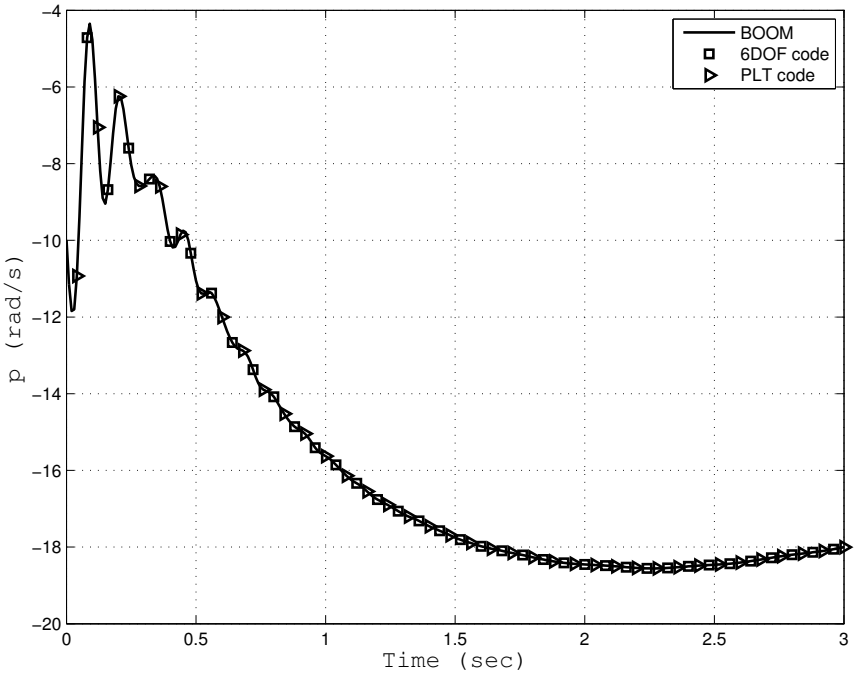

Figure 14: Validation Case 1 – Roll Rate vs Time

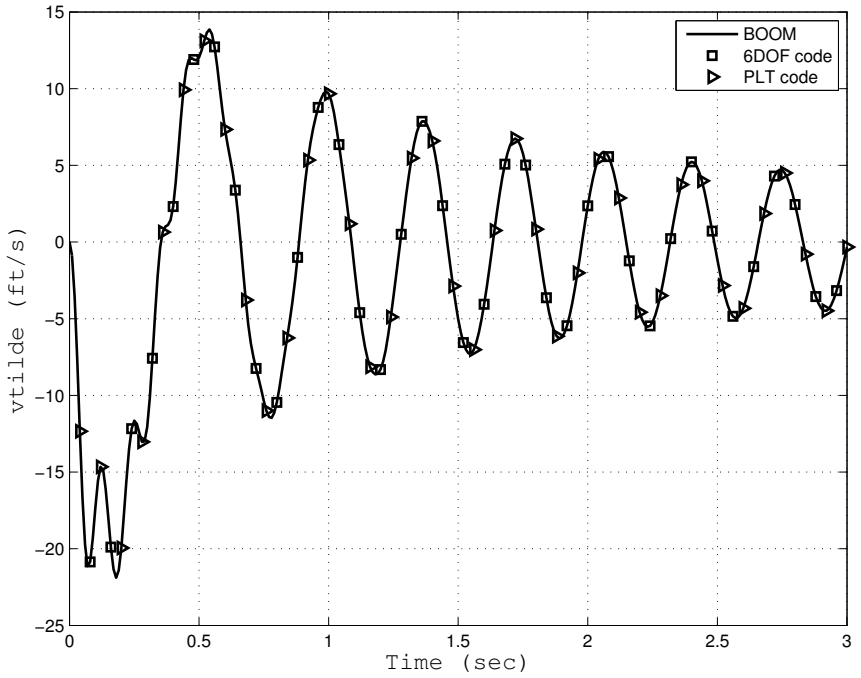

Figure 15: Validation Case 1 – Vtilde vs Time

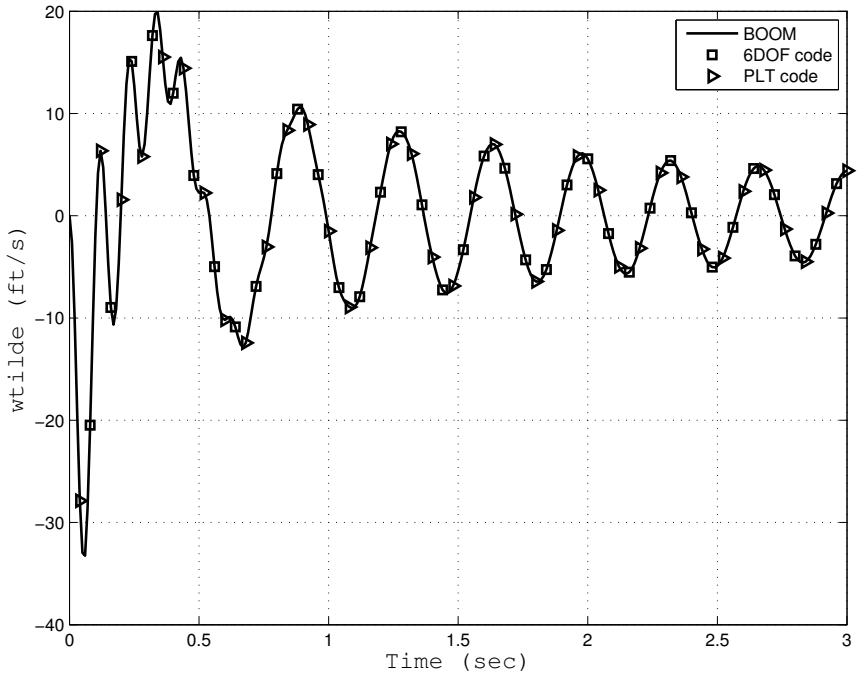

Figure 16: Validation Case 1 – Wtilde vs Time

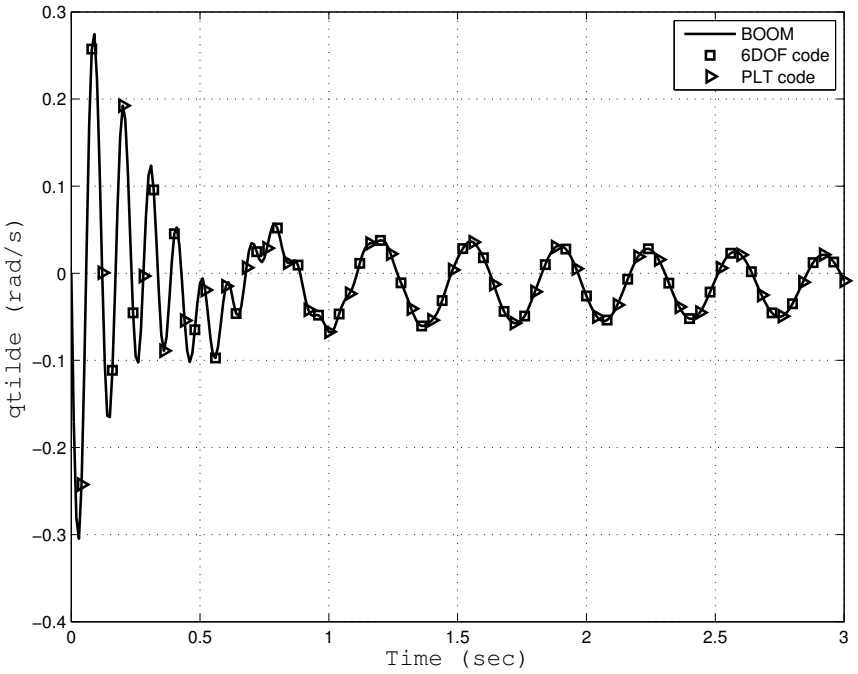

Figure 17: Validation Case 1 – Qtilde vs Time

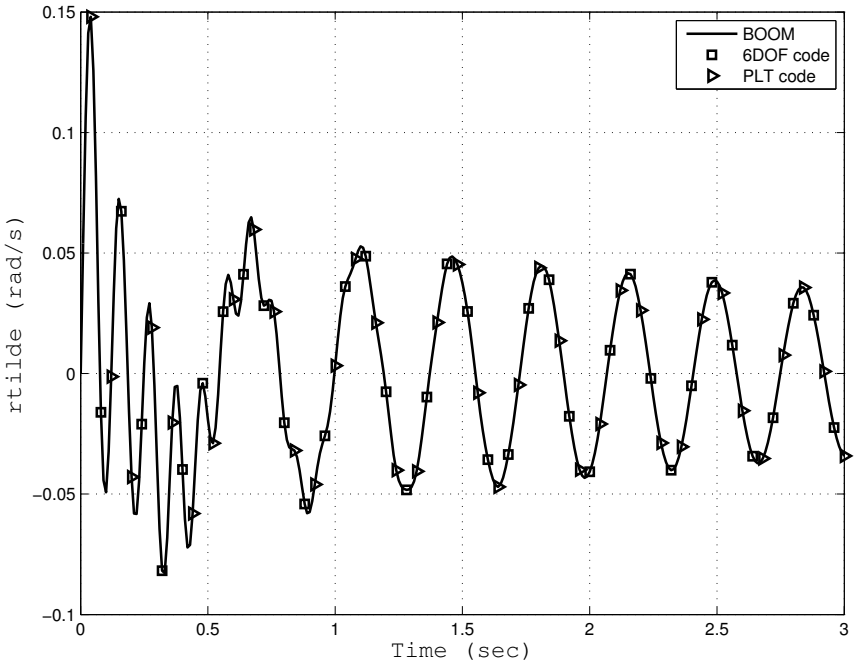

Figure 18: Validation Case 1 – Rtilde vs Time

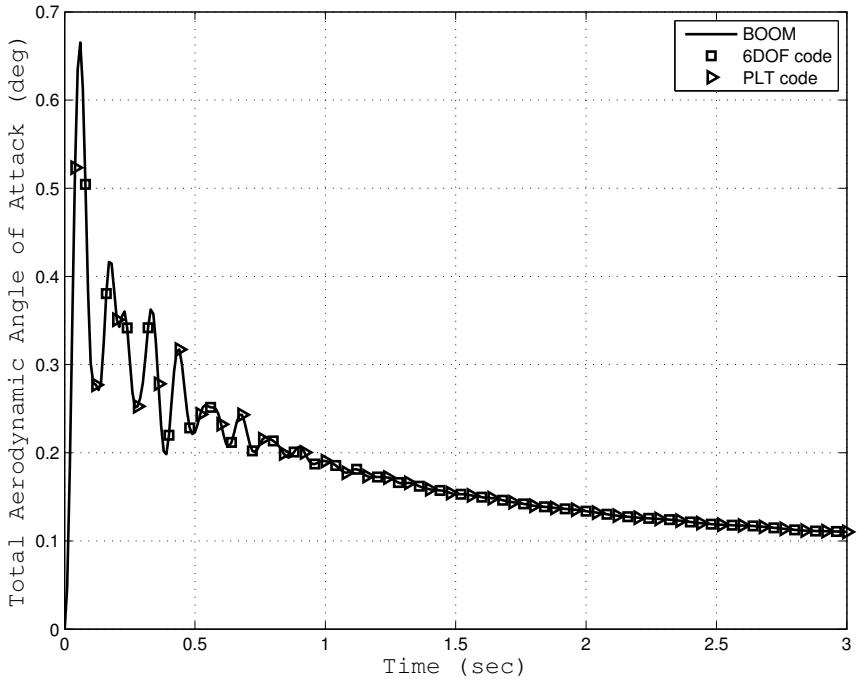

Figure 19: Validation Case 1 – Total Aerodynamic Angle of Attack vs Time

4.2 Case 2 – Full Aero vs Separated Aero Validations

Using the now validated 6DOF code, trajectory results were generated using a symmetric projectile to further confirm the accuracy of the lifting surface aerodynamic model. Figure 20 illustrates how the standard finned projectile can be physically described, using (1) the body aerodynamic model of Section (2.4.3) or (2) the lifting surface aerodynamic model of Section (2.4.4). In order to obtain the projectile description using the separated aerodynamic models, the aerodynamic data for the standard finned projectile is divided into lifting surface and body aerodynamic effects. *Appendix D* summarizes these calculations, and summarizes the results of reducing the projectile aerodynamic data down into respective body and lifting surface model contributions.

The trajectory results were generated for the symmetric projectile configuration launched at Mach 0.5 with a quadrant elevation of 1.0286 (deg). Three cases were

run for initial roll rates of 0.0, 1.0, and 10.0 (rad/sec). Figures 21–33 summarize these results, where excellent agreement between the separated and total aerodynamic models can be seen.

The trajectory results of Figures 21, 22, and 23 show that the differing initial roll rates cause a small amount of deflection in the cross range but does not significantly affect the projectile range and altitude. In Figures, 26, 29, and 32 the initial roll rates also cause differences in the lateral oscillatory amplitude of the yaw angle and lateral no-roll frame velocity and angular velocity states but the frequency remains unchanged. In the vertical plane, the states pitch angle and vertical no-roll frame velocity and angular velocity states of Figures 25, 30 and 31 show no significant differences between all cases. Also, variation between cases in the total aerodynamic angle of attack of Figure 33 is very small, which means that the lateral differences are insignificant in affecting the trajectory path yet can still be accurately accounted for by the lifting surface model.

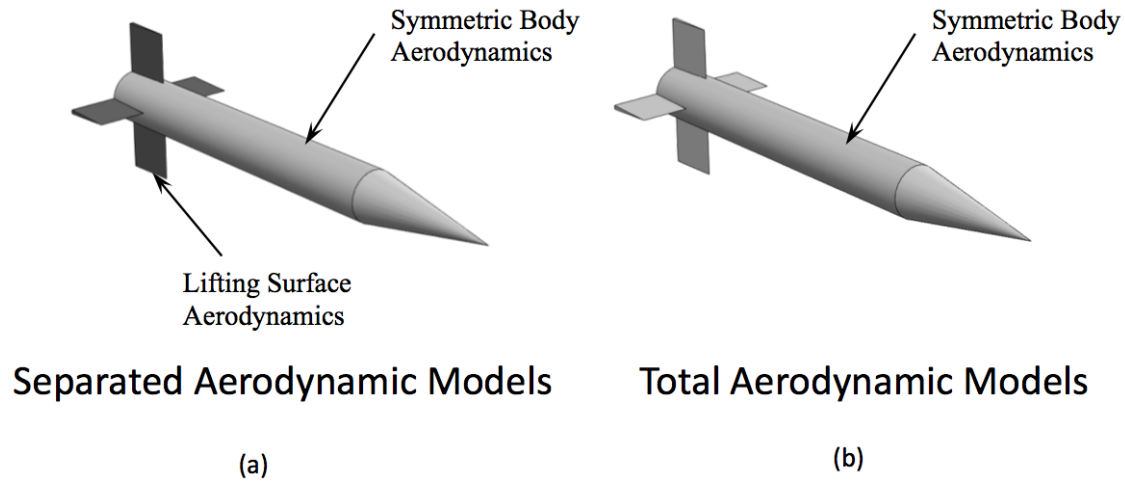

Figure 20: Illustrations of the standard Army-Navy finned projectile, where the externally exerted aerodynamic forces are (a) divided into body (light grey) and lifting surface (dark grey) aerodynamics and (b) left in the compact total body aerodynamic form.

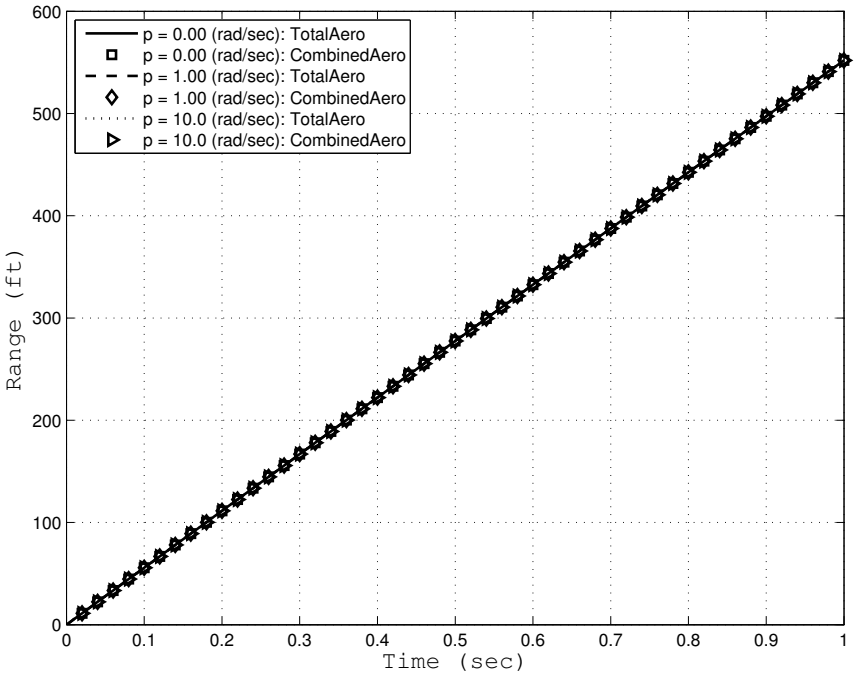

Figure 21: Validation Case 2 – Range vs Time

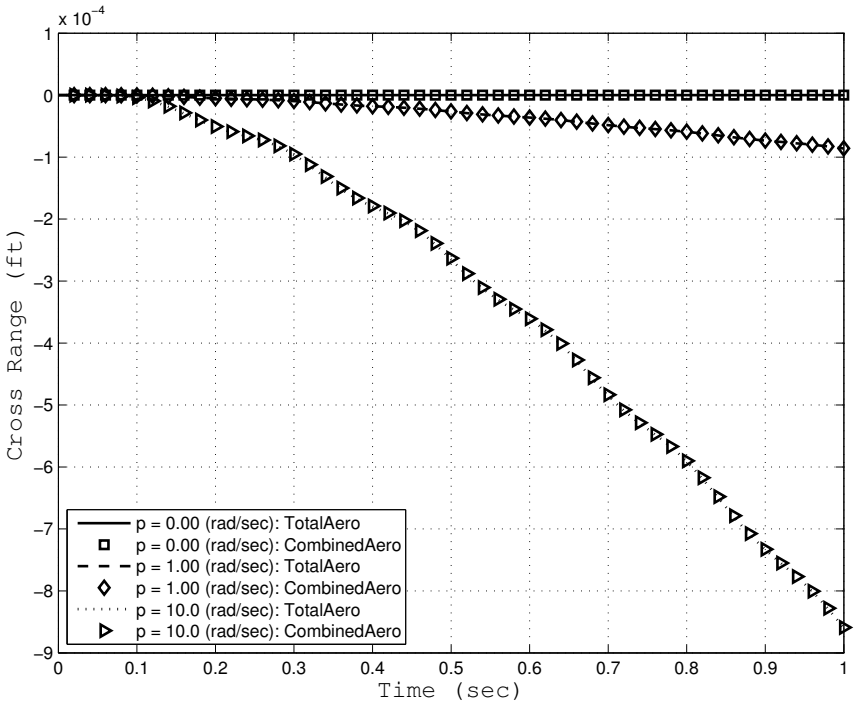

Figure 22: Validation Case 2 – Cross Range vs Time

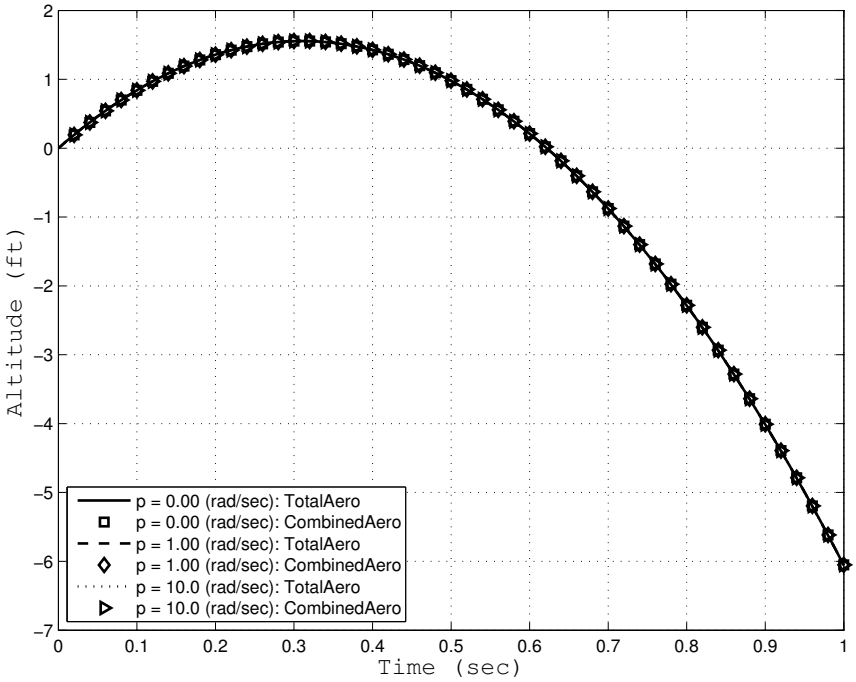

Figure 23: Validation Case 2 – Altitude vs Time

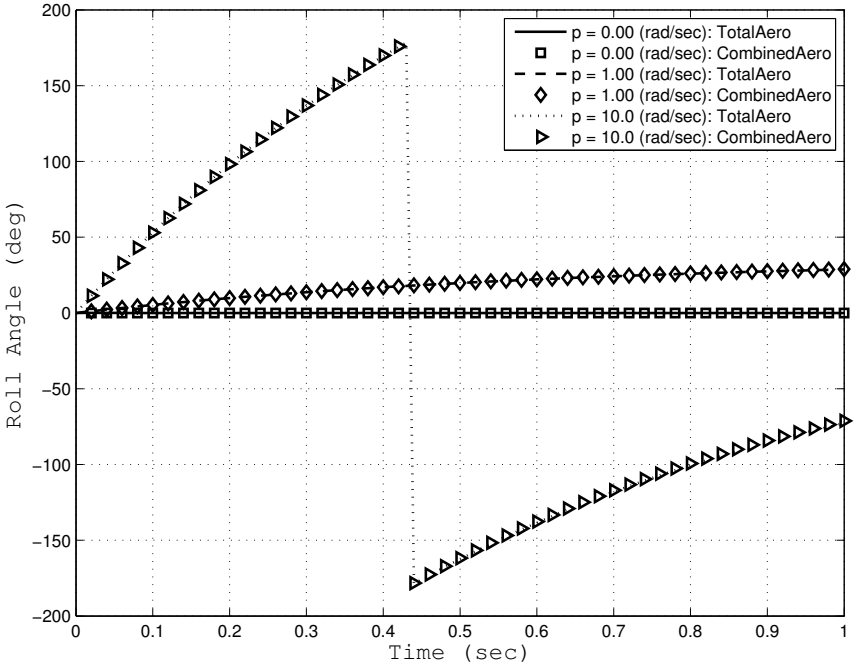

Figure 24: Validation Case 2 – Roll Angle vs Time

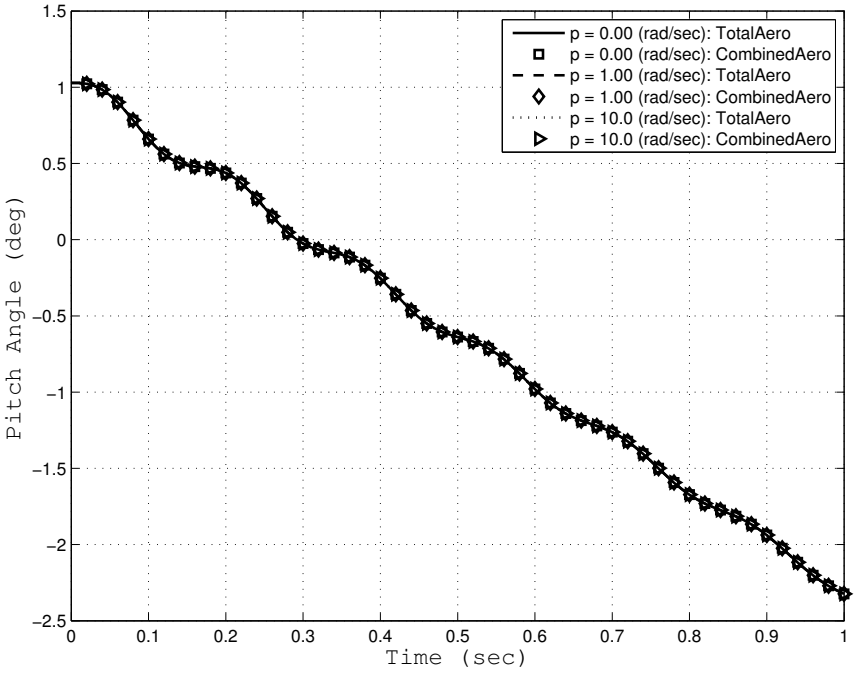

Figure 25: Validation Case 2 – Pitch Angle vs Time

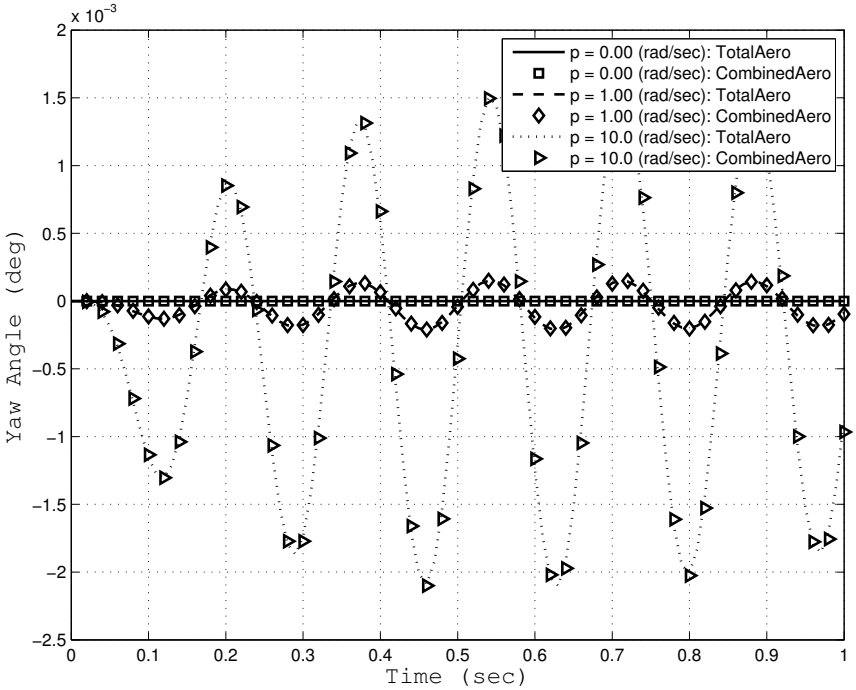

Figure 26: Validation Case 2 – Yaw Angle vs Time

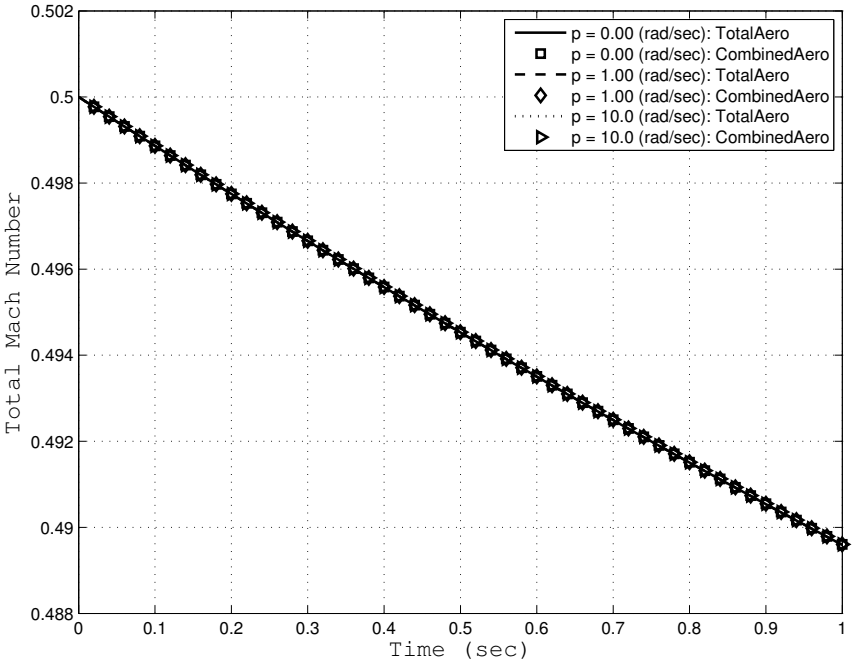

Figure 27: Validation Case 2 – Mach Number vs Time

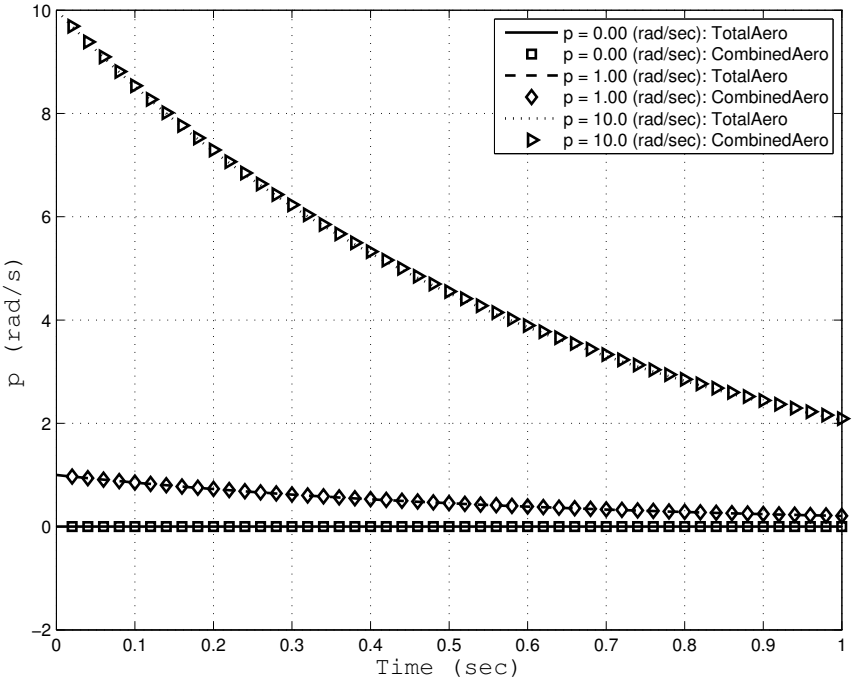

Figure 28: Validation Case 2 – Roll Rate vs Time

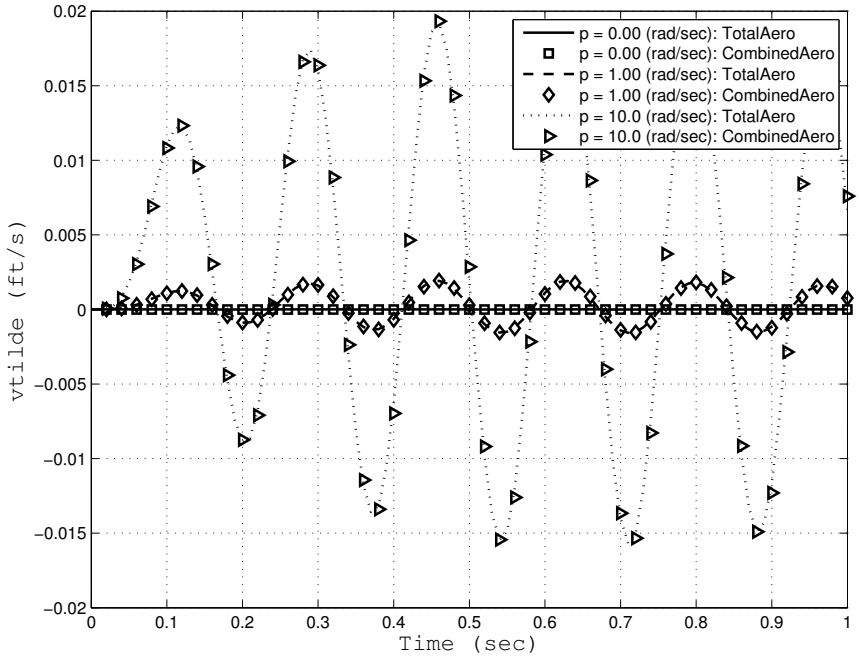

Figure 29: Validation Case 2 – Vtilde vs Time

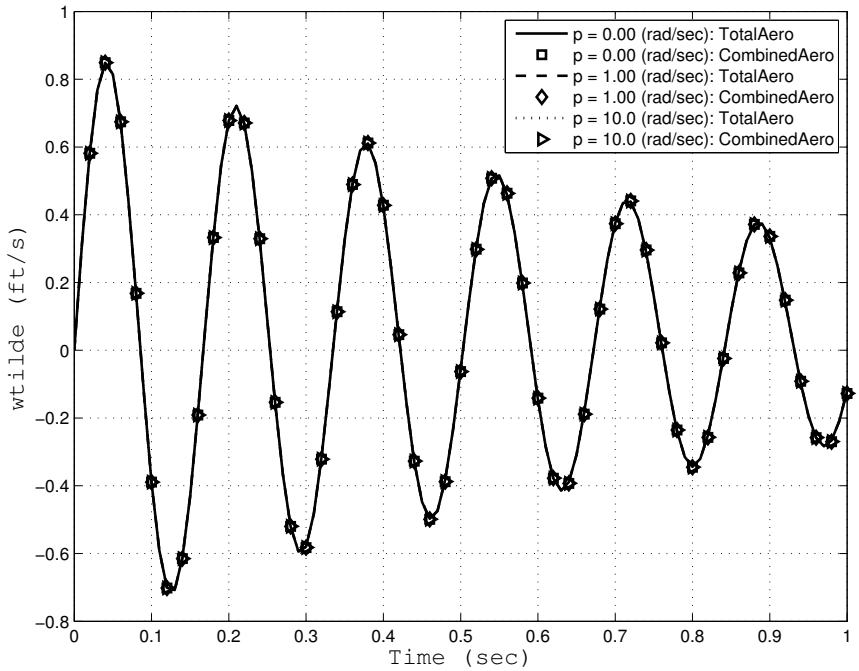

Figure 30: Validation Case 2 – Wtilde vs Time

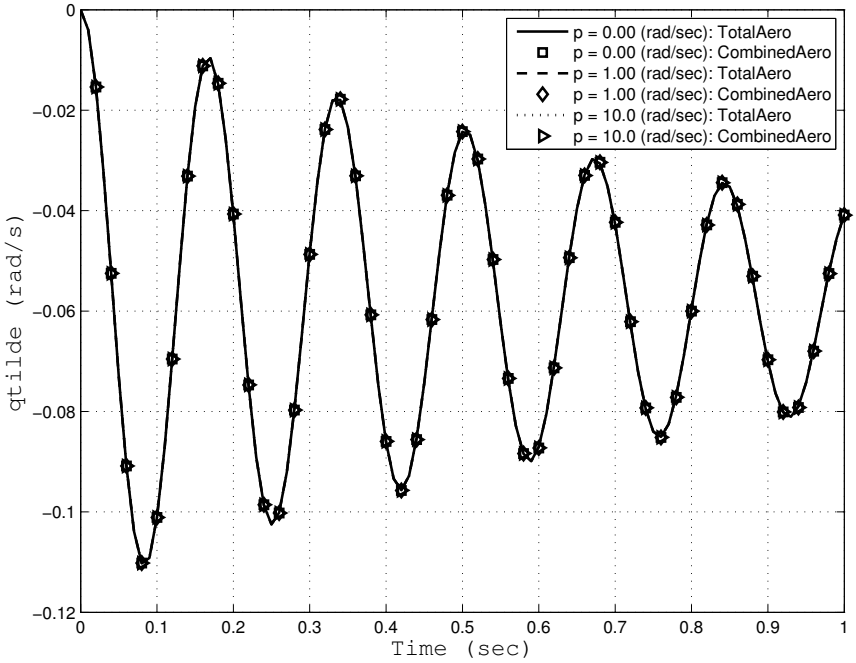

Figure 31: Validation Case 2 – Qtilde vs Time

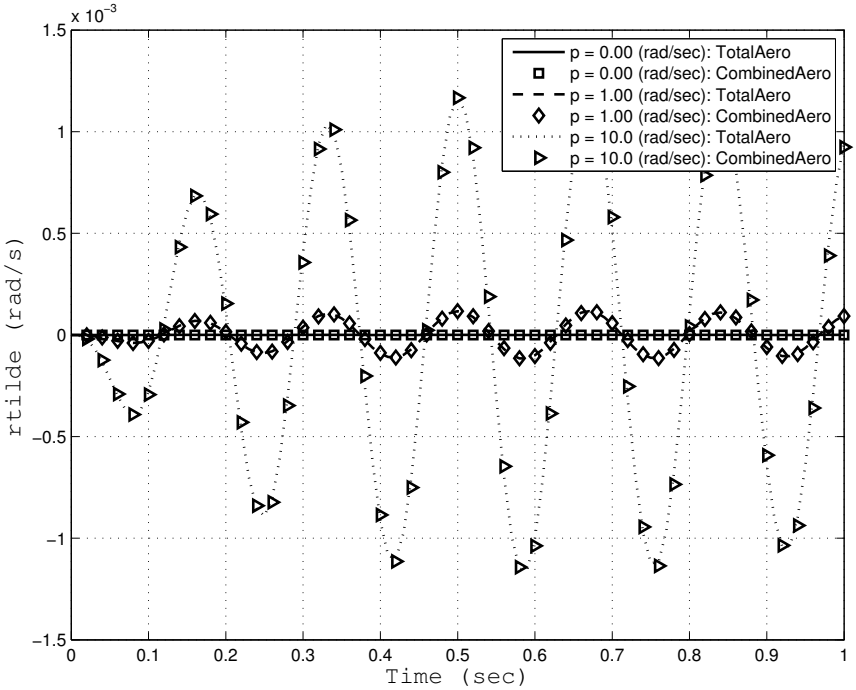

Figure 32: Validation Case 2 – Rtilde vs Time

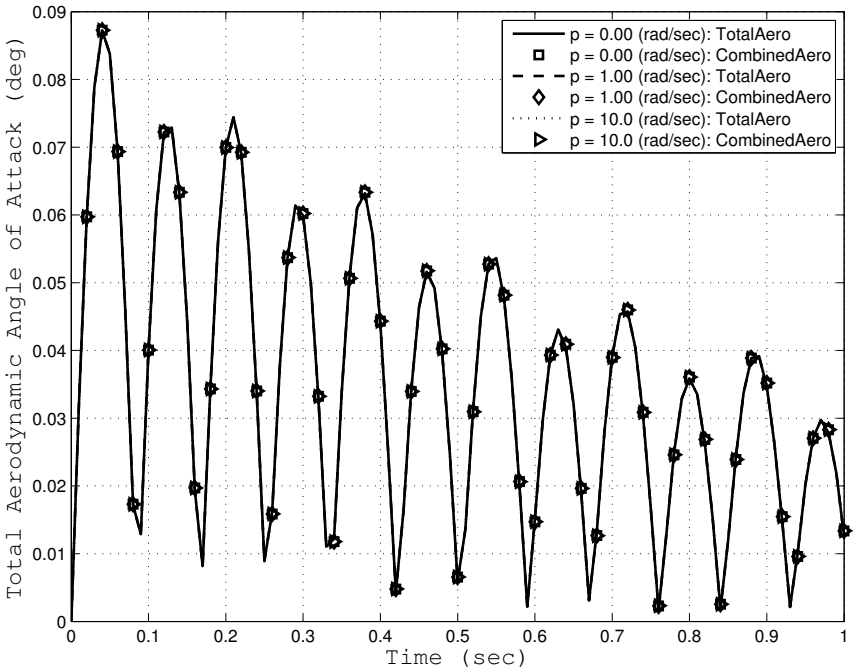

Figure 33: Validation Case 2 – Total Aerodynamic Angle of Attack vs Time

4.3 Case 3 – Comparison of Classical and Extended LTI Models for a Symmetric Projectile

One takeaway from the previous validation cases is that the extended PLT model, can accurately approximate the nonlinear flight dynamics of projectiles flying at small aerodynamic angles of attack. In extension to *Validation Case 2*, the current validation case will compare LTI approximations of the total aerodynamic and separated aerodynamic models to the equivalent 6DOF trajectory results for a symmetric projectile. The LTI approximations are created by holding the quasi-linear states ϕ_o, V_o, and p_o constant within the PLT matrix $\mathbf{A}$ of Equations (62) and (67) in *Chapter 2*. From *Chapter 3*, holding these states to be constant effectively sets $\mathbf{A}$ to be *time-invariant*, therefore creating the LTI approximations. Conveniently, the LTI approximations of the total aerodynamic and separated aerodynamic models from *Validation Case 2* are identically the equivalent classical and extended projectile linear theory models that were derived in *Chapter 2*. Additionally, θ_o is held constant

in the gravity terms of PLT Equations.

Figures 34–46 compare the 6DOF, classical LTI, and extended LTI model trajectory results for the symmetric standard finned projectile launched at Mach 0.5 with a quadrant elevation of 1.0286 (deg) and a roll rate of 0.0 (rad/sec). These results show that the LTI models closely approximate the 6DOF results through 1.0 (sec) of flight. Observing close LTI model approximation to the 6DOF model is good in that it establishes credibility to stability analyses. Also, in some linear control system applications, this infers better controller performance and efficiency, because the linear matrices **A** and **B** would be updated relatively infrequently.

The most noticeable deviation is observed in the total velocity time history in Figure 40. The nonlinear affects of this state cause error between LTI and 6DOF models, because the quasi-linear total velocity V_o appearing in the PLT matrix **A** is constant through flight. Therefore high drag projectile configurations with numerous lifting surface appendages will introduce more error than lower drag projectiles, since drag causes the projectile total velocity to decrease at a faster rate.

A final observation is that both LTI models generated identical results. Of course from *Chapter 2*, the extended LTI model is far more generalized to account for lifting surface aerodynamic effects; however, for symmetric projectiles the extended theory simplifies down to classical linear theory. This result agrees with the intuition gained from the previous validation case and confirms that while the quasi-linear states ϕ_o, V_o, and p_o frequently appear within the extended PLT matrix **A** of Equation (67), the extended LTI drastically simplifies for symmetric projectiles.

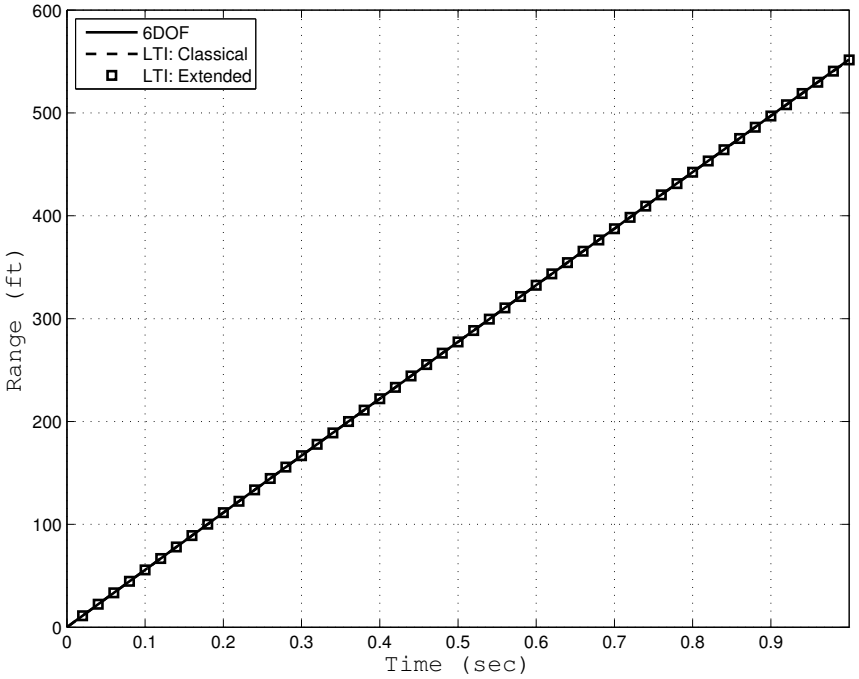

Figure 34: Validation Case 3 – Range vs Time

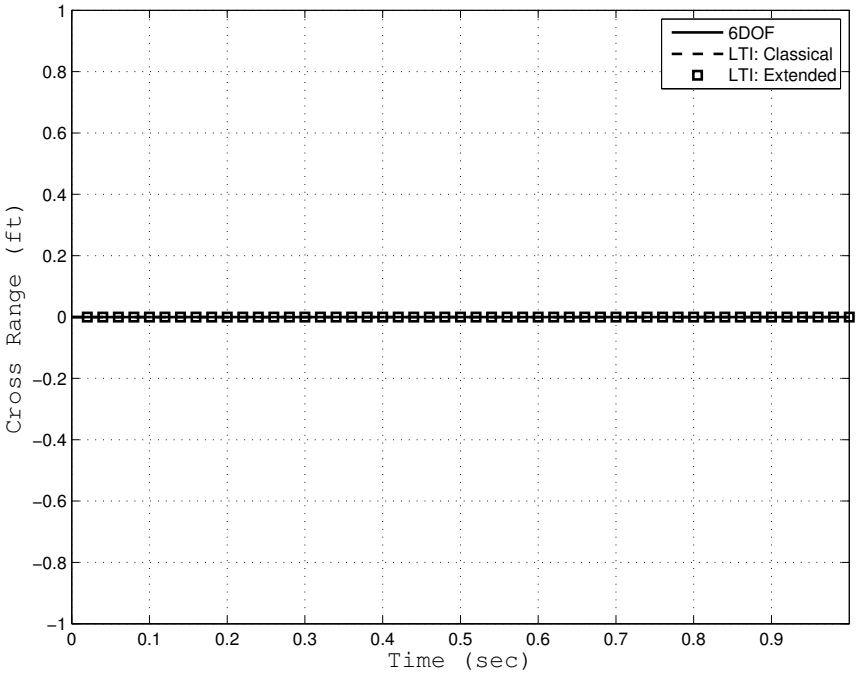

Figure 35: Validation Case 3 – Cross Range vs Time

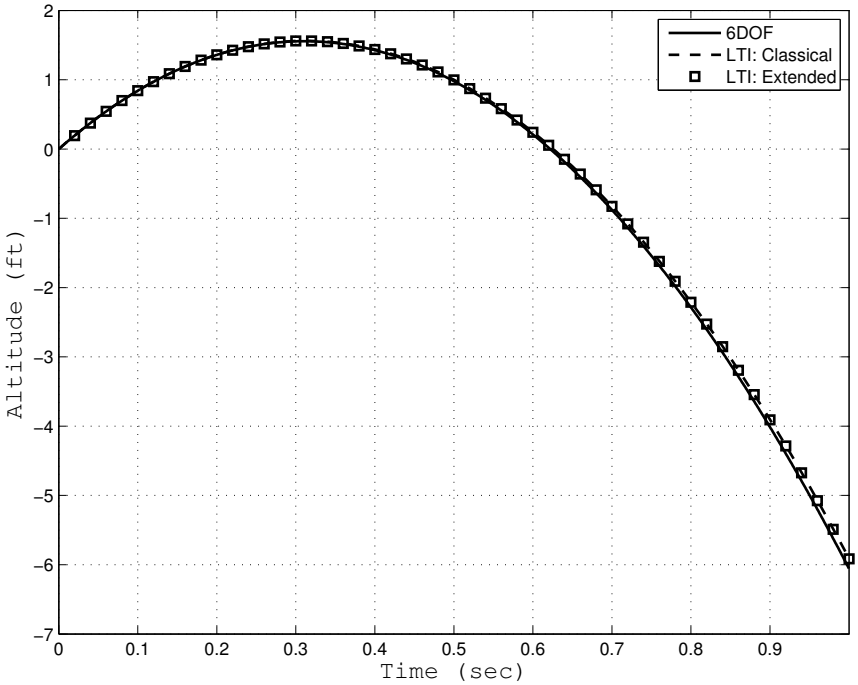

Figure 36: Validation Case 3 – Altitude vs Time

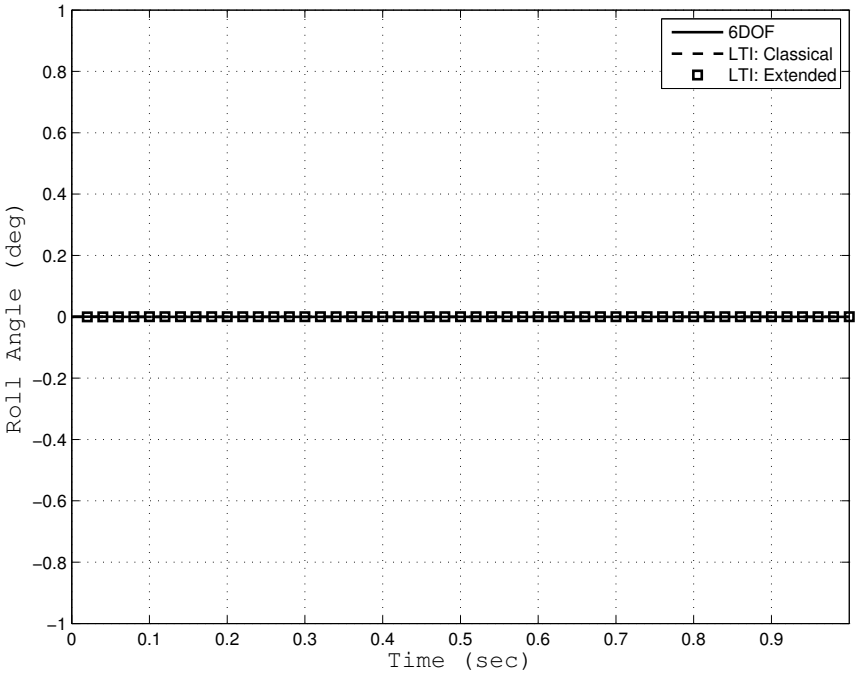

Figure 37: Validation Case 3 – Roll Angle vs Time

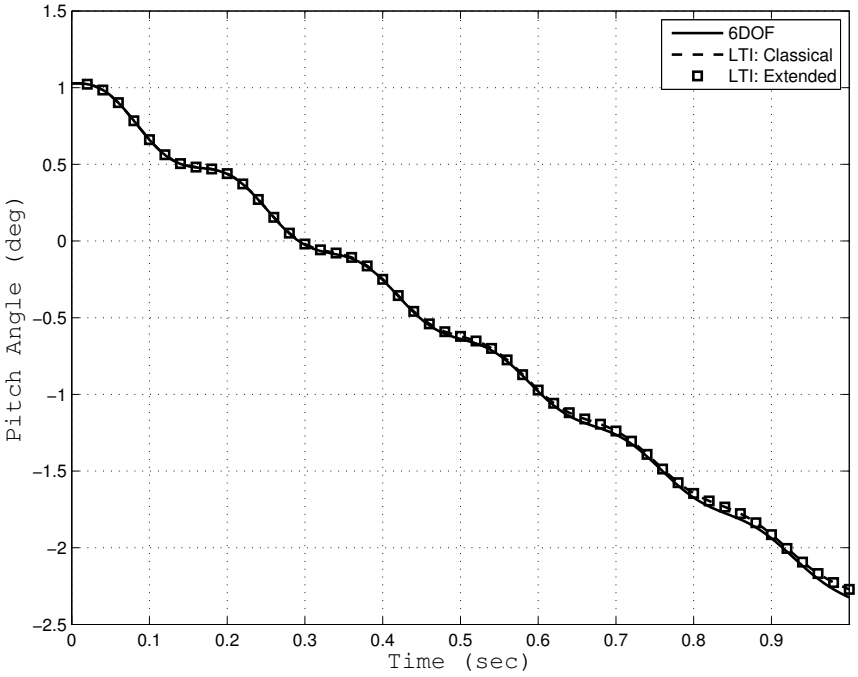

Figure 38: Validation Case 3 – Pitch Angle vs Time

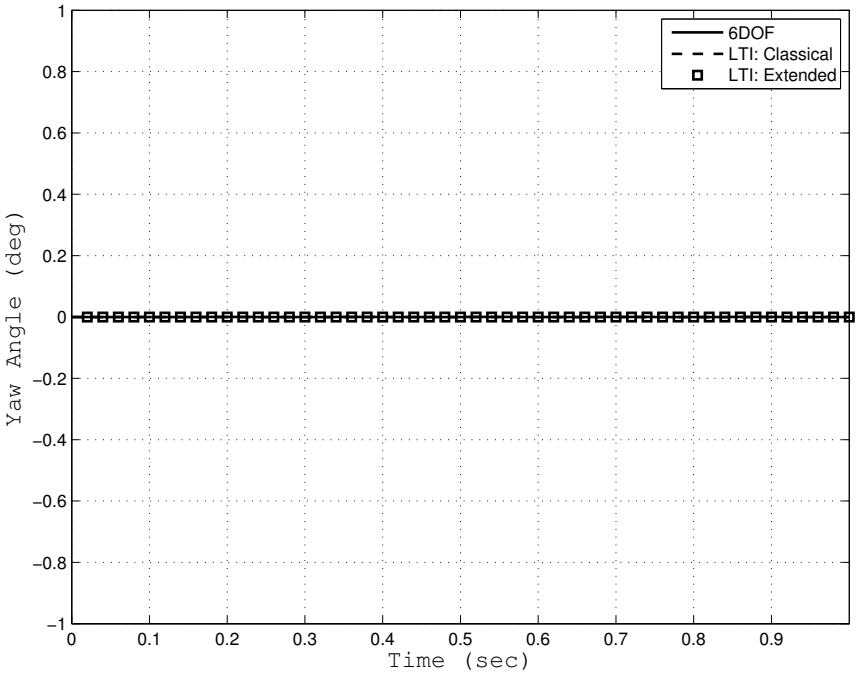

Figure 39: Validation Case 3 – Yaw Angle vs Time

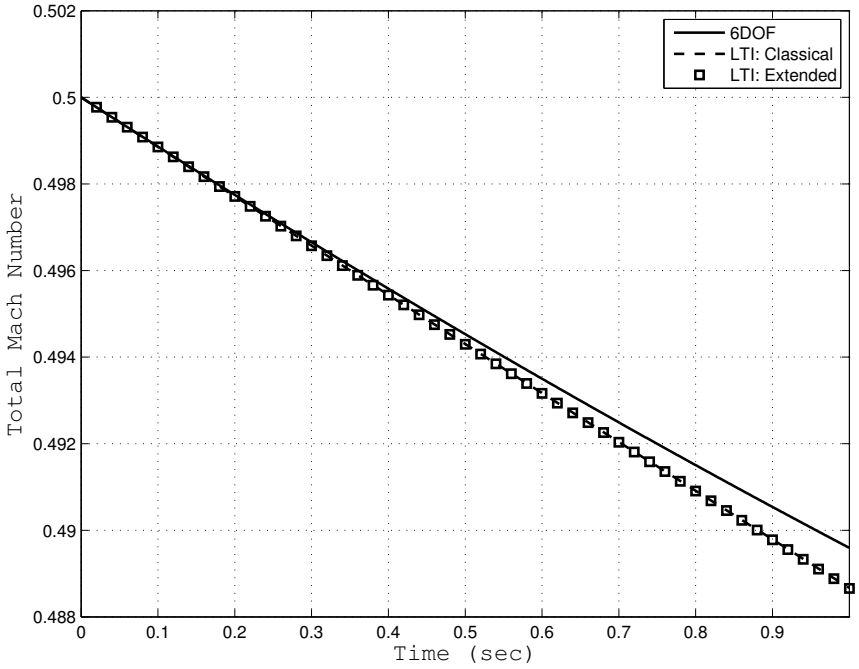

Figure 40: Validation Case 3 – Mach Number vs Time

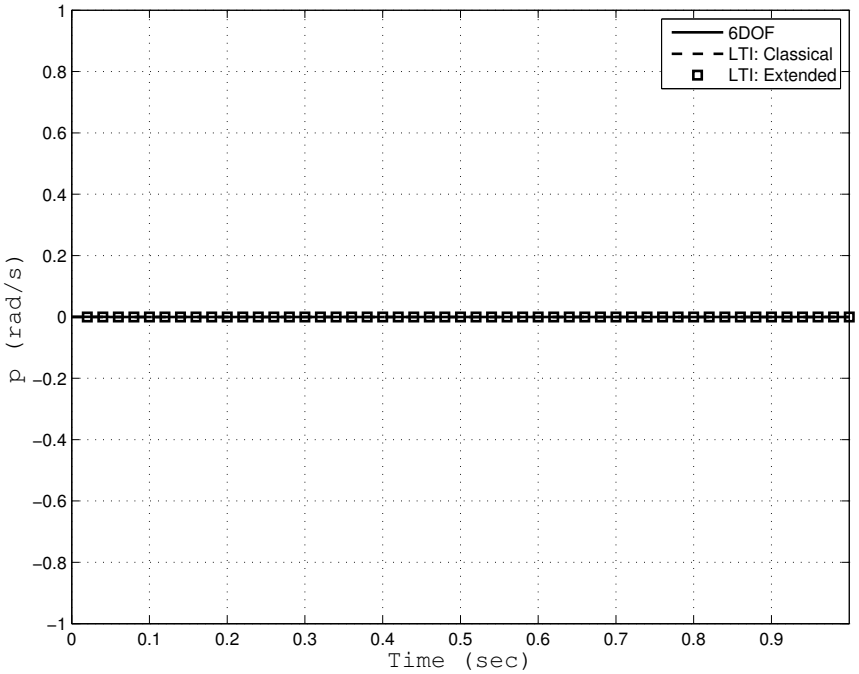

Figure 41: Validation Case 3 – Roll Rate vs Time

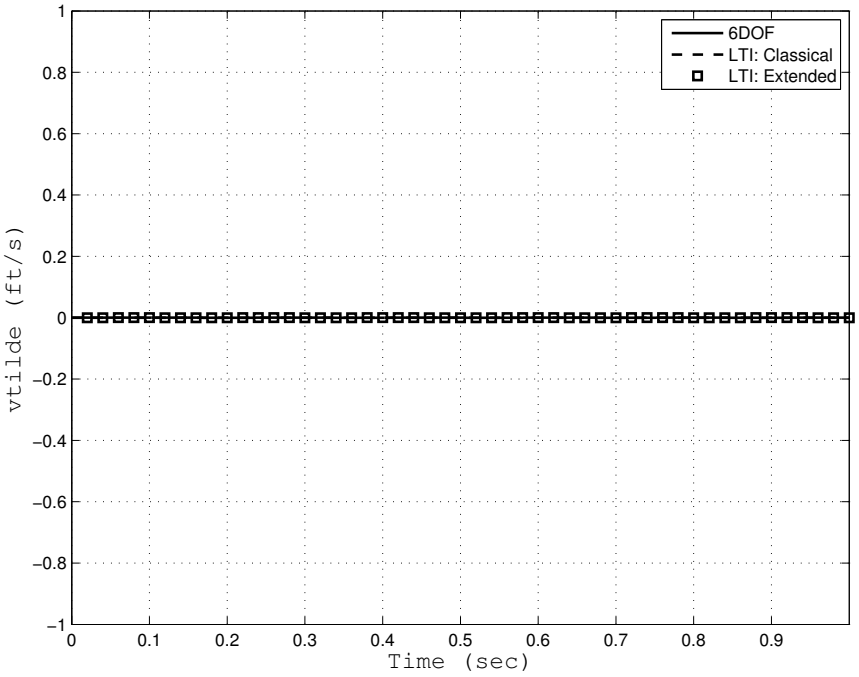

Figure 42: Validation Case 3 – Vtilde vs Time

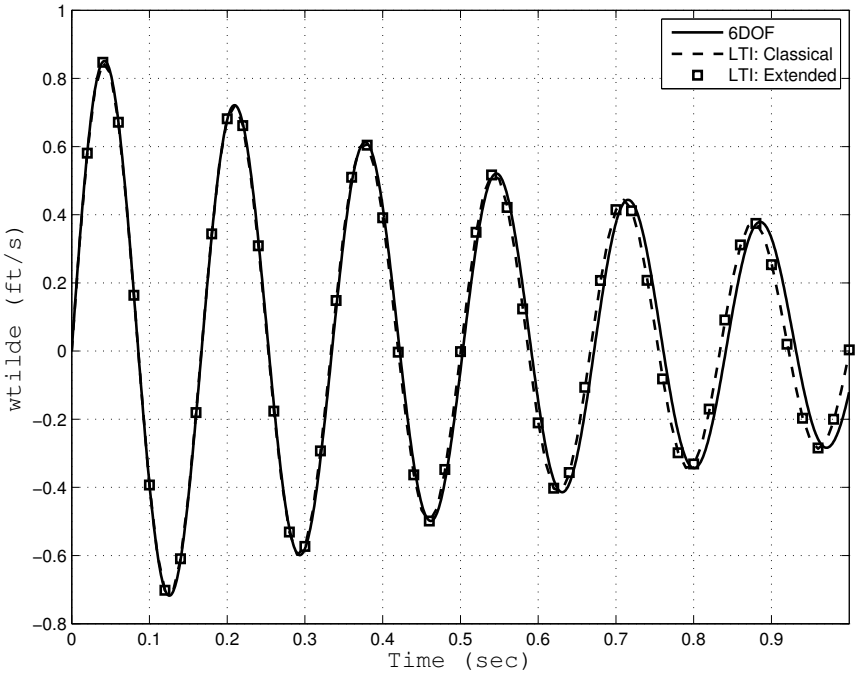

Figure 43: Validation Case 3 – Wtilde vs Time

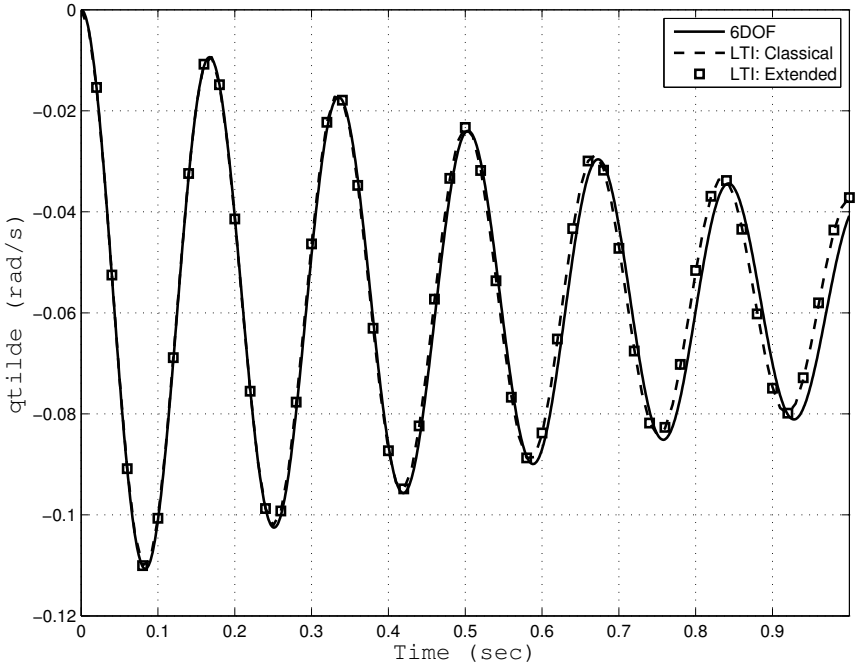

Figure 44: Validation Case 3 – Qtilde vs Time

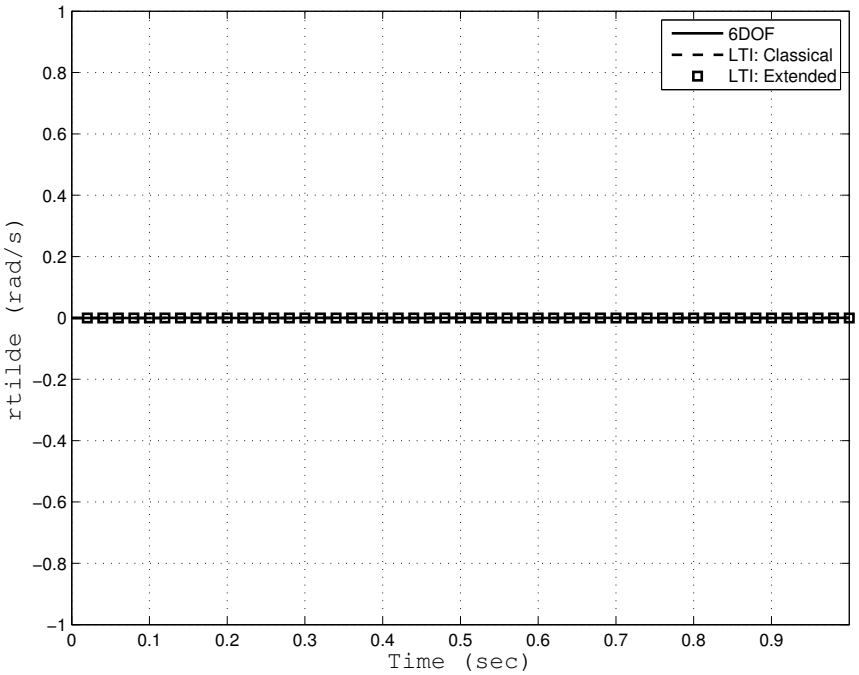

Figure 45: Validation Case 3 – Rtilde vs Time

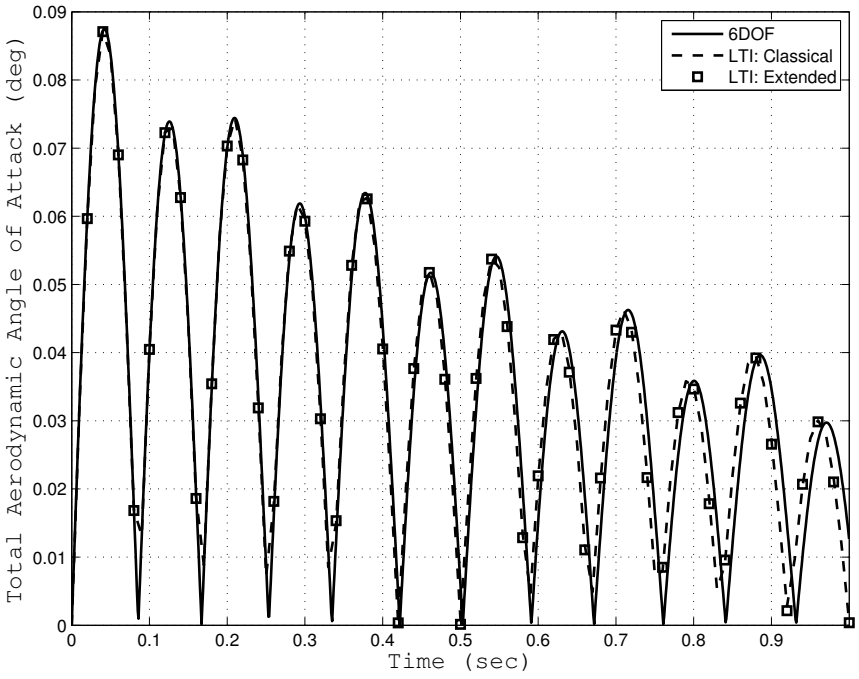

Figure 46: Validation Case 3 – Total Aerodynamic Angle of Attack vs Time

4.4 Case 4 – Comparison of LTI and LTP Models for an Asymmetric Projectile

In this validation case linearized dynamic models are generated for an asymmetric projectile and compared to 6DOF simulation results. As done in the previous validation case, the LTI model was generated by setting the quasi-linear states, p_o, V_o, ϕ_o, and θ_o to constant values of the initial conditions. Similarly, the LTP model was generated by expressing ϕ as a linear function of time within the PLT matrix $\mathbf{A}$, as shown in Equation (67) of Section (3.2). Recall that by expressing ϕ in this form, the extended PLT matrix $\mathbf{A}$ is periodic in time (since $\phi(t)$ only appears inside trig functions). Thus, for LTP systems *Floquet* theory might be used to evaluate projectile stability.

The projectile testbed with two asymmetrically placed lifting surfaces from *Validation Case 1* is again used, as well as the initial conditions in Table 3. Figures 47–59 compare simulation results from 6DOF, PLT (quasi-linear), LTI, and LTP models. In

contrast to the previous validation case, both the LTI and LTP models do not closely approximate the 6DOF/PLT simulation results over the entire time interval of 1.0 (sec), but in general the LTP model outperforms the LTI model approximations.

In Figure 48, the LTP model approximates the cross range for nearly 0.5 (sec), while the LTI model diverges after only 0.2 (sec). Figure 49 shows that the LTP and LTI models diverge from the altitude after 0.3 (sec) and 0.4 (sec), respectively. In Figure 50 the LTI and LTP models diverge from the roll angle after approximately 0.2 (sec), where the 6DOF model shows that the roll angle does not vary at an approximately linear rate, as assumed by the LTP model. The Euler pitch and yaw angle plots show that the LTP model is a better approximation of the 6DOF than the LTI model. There is minimal divergence in the Mach number plots of Figure 53; however, the roll rate in Figure 54 shows that both the LTI and LTP models diverge after 0.1 (sec). Throughout the epicyclic states in Figures 54–58 the LTI and LTP models vary in performance for this projectile.

Since the Mach number is very well approximated over the 1.0 (sec) interval, the quasi-linear roll angle ϕ_o and roll rate p_o states are observed to be the primary sources of error. Thus, the ability of the LTI and LTP models to approximate the 6DOF results is greatly reduced if the asymmetries cause irregular roll angle behavior caused most likely by a fast changing roll rate. For asymmetric projectiles where roll stability is designed for, an LTI model where $p_o = 0.0$ (rad/sec) could still perform very well; however, this will need to be determined on a case-by-case basis.

Table 3: Summary of initial conditions used in Validation Case 4.

Kinematic States	**Dynamic States**
$x = 0.00$ (ft)	$V = 3357.0$ (ft/sec)
$y = 0.00$ (ft)	$p = -3.00$ (rad/sec)
$z = 0.00$ (ft)	$\tilde{v} = 0.00$ (ft/sec)
$\phi = 0.00$ (deg)	$\tilde{w} = 0.00$ (ft/sec)
$\theta = 1.0286$ (deg)	$\tilde{q} = 0.00$ (rad/sec)
$\psi = 0.00$ (deg)	$\tilde{r} = 0.00$ (rad/sec)

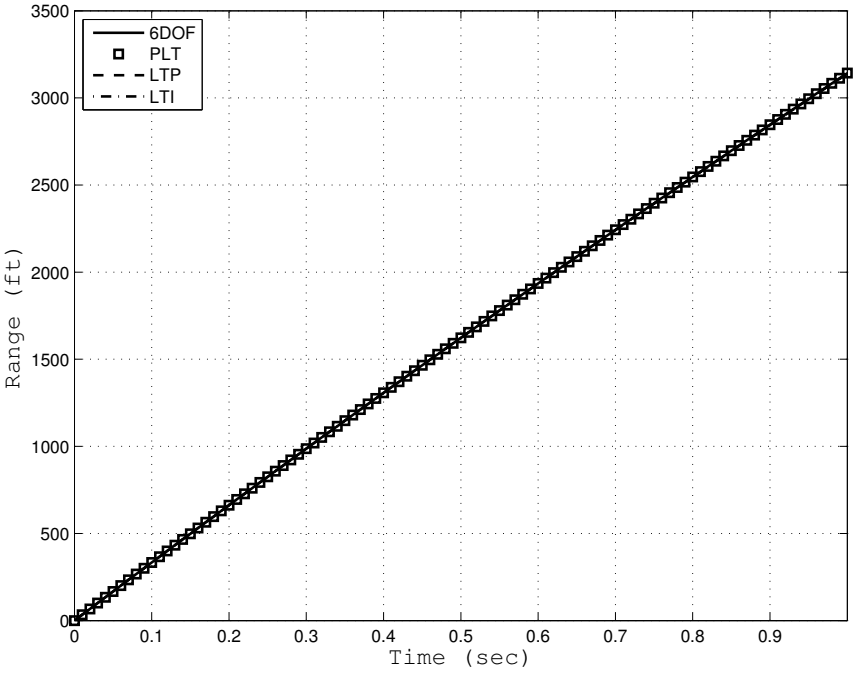

Figure 47: Validation Case 4 – Range vs Time

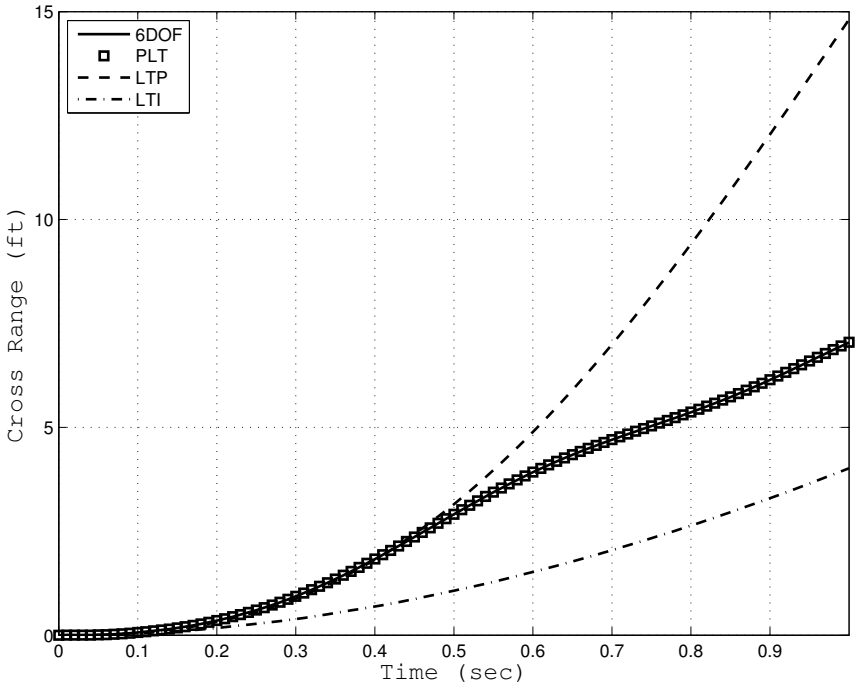

Figure 48: Validation Case 4 – Cross Range vs Time

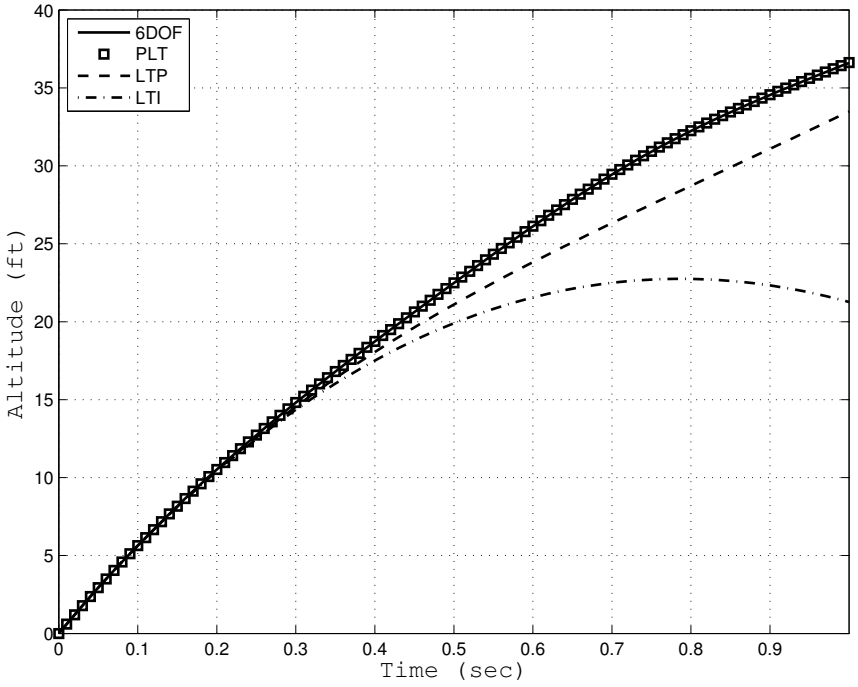

Figure 49: Validation Case 4 – Altitude vs Time

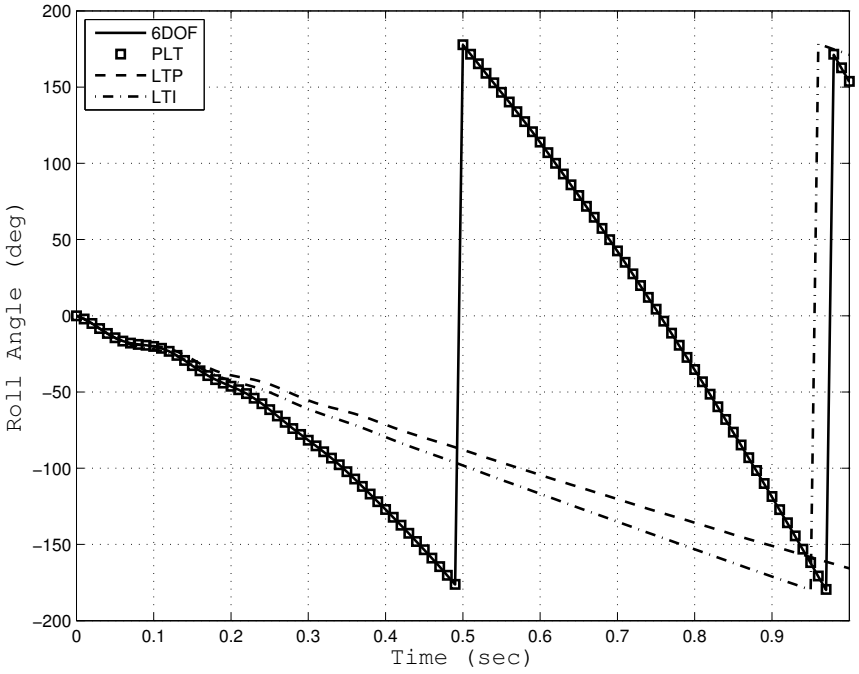

Figure 50: Validation Case 4 – Roll Angle vs Time

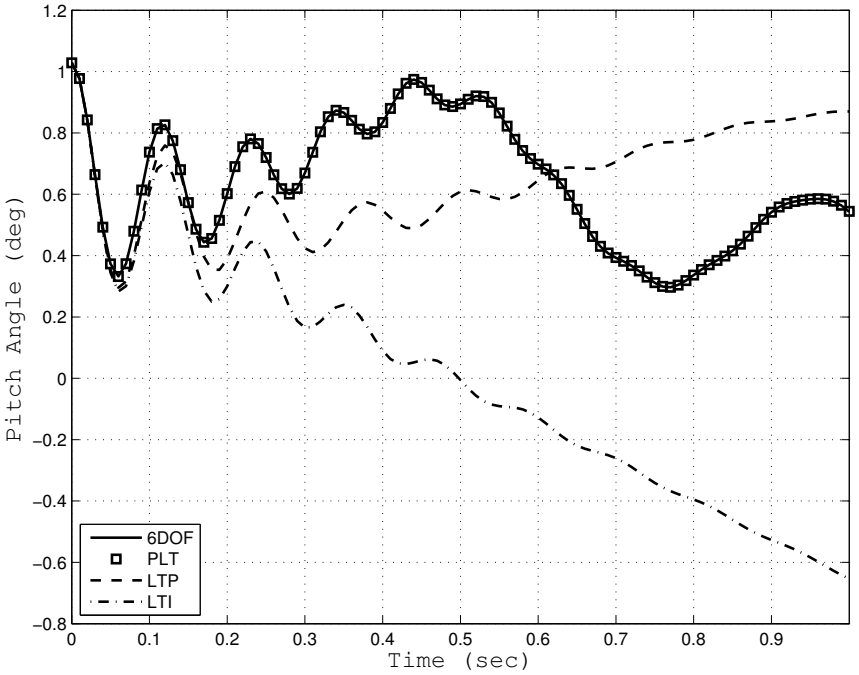

Figure 51: Validation Case 4 – Pitch Angle vs Time

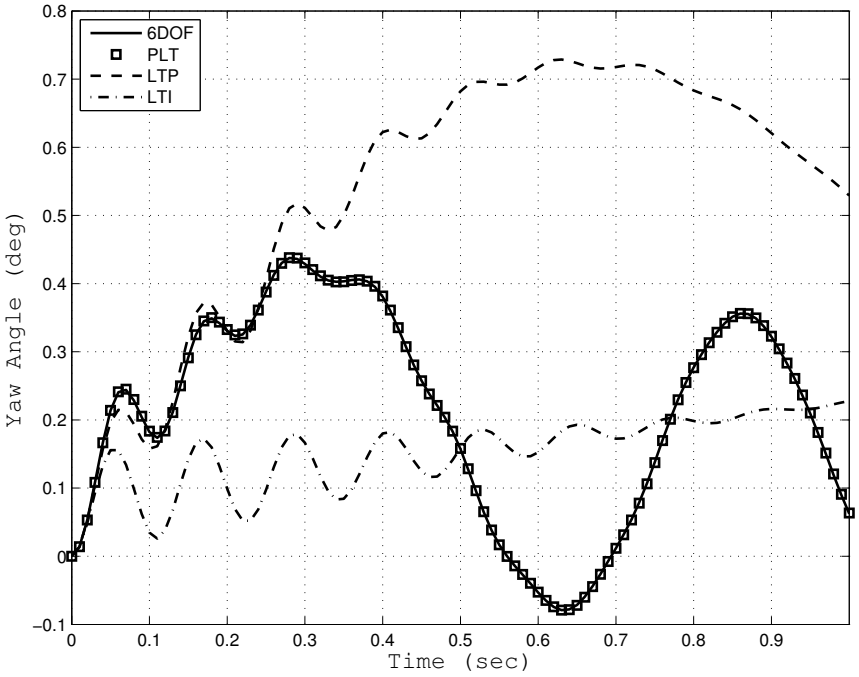

Figure 52: Validation Case 4 – Yaw Angle vs Time

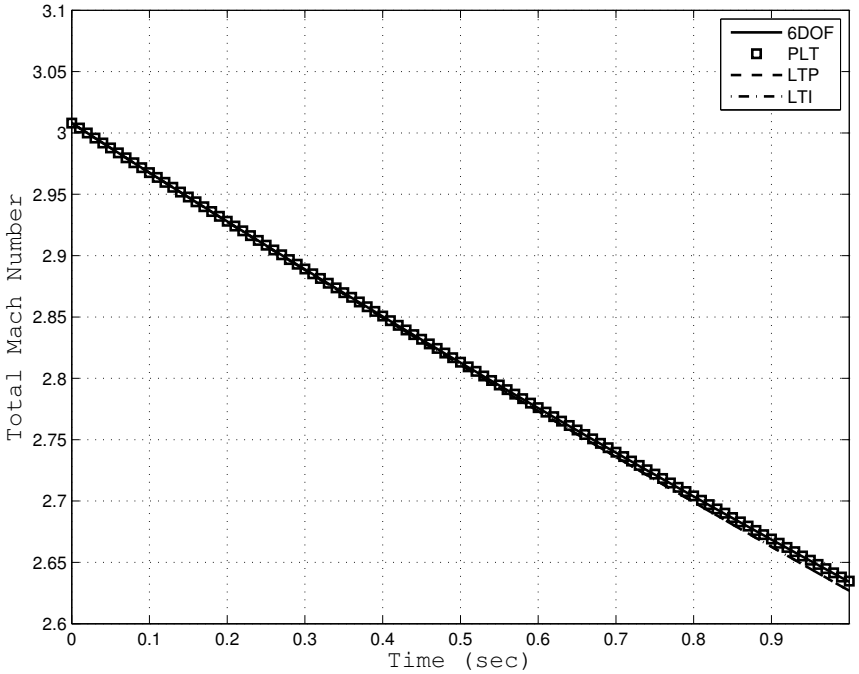

Figure 53: Validation Case 4 – Mach Number vs Time

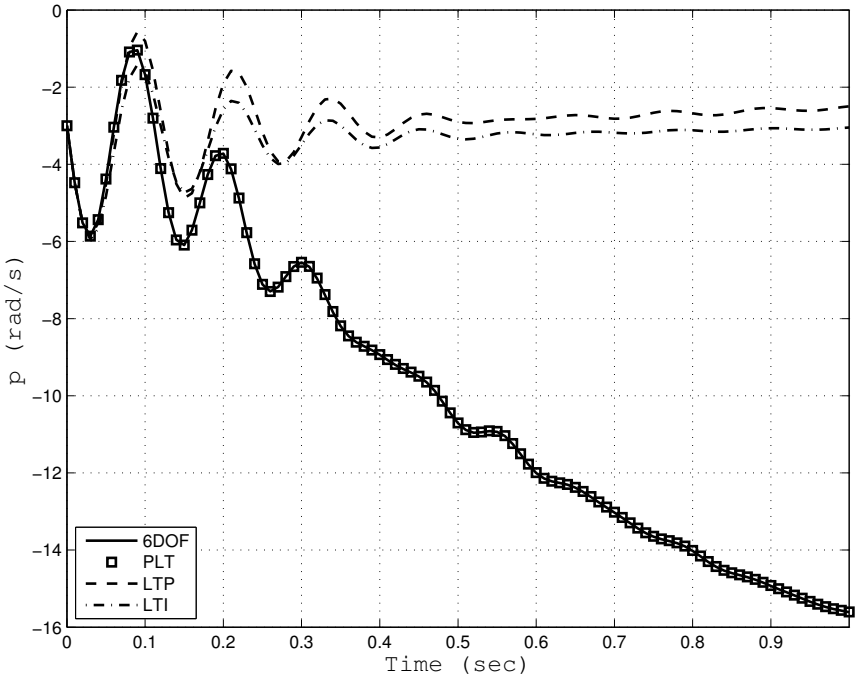

Figure 54: Validation Case 4 – Roll Rate vs Time

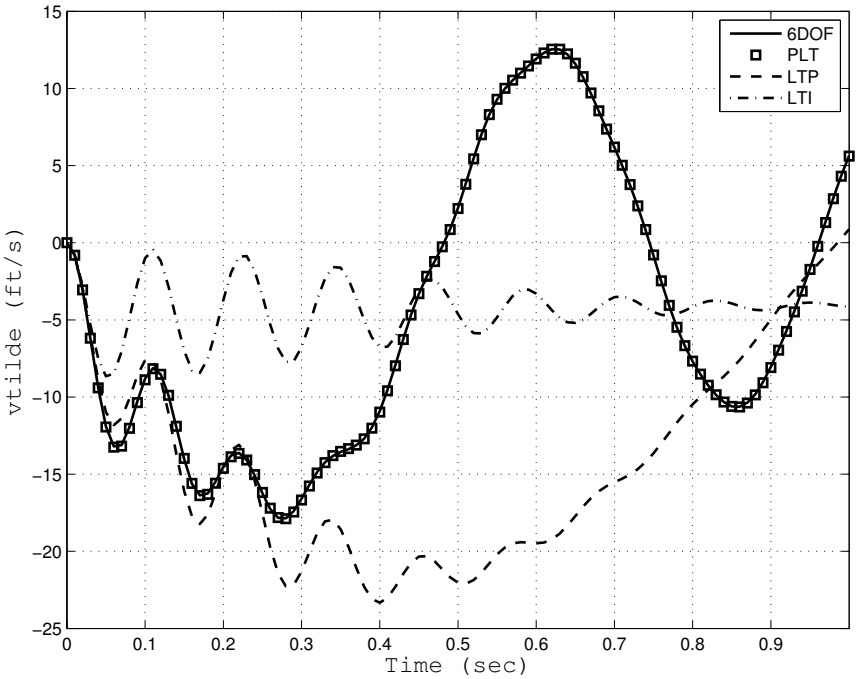

Figure 55: Validation Case 4 – Vtilde vs Time

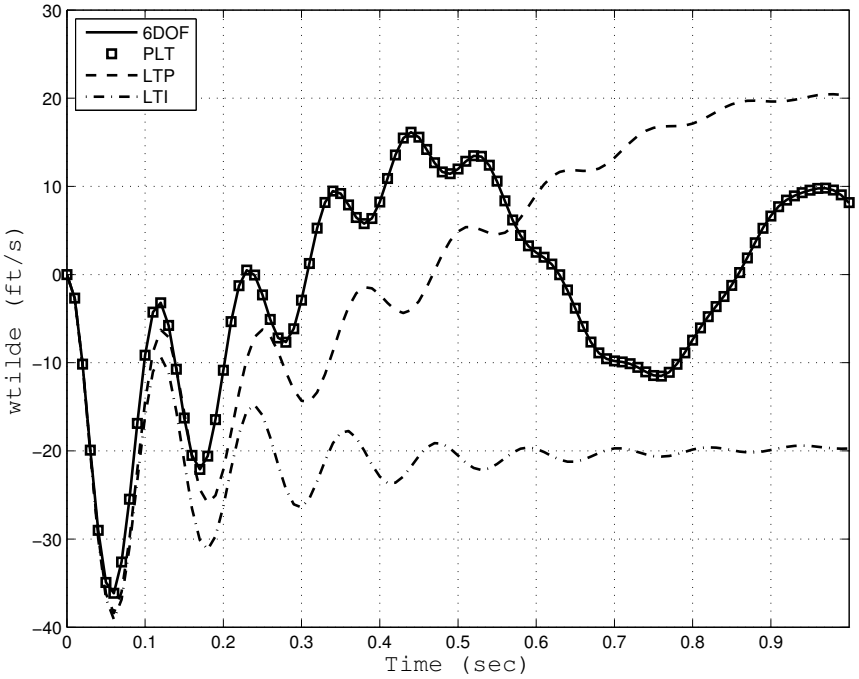

Figure 56: Validation Case 4 – Wtilde vs Time

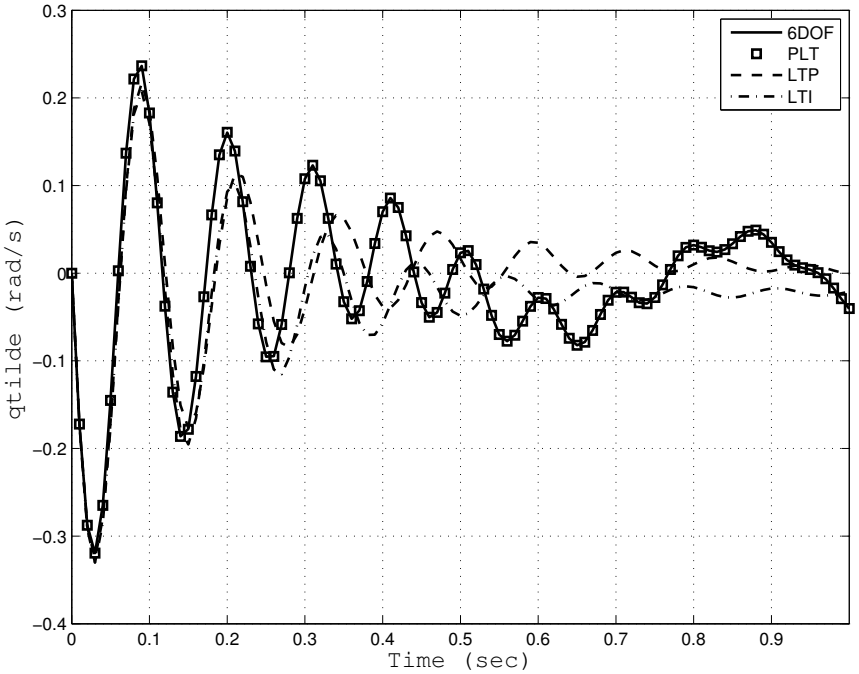

Figure 57: Validation Case 4 – Qtilde vs Time

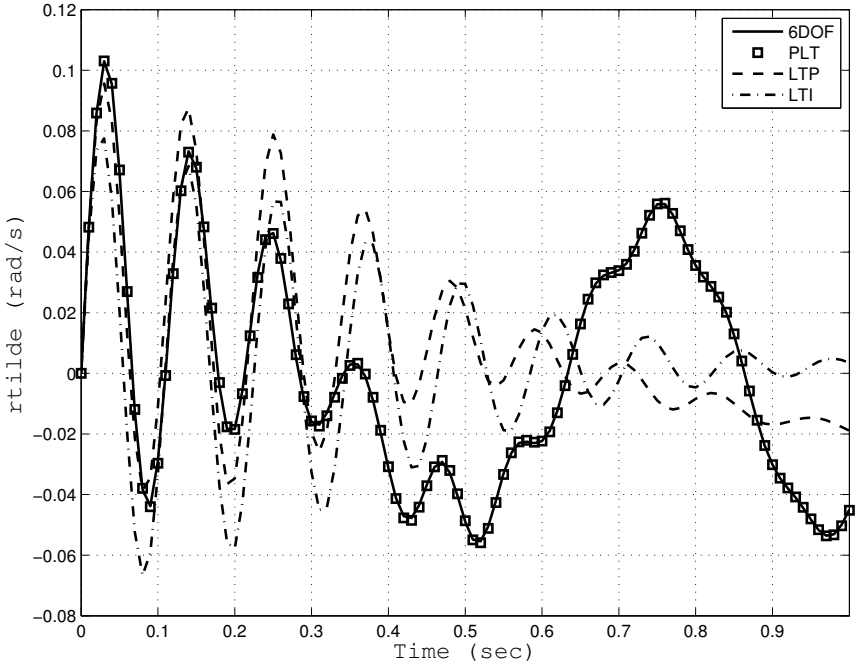

Figure 58: Validation Case 4 – Rtilde vs Time

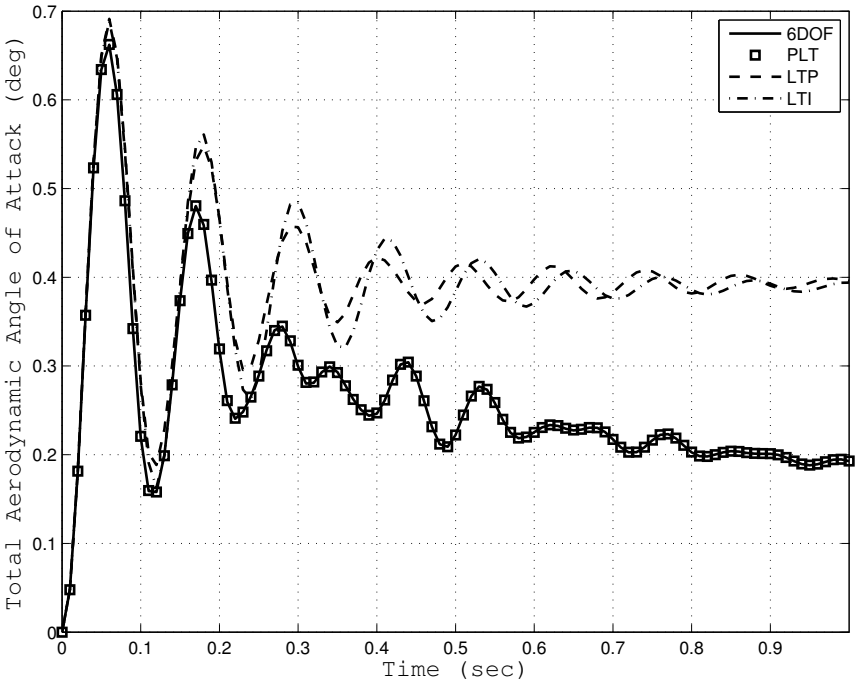

Figure 59: Validation Case 4 – Total Aerodynamic Angle of Attack vs Time

4.5 Case 5 – Stability Analysis of a Symmetric Projectile

In *Validation Case 3* the extended LTI model compared favorably to the 6DOF trajectory results for a symmetric projectile. In that case the LTP model was not simulated because for $p_o = 0.0$ (rad/sec) the LTP model is identical in form to the LTI model. This validation case further investigates the LTI and LTP models for a symmetric projectile by performing *eigenvalue* and *Floquet* stability analyses. Within the PLT matrix $\mathbf{A}$, the quasi-linear states V_o and ϕ_o were set to 558 (ft/sec) and 0.0 (rad/sec), respectively, while the roll rate was parametrically varied from 0.0 (rad/sec) $\leq p_o \leq$ 1000 (rad/sec).

Figure 60 shows root-locus plot of LTI and LTP stability results. As seen, both the LTI and LTP models generated nearly identical results. There are six system poles corresponding to the six dynamic states: V, p, $\tilde{v}$, $\tilde{w}$, $\tilde{q}$, and $\tilde{r}$. For symmetric projectiles, the poles that correspond to the latter four dynamic states are commonly referred to as the epicyclic poles. This behavior is confirmed upon inspection of the eigenvalue/mode structures. Table 4 shows the projectile mode structure at $p = 1000$ (rad/sec) and Mach 0.5. The behavior of these epicyclic poles for rolling symmetric projectiles is well understood [4][23] in that as roll rate increases two modes are observed: a fast mode λ_{FAST} and a slow mode λ_{SLOW}. As roll rate increases, the λ_{FAST} poles become increasingly stable, while the λ_{SLOW} poles become equally less stable. The results generated below confirm this behavior. At a roll rate of 0.0 (rad/sec), two epicyclic poles are equal (repeated roots), but as the roll rate increases, a fast mode pole and its complex conjugate more farther left, which indicates increasing stability. The two slow mode complex conjugates move further right in the left-half complex plane, indicating decreasing stability.

Showing that the LTP and LTI stability analyses for symmetric are equivalent is an important result. As the roll rate increases, the approximation of $\phi(t)$ as a linear function of time is a very accurate representation of the symmetric projectile roll

angle behavior.

Table 4: Orthonormalized eigenmatrix for $p = 1000$ (rad/sec) at $Ma = 0.5$.

	Velocity Mode	**Roll Mode**	**Fast Epicyclic Mode**		**Slow Epicyclic Mode**	
V	1.00	0.00	0.00	0.00	0.00	0.00
p	0.00	1.00	0.00	0.00	0.00	0.00
$\tilde{v}$	0.00	0.00	0.46	0.46	0.40	0.40
$\tilde{w}$	0.00	0.00	0.46	0.46	0.53	0.53
$\tilde{q}$	0.00	0.00	0.04	0.04	0.04	0.04
$\tilde{r}$	0.00	0.00	0.04	0.04	0.03	0.03

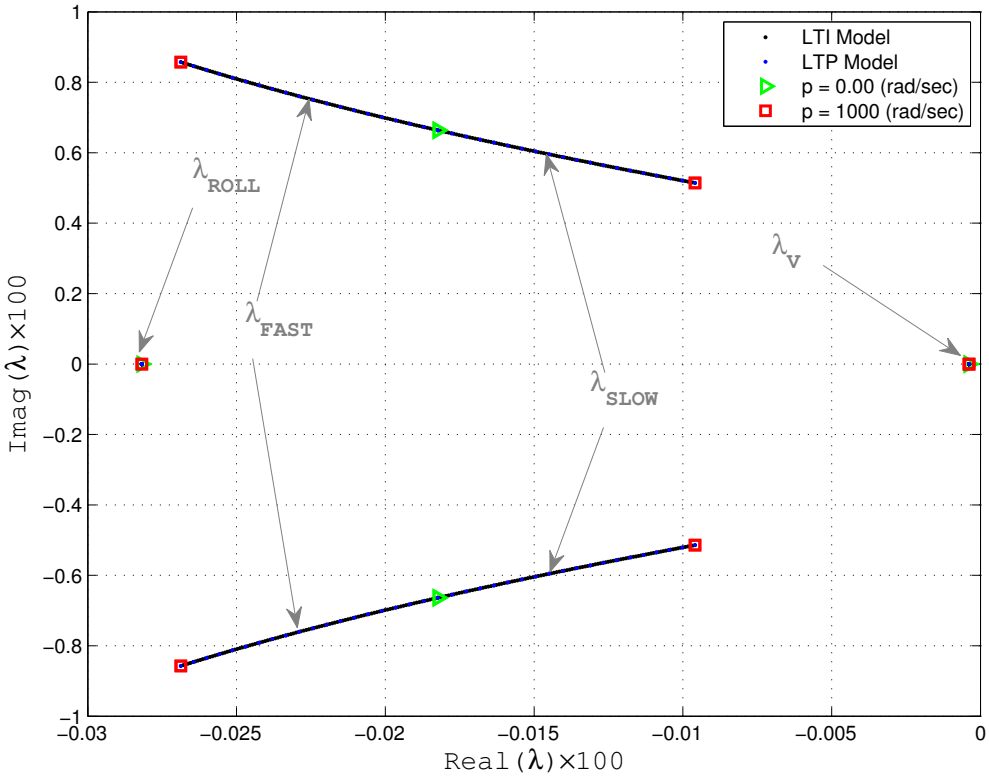

Figure 60: Root Locus: Parameterized by projectile spin rate p

4.6 Case 6 – Stability Analysis of a Asymmetric Projectile

This final validation case performs LTI and LTP stability analyses on the asymmetric projectile configuration, used previously (shown in Figure 6). Again, the quasi-linear states V_o and ϕ_o were set to 3357 (ft/sec) and 0.0 (rad/sec), respectively, and the roll rate was parametrically varied from 0.0 (rad/sec) $\leq p_o \leq$ 1000 (rad/sec).

Figure 60 shows root-locus plot of the generate LTI and LTP stability results for the asymmetric projectile and Table 5 shows the LTI model mode structure at $p = 1000$ (rad/sec). Notice from the slow mode structure that this mode is now mildly influenced by the roll rate. As in the case of the symmetric projectile, a fast mode is observed to move towards stability in a complex conjugate pair, while a slow mode follows similar behavior but becomes less stable. For this projectile the LTI and LTP models are not equivalent, as was the case for the symmetric projectile; however, the epicyclic poles for the LTI and LTP models do approach each other as roll rate increases.

Upon additional inspection of mode structures, a roll mode λ_{ROLL} is found to correspond to a pole that is further stable and located on the real axis, while a total velocity mode λ_V is found to correspond to a pole that is also located on the real axis. In projectile stability studies, this velocity mode is primarily driven by the base drag coefficient C_{X0} and is always real and very lightly damped. Typically, projectile performance in stability analyses is determined, where the total velocity mode is ignored[4][23].

Table 5: Orthonormalized eigenmatrix for $p = 1000$ (rad/sec) at $Ma = 0.5$.

	Velocity Mode	**Roll Mode**	**Fast Epicyclic Mode**		**Slow Epicyclic Mode**	
V	0.98	0.00	0.00	0.00	0.00	0.00
p	0.02	1.00	0.08	0.08	0.13	0.13
$\tilde{v}$	0.00	0.00	0.42	0.42	0.42	0.42
$\tilde{w}$	0.00	0.00	0.43	0.43	0.41	0.41
$\tilde{q}$	0.00	0.00	0.04	0.04	0.02	0.02
$\tilde{r}$	0.00	0.00	0.04	0.04	0.02	0.02

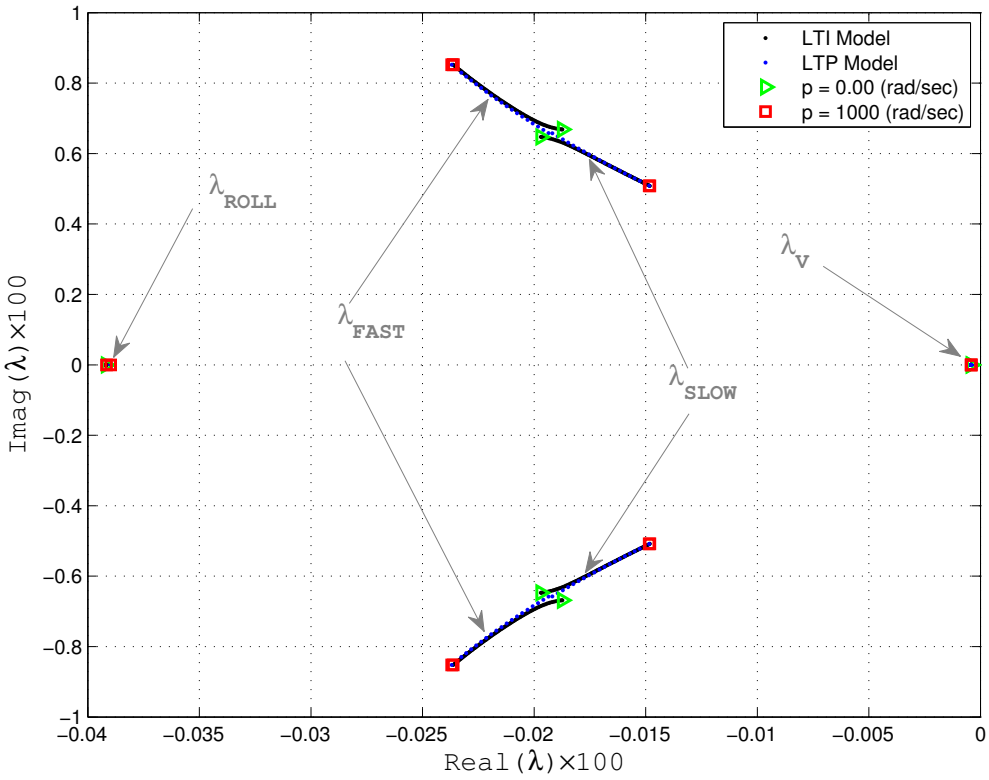

Figure 61: Root Locus: Parameterized by projectile spin rate p

CHAPTER V

TRADE STUDIES

It has been shown that extended PLT models are capable of approximating the dynamics of projectiles with general lifting surface configurations; however, accurate approximation of extended LTI and LTP models to the 6DOF model is not always guaranteed. This point was demonstrated in the case of the asymmetric projectile of *Chapter 4*, where an asymmetric lifting surface configuration was arbitrarily chosen without any intuition into the flight mechanics. This was an extreme case of an aerodynamically asymmetric projectile, since the lifting surface configuration was asymmetric in both horizontal ($\vec{I}_B - \vec{J}_B$) and vertical ($\vec{I}_B - \vec{K}_B$) planes of the projectile body frame. Often, airframes are only asymmetric in one plane, as is the case with winged aircraft. Both types of aerodynamic asymmetries will be studied in this chapter, but it will be shown that the second type of aerodynamic asymmetry can be very well approximated by the extended PLT models.

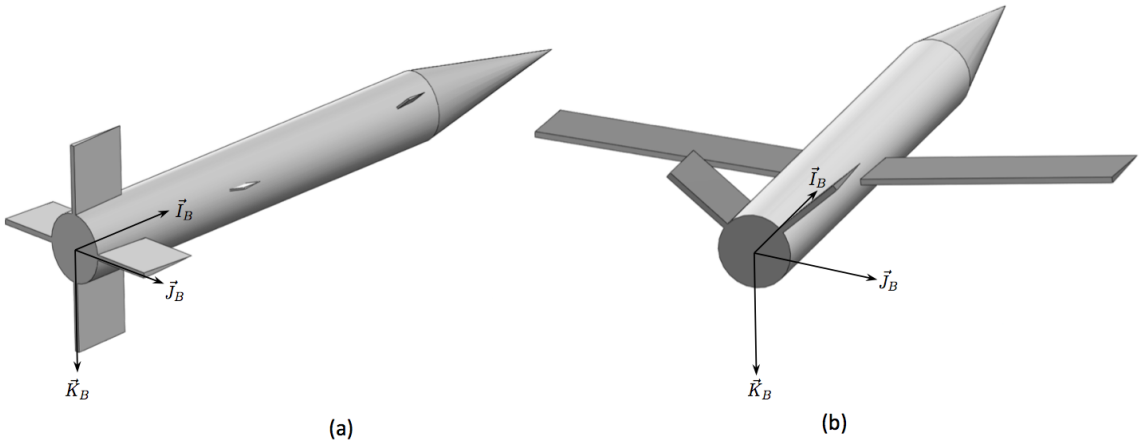

Figure 62: Example illustrations of (a) a projectile configuration that is fully asymmetric and (b) a projectile configuration that is only asymmetric with respect to one plane (horizontal plane).

In this chapter, parametric trade studies of various projectile configurations are conducted, using the extended LTI and LTP stability models. As was done in the last chapter, comparison was made between 6DOF, LTI, and LTP model trajectory results. Dynamic simulation results will be briefly discussed in a case-by-case basis; however, dynamic simulation results will only be shown if necessary. In this chapter there are two distinct types of parametric stability analyses that are performed: (1) geometrical variation (*i.e.* variation of fin length) and (2) quasi-linear dynamic state variation (*i.e.* variation of roll rate). The latter analysis type will be used on certain special projectile configurations to gain additional insight on dynamic stability. An outline of the trade studies presented in this chapter include the following:

- **Baseline 4-Finned Symmetric Projectile Configuration:**

  (1) Asymmetric variation of fin parameters.

  (2) Roll angle variation of interesting configurations.

- **Baseline 3-Finned Symmetric Projectile Configuration:**

  (1) Asymmetric variation of fin parameters.

  (2) Roll angle variation of interesting configurations.

- **Baseline Hybrid/Projectile Configuration:**

  (1) Mach number variation of the baseline configuration.

  (2) Asymmetric variation of tail and wing parameters.

5.1 Trade Study – Vary Fin Parameters Off The Baseline 4-Finned Projectile Configuration

The purpose of the following set of trade studies is to investigate the effects of varying fin length (or equivalently fin area) with respect to a baseline 4-finned projectile. In Figure 63 a projectile body is shown with four labeled fins, symmetrically placed at the rear of the projectile. Table 6 summarizes nominal fin geometry, where the i^{th} fin length, width, azimuth angle, and cant angle are represented by b_i, c_i, ϕ_{C_i}, and δ_{C_i}, respectively.

Table 6: Summary Baseline 4-Finned Projectile Parameters

Fin#	b_i (ft)	c_i (ft)	ϕ_{C_i} (deg)	δ_{C_i} (deg)
F1	0.0984	0.0984	0.0	0.00
F2	0.0984	0.0984	90	0.00
F3	0.0984	0.0984	180	0.00
F4	0.0984	0.0984	270	0.00

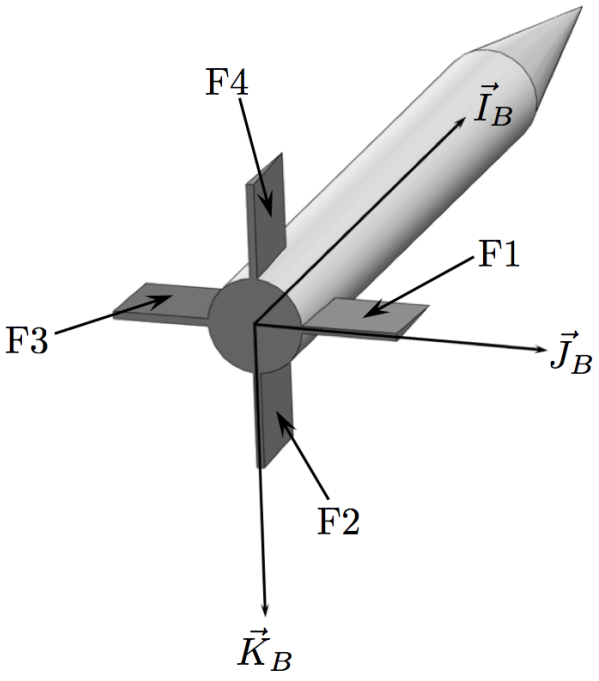

Figure 63: Illustration of the baseline 4-finned projectile configuration.

5.1.1 Effect of Variation of Fin F1 and F3 fin Lengths on Stability

In the following trade study, projectile dynamic stability was evaluated for simultaneous variation of F1 and F3 fin lengths (or equivalently fin areas). Given the nominal fin lengths previously summarized in Table 6, stability roots were calculated as F1 and F3 lengths varied between $0 \leq b \leq 4b_{nom}$. Projectile quasi-linear roll rate and roll angle were set to 0.0 (rad/sec) and 0.0 (deg), respectively. Both subsonic and supersonic cases were considered, where the quasi-linear total velocity was set to 558.0 (ft/sec) (Mach 0.5) in the subsonic case and 3357.0 (ft/sec) (Mach 3.0) in the supersonic case. Dynamic simulation for this study showed that the LTI model was sufficient to approximate the 6DOF model for at least 1.0 (sec) of flight time for values of b where the system was stable. The system was observed to grow increasingly unstable as the fin length approached 0.0 (ft), causing discrepancy between LTI and 6DOF models as larger angles of attack were observed.

Figure 64 shows the subsonic behavior of the dynamic modes with changing F1 and F3 fin lengths, and Table 7 shows the LTI mode structure at $b/b_{nom} = 0.0$. As fin length decreases from $b/b_{nom} = 4.0$, the two vertical plane epicyclic roots significantly decrease in frequency towards zero at point A. At the value $b/b_{nom} \approx 0.34$, the behavior of these roots changes as they split into a pair of real roots in branches AB and AC of the locus. These branches represent damped aperiodic modes, or subsidences. At $b/b_{nom} \approx 0.3404$, branch AC crosses over the imaginary axis, making the system unstable. The two horizontal plane epicyclic roots are invariant in b. These modes are related to the fins F2 and F4, which are not varied, hence leaving the horizontal plane stability unaffected. Finally, the real-valued roll mode root becomes very lightly damped as b approaches zero. In Figure 65, the dynamic modes of the supersonic case are shown to behave similarly to the subsonic case, but that the system becomes unstable more quickly at values less than $b/b_{nom} \approx 0.528$.

Table 7: Orthonormalized eigenmatrix for $b/b_{nom} = 0.0$ at $Ma = 0.5$.

	Velocity Mode	Roll Mode	Vertical Epicyclic Mode		Horizontal Epicyclic Mode	
V	1.00	0.00	0.00	0.00	0.00	0.00
p	0.00	1.00	0.00	0.00	0.00	0.00
$\tilde{v}$	0.00	0.00	0.00	0.00	0.99	0.99
$\tilde{w}$	0.00	0.00	0.99	0.99	0.00	0.00
$\tilde{q}$	0.00	0.00	0.01	0.01	0.00	0.00
$\tilde{r}$	0.00	0.00	0.00	0.00	0.01	0.01

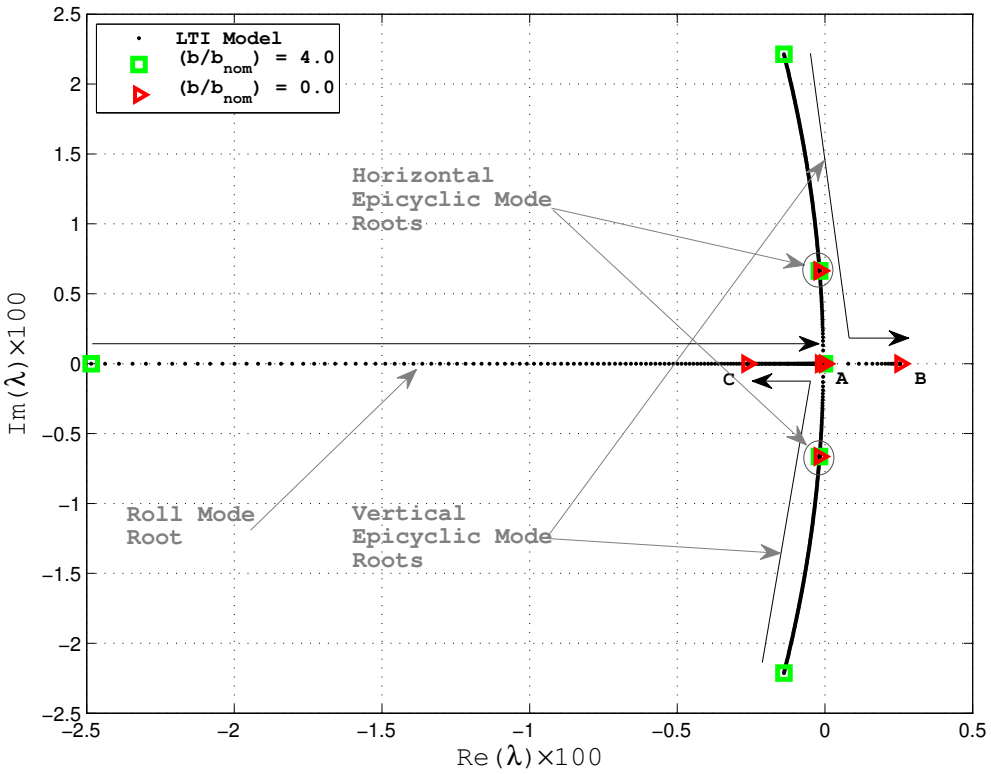

Figure 64: Root Locus: Parameterized by equal variation in F1 and F3 lengths. Subsonic Case: Mach 0.5.

Table 8: Orthonormalized eigenmatrix for $b/b_{nom} = 0.0$ at $Ma = 3.0$.

	Velocity Mode	Roll Mode	Vertical Epicyclic Mode		Horizontal Epicyclic Mode	
V	1.00	0.00	0.00	0.00	0.00	0.00
p	0.00	1.00	0.00	0.00	0.00	0.00
$\tilde{v}$	0.00	0.00	0.00	0.00	0.97	0.97
$\tilde{w}$	0.00	0.00	0.97	0.97	0.00	0.00
$\tilde{q}$	0.00	0.00	0.03	0.03	0.00	0.00
$\tilde{r}$	0.00	0.00	0.00	0.00	0.03	0.03

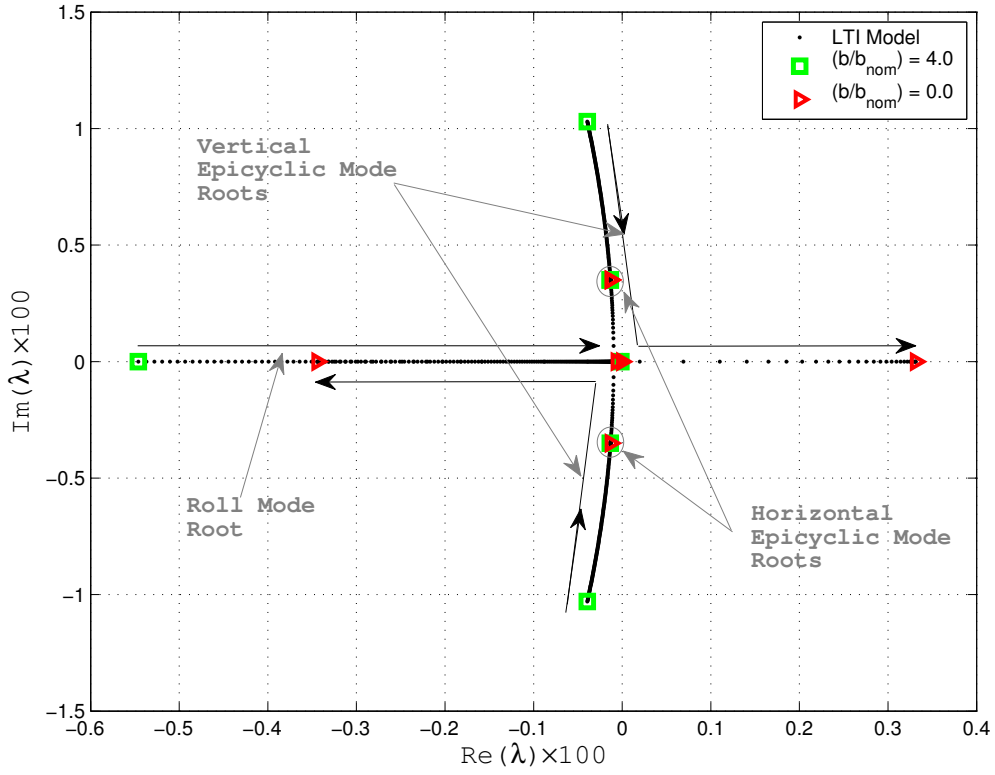

Figure 65: Root Locus: Parameterized by equal variation in F1 and F3 lengths. Supersonic Case: Mach 3.0.

5.1.2 Effect of Roll Rate on Symmetric 2-Finned Projectile Stability

In *Chapter 4* a stability analysis was performed on an axis-symmetric 4-finned projectile as roll rate was varied from 0.0 (rad/sec) $\leq p_o \leq$ 1000 (rad/sec). That study concluded that as roll rate was increased, the epicyclic modes split into fast and slow modes. Here the same analysis is performed but on the unstable symmetric 2-finned projectile, shown in Figure 66. The goal is to determine if vertical plane instabilities can be "rolled out" with increasing roll rate, which is commonly done to stabilize finless projectiles. Note, the usage of the word "symmetry" here does not imply axis-symmetry as is the case with the 4-finned projectile, because the aerodynamic models (coefficients) in each plane are not equivalent.

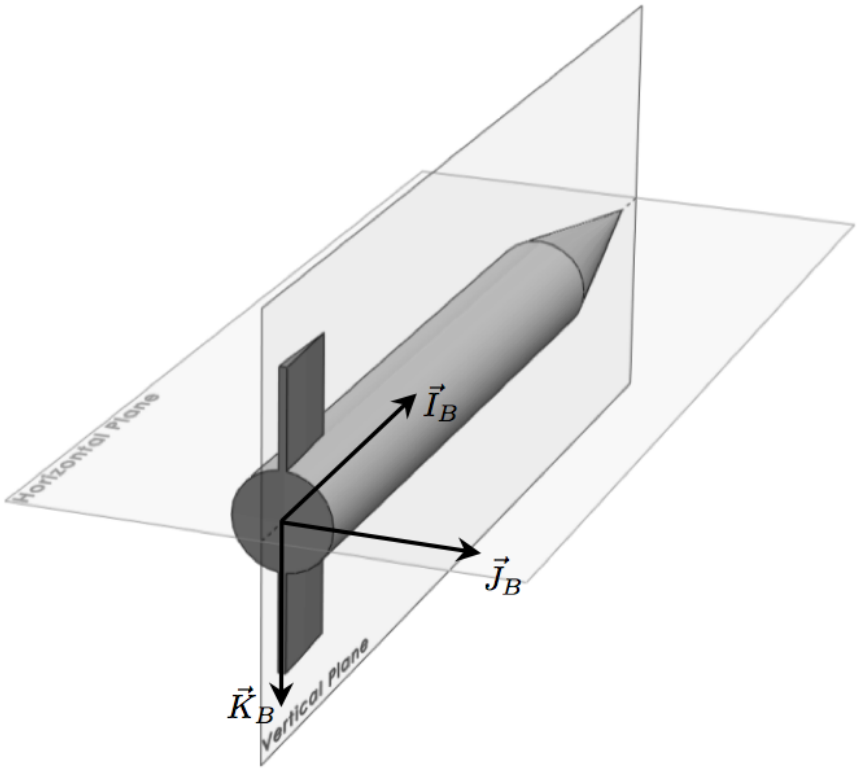

Figure 66: Illustration of a symmetric 2-finned projectile that is unstable in the vertical plane, due to the missing horizontal fins.

Prior to evaluating stability, dynamic simulations were run to compare LTI, LTP, and 6DOF models for the 2-finned projectile. The fin geometry summarized in Table 6 was used for to describe the two fins. Several initial rolls rates were simulated for the projectile launched subsonically at Mach 0.5 and a quadrant elevation of 1.0286 (deg). In these results the LTI and LTP models showed significant deviation from the 6DOF results after 0.1 seconds of flight. This is because while small angles of attack were observed, the roll rate decreased rapidly over a short period of time, thus causing error in the approximation of roll rate as quasi-linear. Also, in every simulation the roll rate slowed enough at some point in time to cause unstable flight characteristics. Thus, dynamic stability continuously changes through flight for changing p_o.

Often in finned projectiles, fin cant is used to induce a steady state roll rate and increase ballistic accuracy. Setting a cant angle for the two fins, a second set of simulations were run. The fin cant was expressed as a function of initial roll rate to encourage a near constant roll rate through flight. At Mach 0.5 the fin cant was found to vary linearly with the roll rate by the relation δ_{c_i} (deg) $\approx 0.0047 p_o$. In these second set of simulations, the LTP model was successfully able to approximate 6DOF results for 1.0 seconds of flight, while the LTI model was still significantly inaccurate. Figures 67 - 79 show trajectory results for a projectile fired at Mach 0.5 with $p_o = 1000$ (rad/sec) and $\delta_{C_i} = 4.7$ (deg). These figures demonstrate the ability of the LTP model to approximate the 6DOF model when fin cant is used to encourage near constant roll rate through flight.

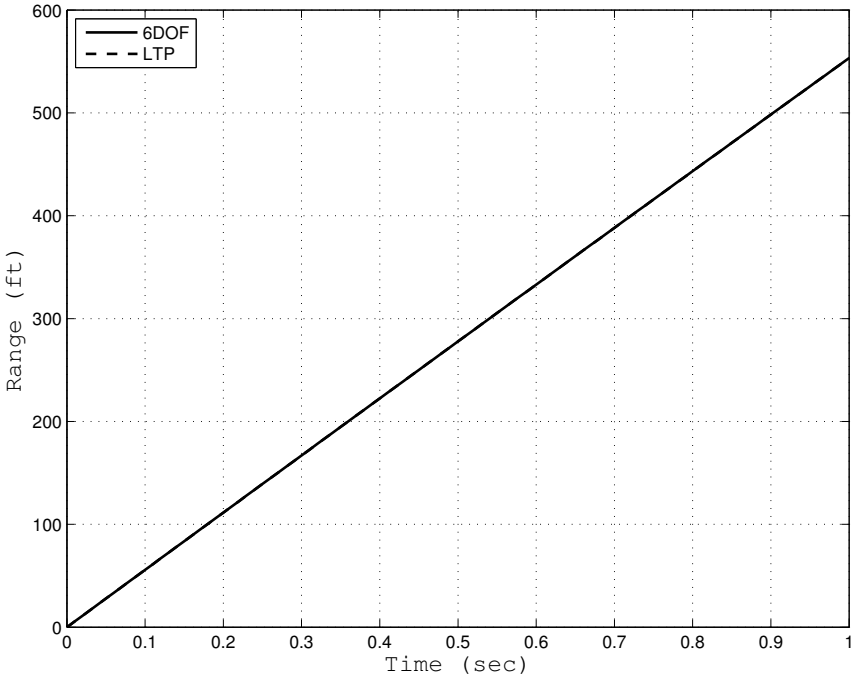

Figure 67: 2-Finned Projectile Case – Range vs Time

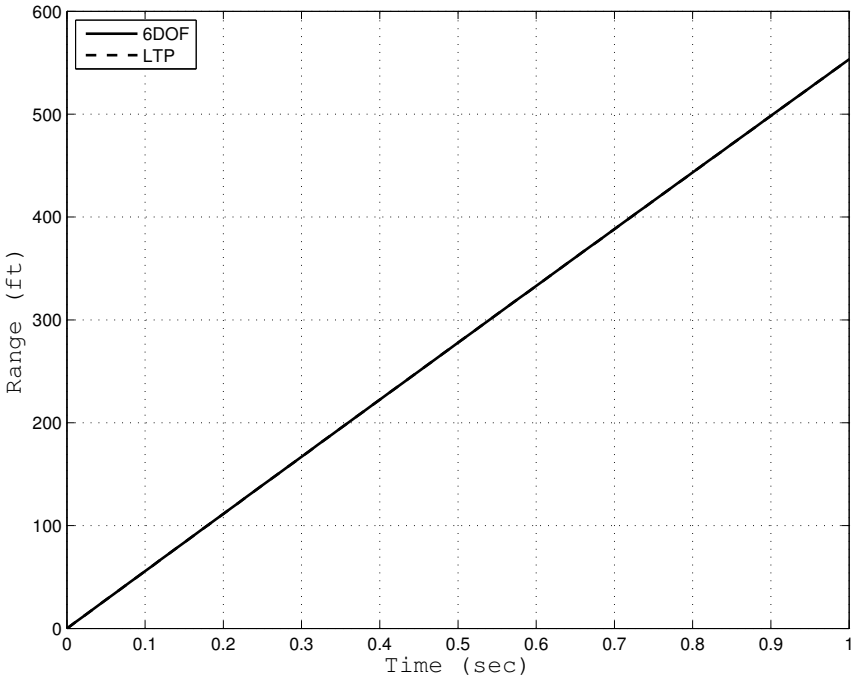

Figure 68: 2-Finned Projectile Case – Cross Range vs Time

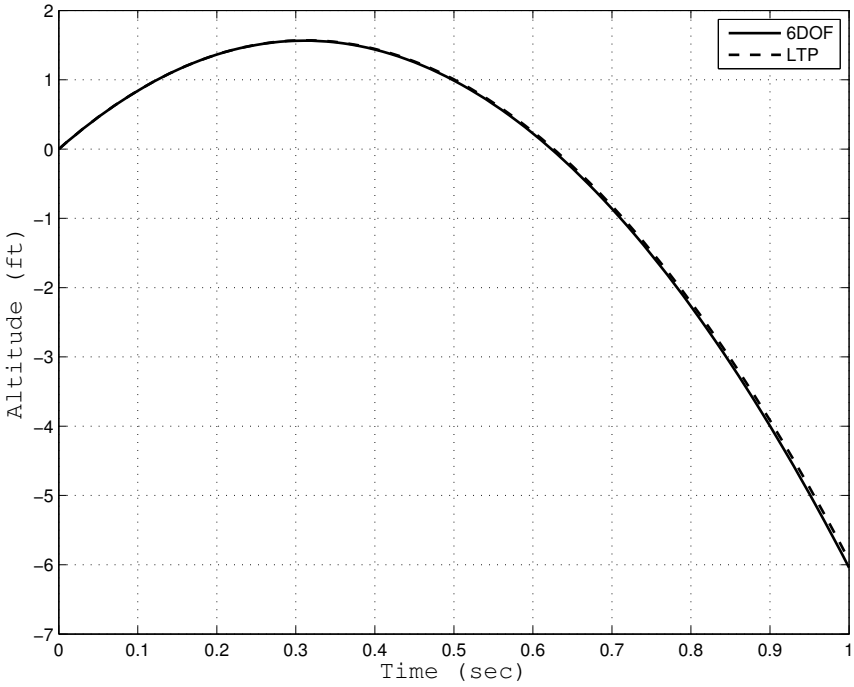

Figure 69: 2-Finned Projectile Case – Altitude vs Time

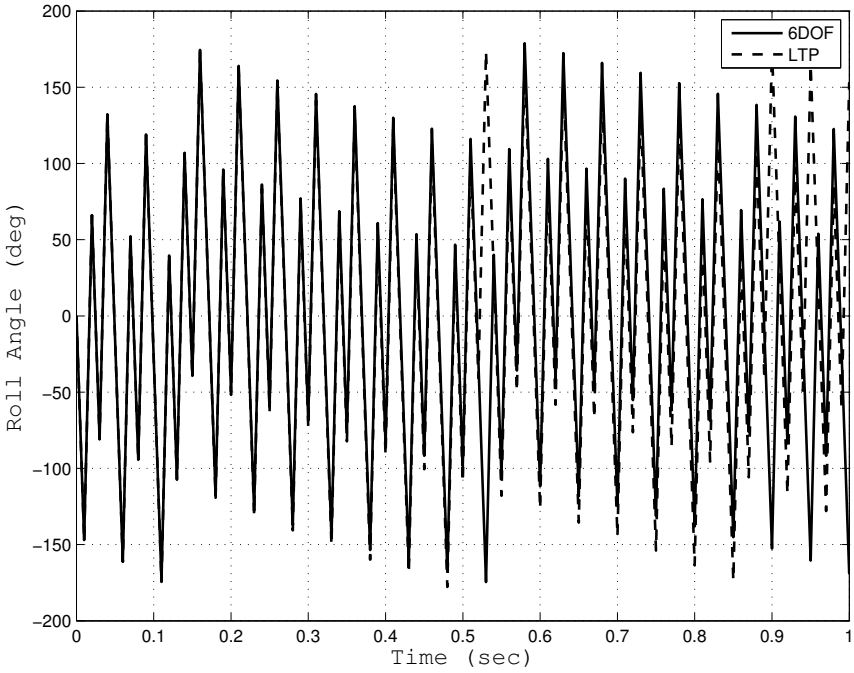

Figure 70: 2-Finned Projectile Case – Roll Angle vs Time

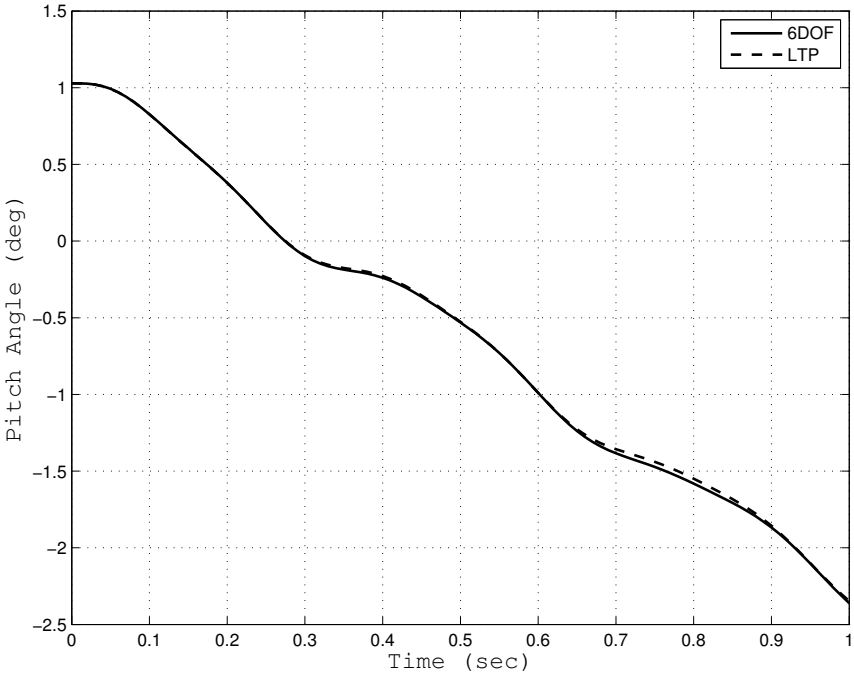

Figure 71: 2-Finned Projectile Case – Pitch Angle vs Time

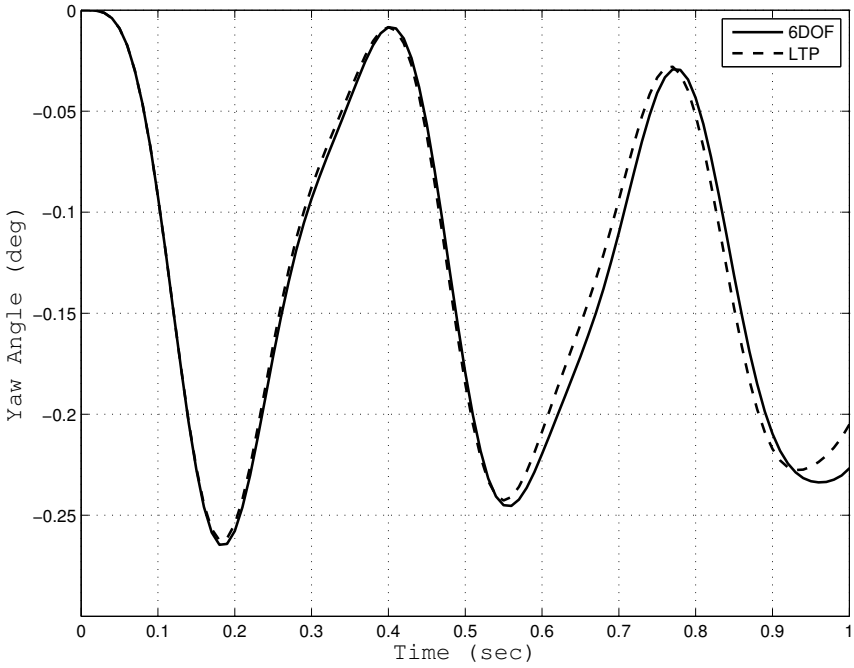

Figure 72: 2-Finned Projectile Case – Yaw Angle vs Time

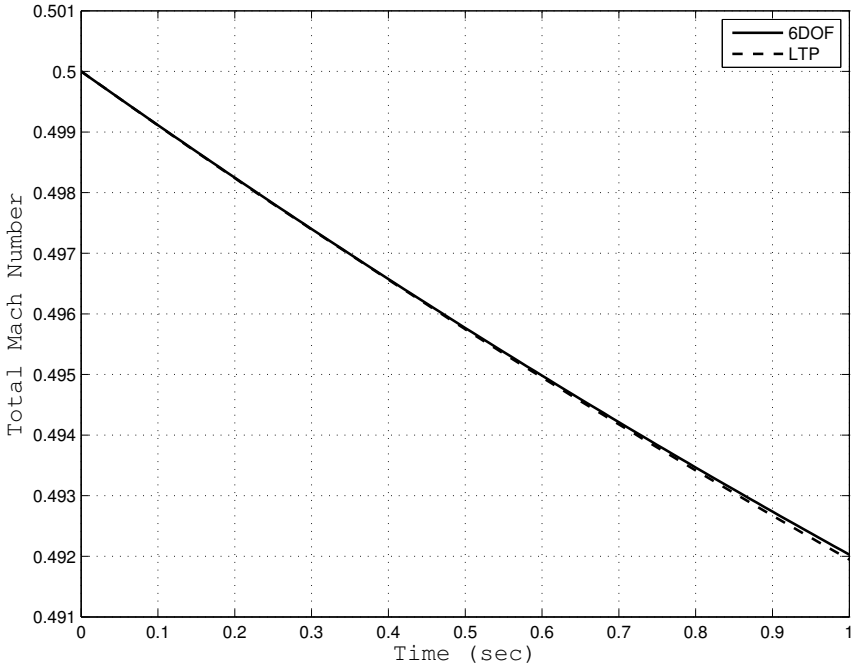

Figure 73: 2-Finned Projectile Case – Total Mach Number vs Time

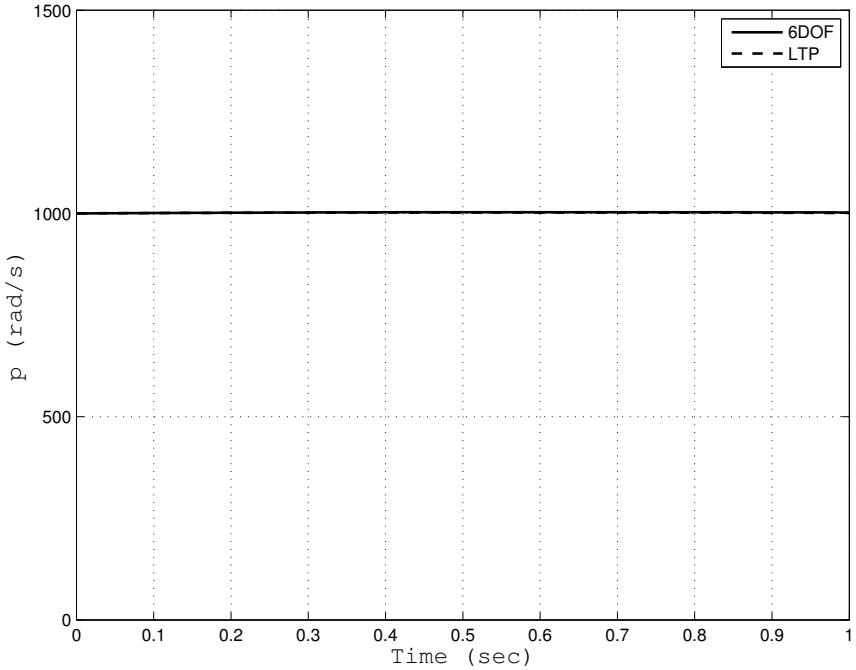

Figure 74: 2-Finned Projectile Case – Roll Rate vs Time

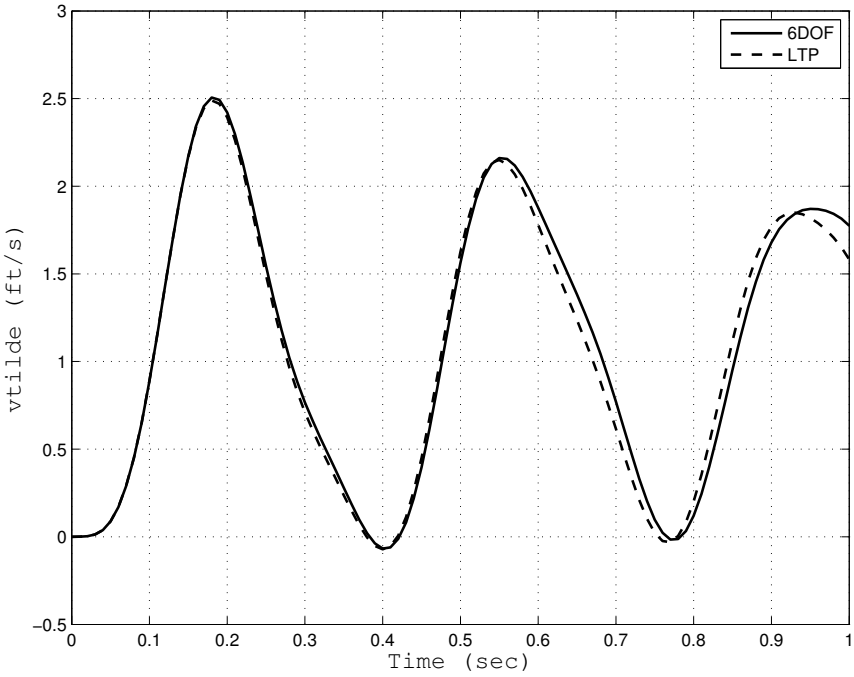

Figure 75: 2-Finned Projectile Case – Vtilde vs Time

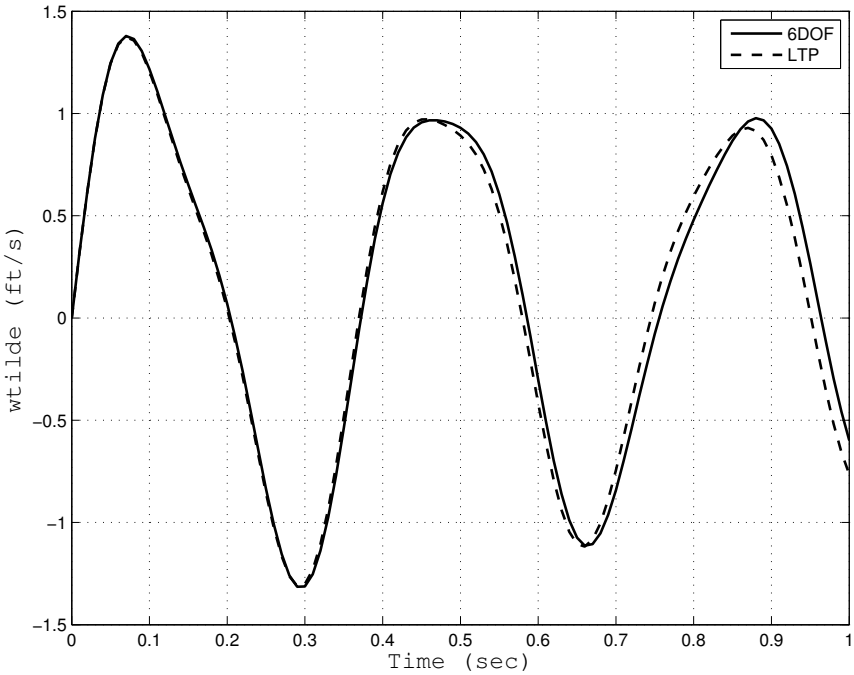

Figure 76: 2-Finned Projectile Case – Wtilde vs Time

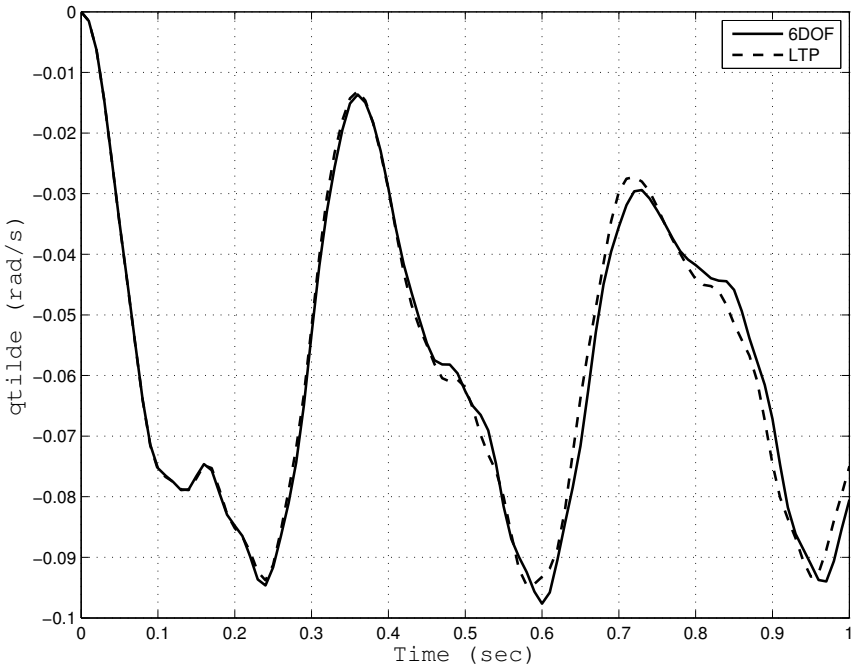

Figure 77: 2-Finned Projectile Case – Qtilde vs Time

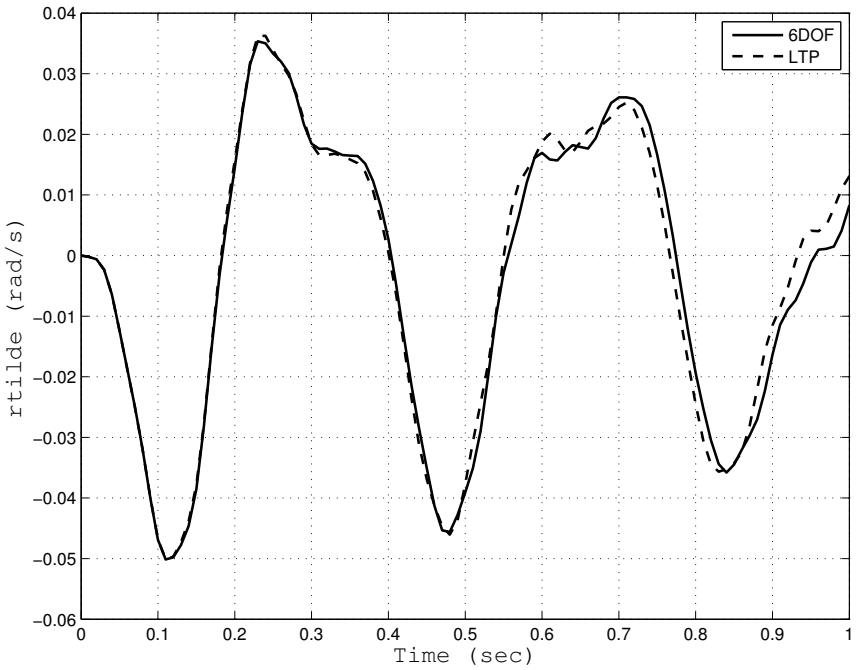

Figure 78: 2-Finned Projectile Case – Rtilde vs Time

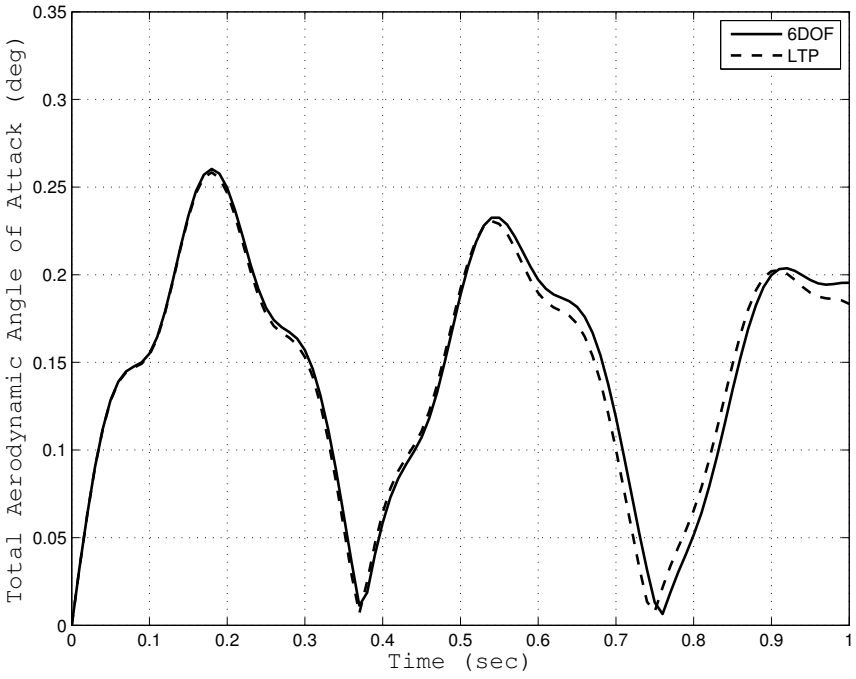

Figure 79: 2-Finned Projectile Case – Total Aerodynamic Angle of Attack vs Time

Since the LTP model significantly outperformed the LTI model in dynamic simulation, Floquet theory was used to evaluate stability. Figure 80 summarizes stability results for the canted 2-finned projectile as roll rate was varied from 0.0 (rad/sec) $\leq$ $p_o \leq$ 1000 (rad/sec). Interestingly enough as roll rate increases, the epicyclic roots are observed to split into fast and slow modes when $p_o \approx 1.34$ (rad/sec). (*Recall that fast/slow mode epicyclic behavior was also observed in case of the axis-symmetric 4-finned projectile stability analysis of* Section 4.5.) Figure 81 shows a closer look at the root locus for $p_o < 1.34$ (rad/sec). For small and decreasing p_o, all four epicyclic roots converge in pairs towards the real axis, where two roots split and diverge to instability. Also in Figure 81, the roll mode root is labeled and is shown be small, real, and unchanging as roll rate is varied.

It is worth mentioning that a stability analysis was also performed for the 2-finned projectile with zero fin cant. Nearly identical results to the canted projectile case were observed with the exception being in the roll mode roots. The roll mode roots were

less stable for this case but not unstable. This deviation, however, was so small that if these the results were plotted over the results of Figure 80 for the entire root locus the difference would not be visually noticeable.

The results of this study are significant in that the statically unstable (zero roll stability) of the 2-finned projectile configuration can be dynamically "rolled out", and then the familiar fast/slow epicyclic mode behavior is observed. Therefore by introducing fin cant and roll rate, the projectile can be said to be dynamically stabilized.

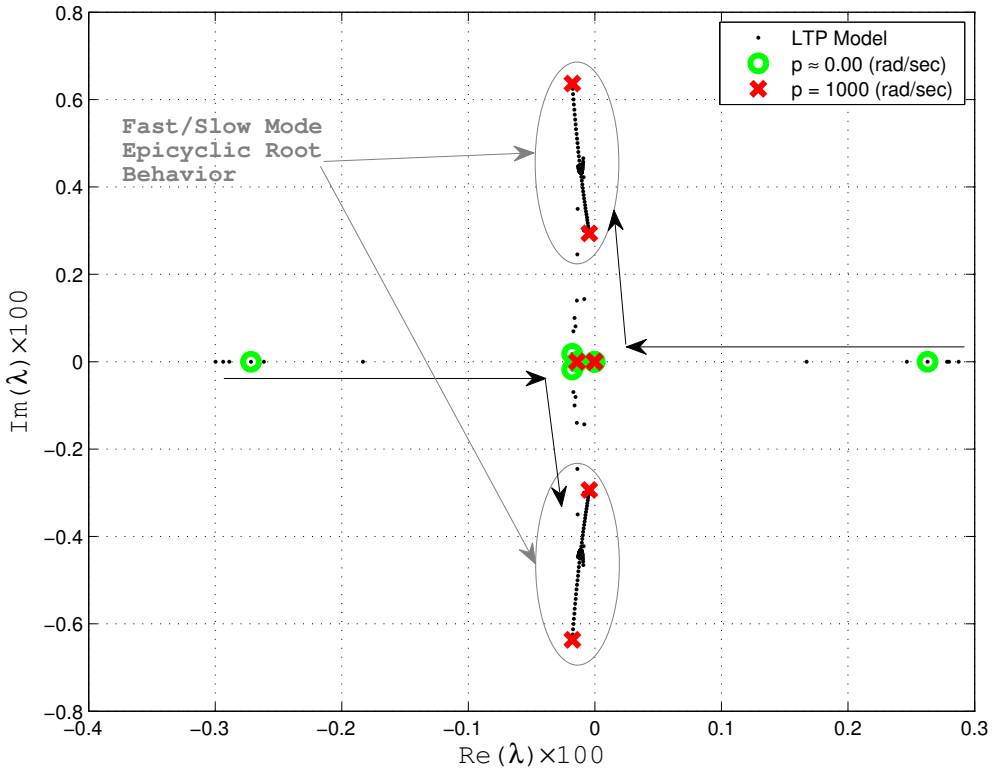

Figure 80: Root Locus: Parameterized by projectile spin rate p at Mach 0.5.

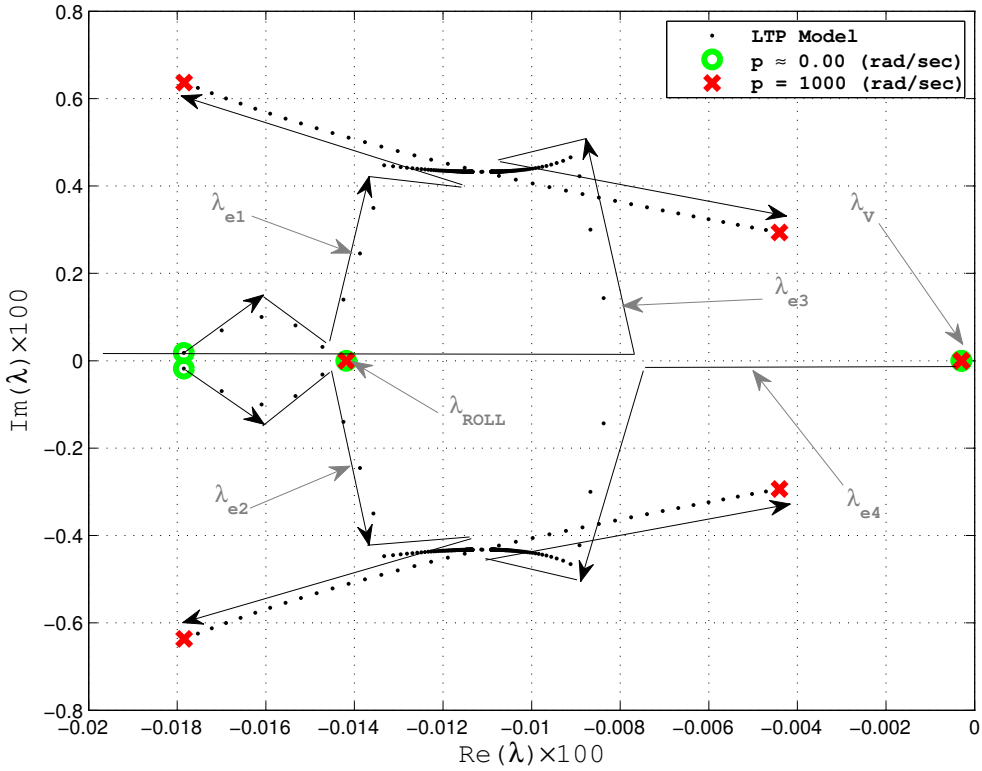

Figure 81: Close-up view of epicyclic root behavior as roll rate is increased.

5.1.3 Effect of Variation of F2 Fin Length on Stability

In the following trade study, projectile dynamic stability was evaluated for variation of F2 fin length (or equivalently fin area). Given the nominal fin lengths previously summarized in Table 4, stability roots were calculated as F2 fin length varied between $0 \leq b \leq 4b_{nom}$. Projectile quasi-linear roll rate and roll angle were set to 0.0 (rad/sec) and 0.0 (deg), respectively. Both subsonic and supersonic cases were considered, where the quasi-linear total velocity was set to 558.0 (ft/sec) (Mach 0.5) in the subsonic case and 3357.0 (ft/sec) (Mach 3.0) in the supersonic case. Dynamic simulation for this study showed that the LTI model was sufficient to approximate the 6DOF model for at least 1.0 (sec) of flight time for values of b where the system was stable. In the supersonic case, the system was observed to grow increasingly

unstable in the roll mode as the fin length approached 0.0 (ft), causing discrepancy between LTI and 6DOF models in roll angle and roll rate.

Figure 82 shows the subsonic behavior of the dynamic modes with changing b, and Table 9 shows the LTI mode structure at $b/b_{nom} = 0.0$. Observation of the eigenvalue/mode structures throughout this analysis showed that as the configuration became increasingly asymmetric, cross-coupling of roll rate and horizontal epicyclic states were observed in horizontal epicyclic and roll/yaw mode structures. When $b/b_{nom} = 4.0$, the two horizontal epicyclic roots are highly oscillatory and heavily damped. As the fin length is varied until $b/b_{nom} = 1.0$, the the dynamic roots are observed to approach values of the vertical epicyclic roots. Reducing the fin length down to $b/b_{nom} = 0.0$, causes the dynamic roots to diminish in frequency while the real component remains approximately constant. Also, the roll/yaw mode becomes significantly less stable; as b/b_{nom} diminishes from 4.0 to 0.0; however, the two vertical epicyclic roots remain unaffected by variation of b.

Figure 83 shows the root locus for the supersonic case of parametric variation of b. For values of fin length $b/b_{nom} > 1.0$, the root locus trends are similar to the subsonic case. As the fin length is reduced below b_{nom}, the dynamic epicyclic roots are observed to increase in stability, while still diminishing in frequency. The roll/yaw mode root, however, does not remain stable for decreasing b. At approximately, $b/b_{nom} \approx 0.34$, this root crosses over the imaginary axis drives the system unstable. The effect of the unstable roll/yaw mode causes the system to drift away from a near steady condition at an exponential rate. In dynamic simulation roll/yaw mode was observed, as coupling between the roll rate and epicyclic states lead to unstable flight characteristics with increasingly larger angles of attack.

Table 9: Orthonormalized eigenmatrix for $b/b_{nom} = 0.0$ at $Ma = 0.5$.

	Velocity Mode	**Roll/Yaw Mode**	**Vertical Epicyclic Mode**		**Horizontal Epicyclic Mode**	
V	1.00	0.00	0.00	0.00	0.00	0.00
p	0.00	0.94	0.00	0.00	0.26	0.26
$\tilde{v}$	0.00	0.06	0.00	0.00	0.71	0.71
$\tilde{w}$	0.00	0.00	0.94	0.94	0.00	0.00
$\tilde{q}$	0.00	0.00	0.06	0.06	0.00	0.00
$\tilde{r}$	0.00	0.00	0.00	0.00	0.03	0.03

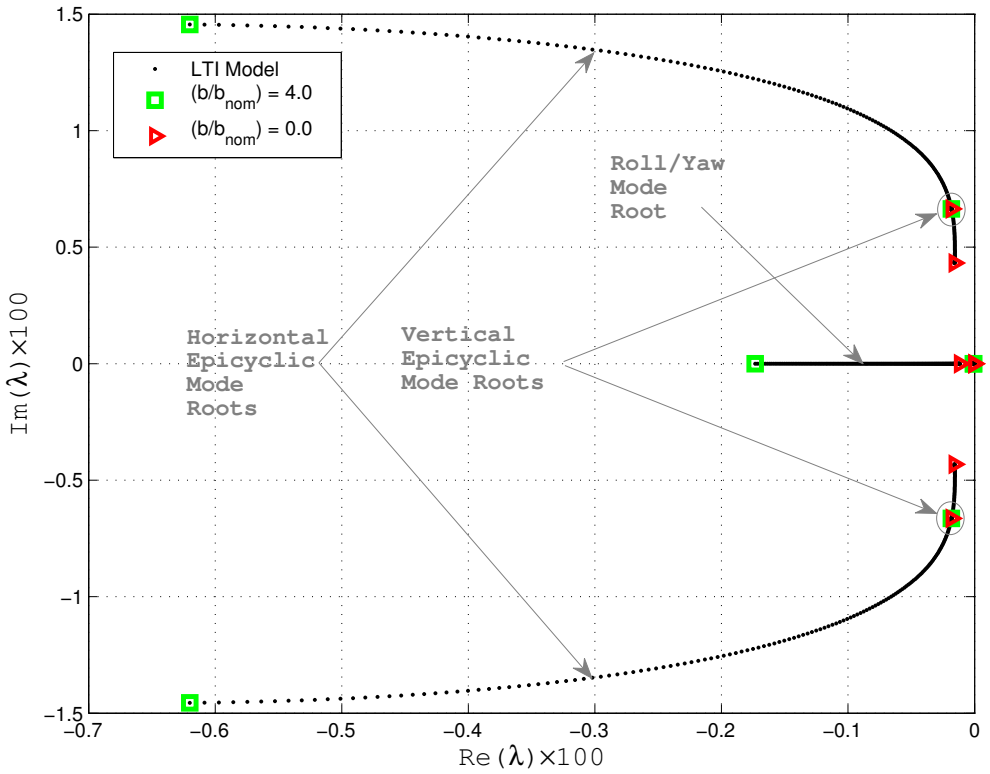

Figure 82: Root Locus: Parameterized by equal variation in F2 fin length. Subsonic Case: Mach 0.5.

Table 10: Orthonormalized eigenmatrix for $b/b_{nom} = 0.0$ at $Ma = 3.0$.

	Velocity Mode	Roll/Yaw Mode	Vertical Epicyclic Mode		Horizontal Epicyclic Mode	
V	1.00	0.00	0.00	0.00	0.00	0.00
p	0.00	0.57	0.00	0.00	0.45	0.45
$\tilde{v}$	0.00	0.43	0.00	0.00	0.54	0.54
$\tilde{w}$	0.00	0.00	0.97	0.97	0.00	0.00
$\tilde{q}$	0.00	0.00	0.03	0.03	0.00	0.00
$\tilde{r}$	0.00	0.00	0.00	0.00	0.01	0.01

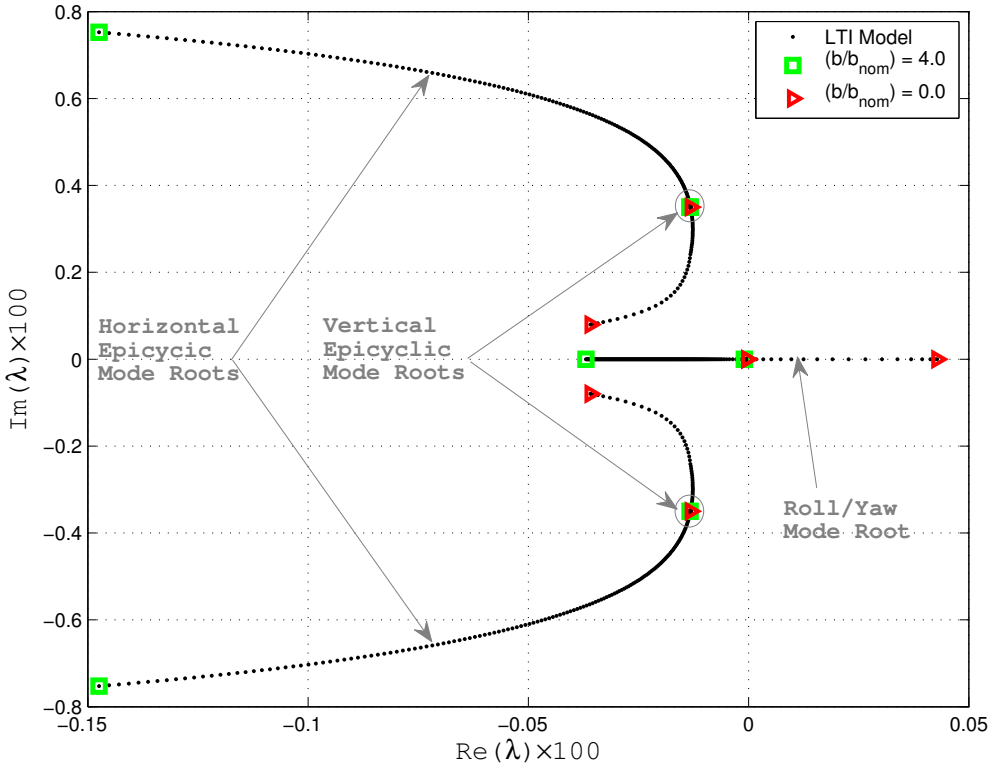

Figure 83: Root Locus: Parameterized by equal variation in F2 fin length. Supersonic Case: Mach 3.0.

5.1.4 Effect of Variation of F1 and F2 Fin Lengths on Stability

In the following trade study, projectile dynamic stability was evaluated for simultaneous variation of F1 and F2 fin lengths (or equivalently fin areas). Given the nominal fin lengths previously summarized in Table 6, stability roots were calculated as F1 and F2 lengths varied between $0 \leq b \leq 4b_{nom}$. Projectile quasi-linear roll rate and roll angle were set to 0.0 (rad/sec) and 0.0 (deg), respectively. Both subsonic and supersonic cases were considered, where the quasi-linear total velocity was set to 558.0 (ft/sec) (Mach 0.5) in the subsonic case and 3357.0 (ft/sec) (Mach 3.0) in the supersonic case. Dynamic simulation for this study showed that the LTI model was sufficient to approximate the 6DOF model for at least 1.0 (sec) of flight time for values of b where the system was stable. For unstable configurations, large aerodynamic angles of attack were observed.

Figure 84 shows the subsonic behavior of the dynamic modes with changing F1 and F2 fin lengths, and Table 11 shows the LTI mode structure at $b/b_{nom} = 0.0$. First, both epicyclic modes are observed to vary with changing b. This occurs because F1 and F2 are not positioned about a plane of symmetry, and therefore both horizontal and vertical plane stability are affected. As b becomes large, the horizontal epicyclic roots grow increasingly damped with smaller changes in frequency. The two vertical epicyclic roots behave in relatively the opposite manner, becoming increasingly more oscillatory and subtly become more damped. At values of b close to b_{nom} the two epicyclic modes converge upon each other. Very little change is observed in epicyclic stability for values of $b/b_{nom} < 1.0$. The roll/yaw mode shows a significant reduction in stability as b is reduced from $4b_{nom}$ towards zero, eventually becoming unstable just before reaching $b/b_{nom} = 0.0$.

In Figure 85, the dynamic modes of the supersonic case are shown to behave similarly to the subsonic case. Epicyclic roots can now clearly be seen to diverge

for $b/b_{nom} < 1.0$ with decreasing oscillatory trends, as two roots becoming noticeably more damped and two becoming slightly less damped. The roll/yaw mode now becomes increasing unstable for values less than $b/b_{nom} \approx 0.30$.

Table 11: Orthonormalized eigenmatrix for $b/b_{nom} = 0.0$ at $Ma = 0.5$.

	Velocity Mode	**Roll/Yaw Mode**	**Vertical Epicyclic Mode**		**Horizontal Epicyclic Mode**	
V	1.00	0.00	0.00	0.00	0.00	0.00
p	0.00	0.89	0.00	0.00	0.26	0.26
$\tilde{v}$	0.00	0.05	0.48	0.48	0.35	0.35
$\tilde{w}$	0.00	0.05	0.48	0.48	0.35	0.35
$\tilde{q}$	0.00	0.00	0.02	0.02	0.02	0.02
$\tilde{r}$	0.00	0.00	0.02	0.02	0.02	0.02

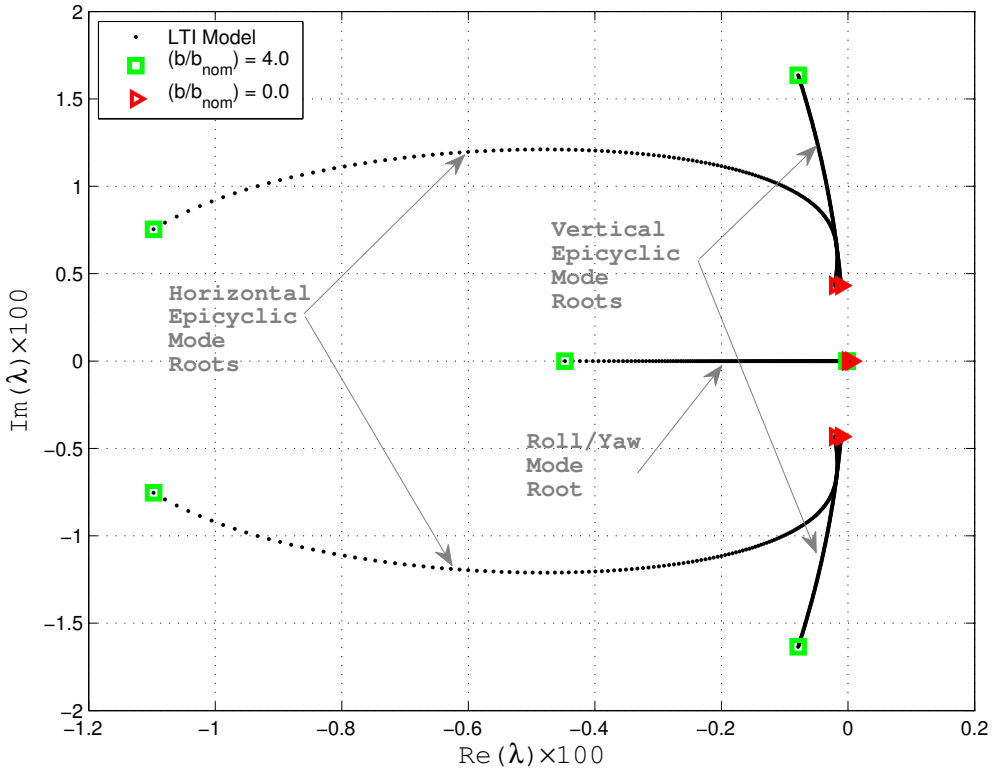

Figure 84: Root Locus: Parameterized by variation of F1 and F2 fin lengths. Subsonic Case: Mach 0.5.

Table 12: Orthonormalized eigenmatrix for $b/b_{nom} = 0.0$ at $Ma = 3.0$.

	Velocity Mode	Roll/Yaw Mode	Horizontal Epicyclic Mode		Vertical Epicyclic Mode	
V	0.88	0.00	0.00	0.00	0.00	0.00
p	0.00	0.49	0.00	0.00	0.41	0.41
$\tilde{v}$	0.06	0.25	0.50	0.50	0.29	0.29
$\tilde{w}$	0.06	0.25	0.50	0.50	0.29	0.29
$\tilde{q}$	0.00	0.01	0.00	0.00	0.01	0.01
$\tilde{r}$	0.00	0.01	0.00	0.00	0.01	0.01

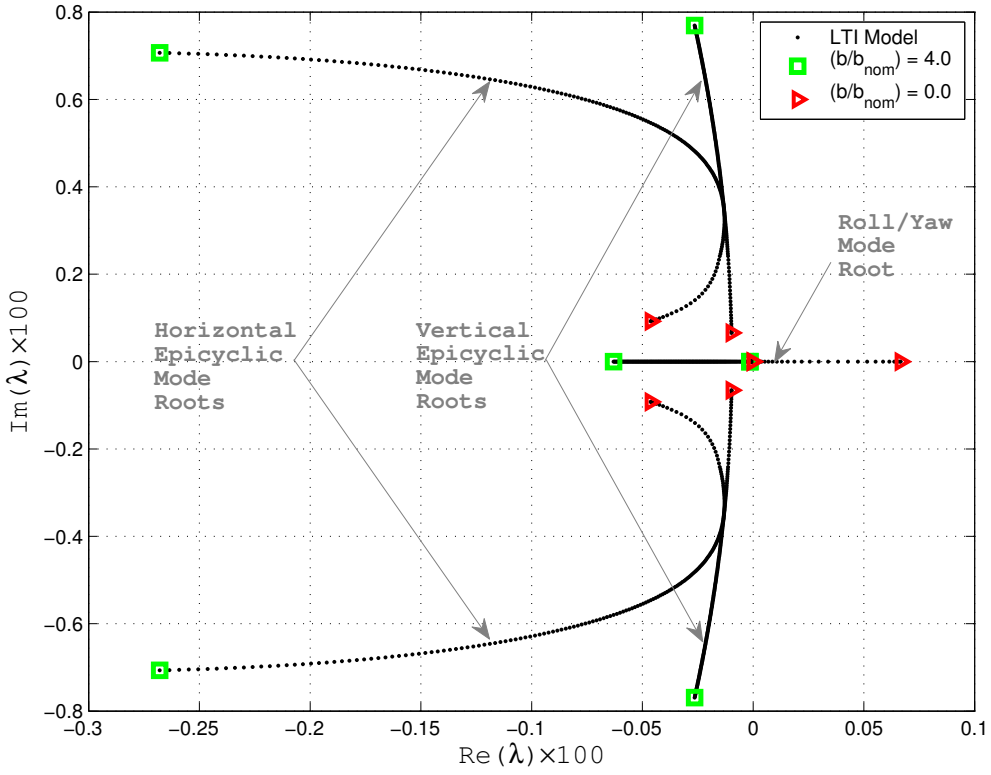

Figure 85: Root Locus: Parameterized by variation of F1 and F2 fin lengths. Supersonic Case: Mach 3.0.

5.2 Trade Study – Vary Fin Parameters Off of the Baseline 3-Finned Projectile Configuration

The purpose of the following trade studies is to investigate the effects of varying fin length (or equivalently fin area) off of a baseline 3-finned projectile. Figure 86 shows an illustration of a projectile with three fins placed symmetrically at the rear of the projectile. Table 86 summarizes fin geometry, where the i^{th} fin length, width, azimuth angle, and cant angle are represented by b_i, c_i, ϕ_{C_i}, and δ_{C_i}, respectively.

Table 13: Summary Baseline 3-Finned Projectile Parameters

Fin#	b_i (ft)	c_i (ft)	ϕ_{C_i} (deg)	δ_{C_i} (deg)
F1	0.0984	0.0984	90	0.00
F2	0.0984	0.0984	210	0.00
F3	0.0984	0.0984	330	0.00

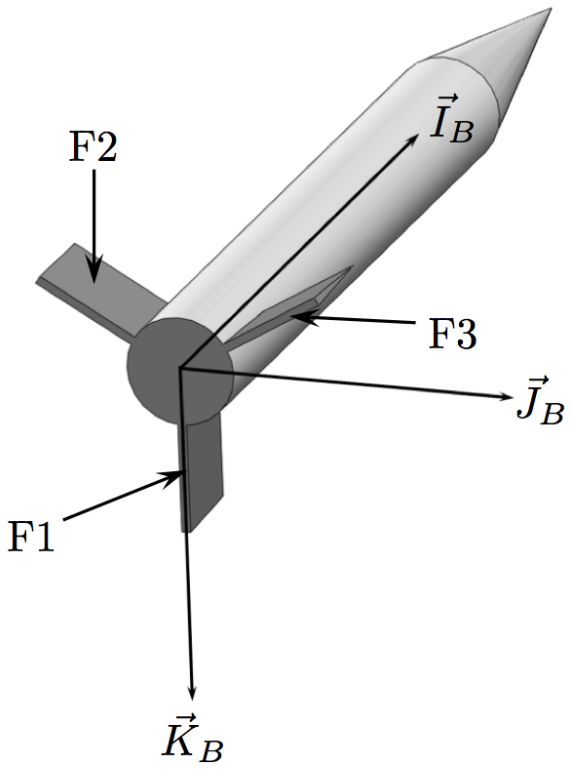

Figure 86: Illustration of the baseline 3-finned projectile configuration.

5.2.1 Effect of Variation of F1 Fin Length on Stability

In the following trade study, projectile dynamic stability was evaluated for variation of F1 fin length (or equivalently fin area). Given the nominal fin lengths previously summarized in Table 4, stability roots were calculated as F1 fin length varied between $0 \leq b \leq 4b_{nom}$. Projectile quasi-linear roll rate and roll angle were set to 0.0 (rad/sec) and 0.0 (deg), respectively. Both subsonic and supersonic cases were considered, where the quasi-linear total velocity was set to 558.0 (ft/sec) (Mach 0.5) in the subsonic case and 3357.0 (ft/sec) (Mach 3.0) in the supersonic case. Dynamic simulation for this study showed that the LTI model was sufficient to approximate the 6DOF model for at least 1.0 (sec) of flight time for values of b where the system was stable. In the supersonic case, the system was observed to grow increasingly unstable in the roll/yaw mode as the fin length approached 0.0 (ft).

Figure 87 shows the subsonic behavior of the dynamic modes with changing b, and Table 14 shows the LTI mode structure at $b/b_{nom} = 0.0$. The vertical epicyclic mode roots are invariant in b, since the vertical fin F1 only affects horizontal plane aerodynamic forces. When $b/b_{nom} = 4.0$, the horizontal epicyclic mode roots are highly oscillatory and heavily damped. As the fin length is varied until $b/b_{nom} = 1.0$, the horizontal epicyclic mode roots converge upon the vertical epicyclic mode roots. Reducing the fin length further down towards $b/b_{nom} = 0.0$, causes the horizontal mode roots to diminish in frequency and become slightly mode damped. The roll/yaw mode crosses the imaginary axis at $b/b_{nom} \approx 0.38$, driving the system unstable.

Figure 88 shows the root locus for the supersonic case of parametric variation of b. For values of fin length $b/b_{nom} > 1.0$, the epicyclic and roll/yaw modes vary in similar fashion to the subsonic case. For values of $b < b_{nom}$, the system becomes increasingly sensitive to changing b. The horizontal epicyclic mode changes an oscillatory mode to an aperiodic mode for fin lengths less than $b/b_{nom} \approx 0.46$. The roll/yaw mode crosses the imaginary axis at $b/b_{nom} \approx 0.64$, driving the system unstable.

Table 14: Orthonormalized eigenmatrix for $b/b_{nom} = 0.0$ at $Ma = 0.5$.

	Velocity Mode	Roll/Yaw Mode	Vertical Epicyclic Mode		Horizontal Epicyclic Mode	
V	0.99	0.00	0.00	0.00	0.00	0.00
p	0.00	0.84	0.00	0.00	0.39	0.39
$\tilde{v}$	0.00	0.16	0.00	0.00	0.60	0.60
$\tilde{w}$	0.01	0.00	0.95	0.95	0.00	0.00
$\tilde{q}$	0.00	0.00	0.05	0.05	0.00	0.00
$\tilde{r}$	0.00	0.00	0.00	0.00	0.01	0.01

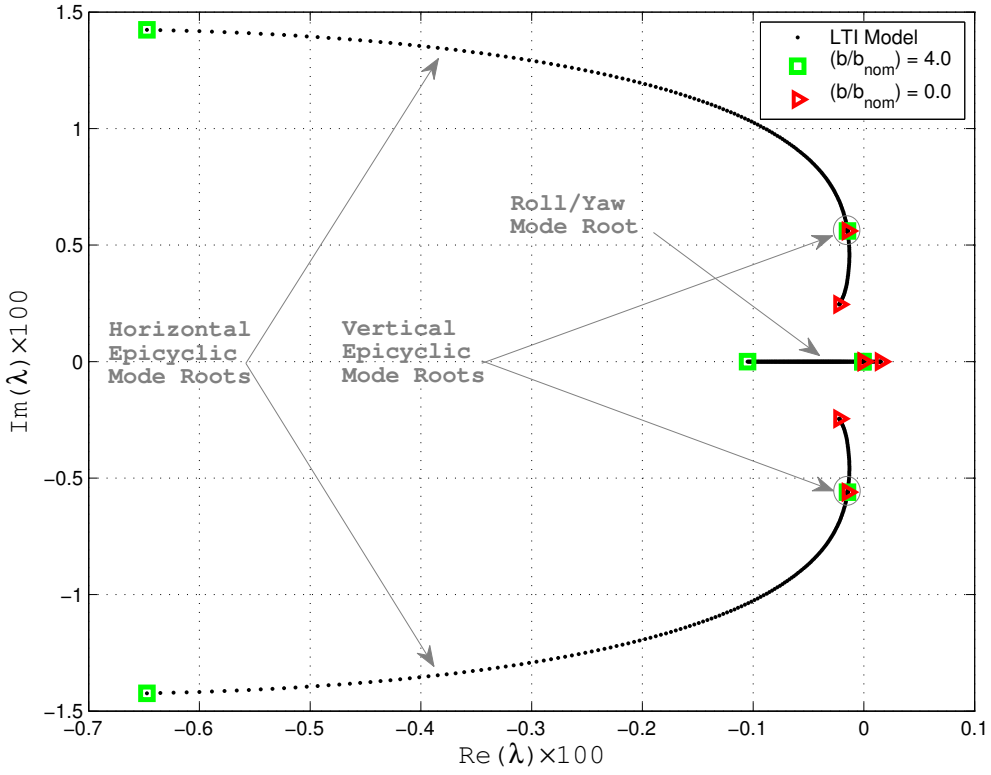

Figure 87: Root Locus: Parameterized by variation of F1 fin length. Subsonic Case: Mach 0.5.

Table 15: Orthonormalized eigenmatrix for $b/b_{nom} = 0.0$ at $Ma = 3.0$.

	Velocity Mode	Roll/Yaw Mode	Vertical Epicyclic Mode		Horizontal Epicyclic Mode	
V	0.98	0.00	0.00	0.00	0.00	0.00
p	0.00	0.91	0.00	0.00	0.23	0.23
$\tilde{v}$	0.00	0.09	0.00	0.00	0.75	0.75
$\tilde{w}$	0.02	0.00	0.97	0.97	0.00	0.00
$\tilde{q}$	0.00	0.00	0.03	0.03	0.00	0.00
$\tilde{r}$	0.00	0.00	0.00	0.00	0.02	0.02

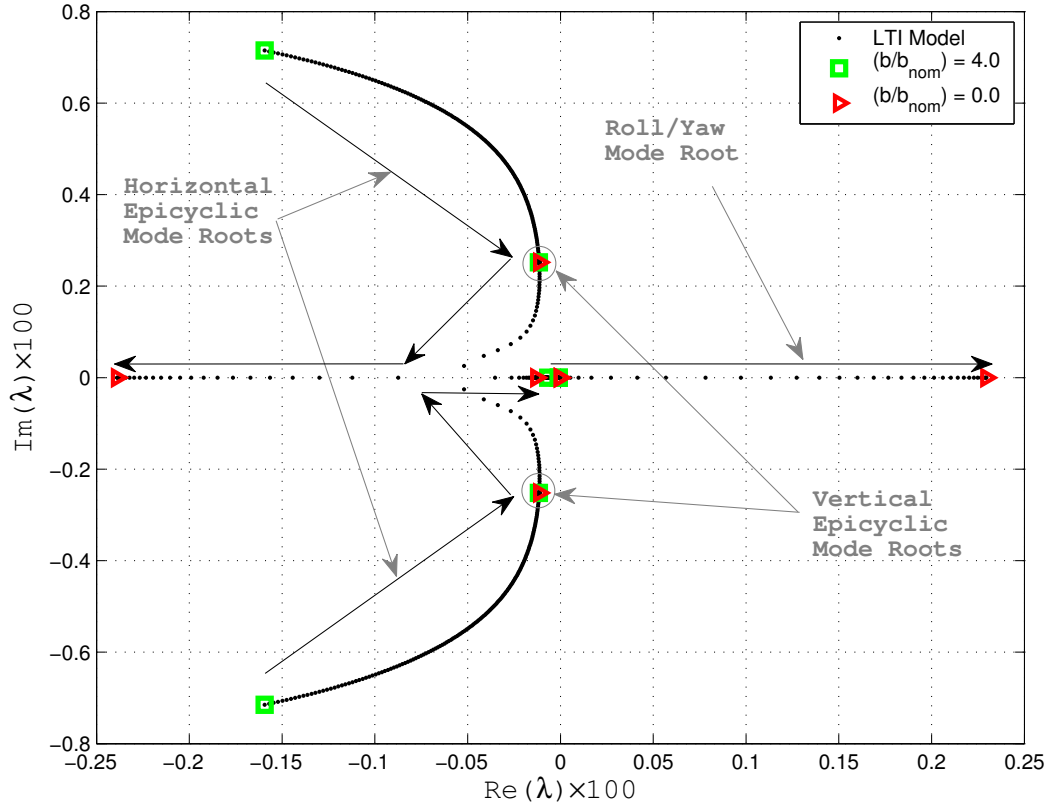

Figure 88: Root Locus: Parameterized by variation of F1 fin length. Supersonic Case: Mach 3.0.

5.2.2 Effect of Roll Rate on V-tailed Projectile Stability

Here a stability analysis is performed on an asymmetric 2-finned V-tail projectile as roll rate was varied from 0.0 (rad/sec) $\leq p_o \leq$ 1000 (rad/sec). Again, the goal is to determine if dynamic instabilities can be "rolled-out" with increasing roll rate, which is commonly done to stabilize finless projectiles. Dynamic simulations were run to compare LTI, LTP, and 6DOF models for the 2-finned V-tail projectile shown in Figure 89. The fin geometry summarized in Table 6 was used for to describe the two fins, designated as F2 and F3. Several initial rolls rates were simulated for the projectile launched subsonically at Mach 0.5 and a quadrant elevation of 1.0286 (deg). As initial roll rate varied, a cant angle was set for the two fins to encourage a constant, steady roll rate through flight. For a flight speed of Mach 0.5, fin cant is proportional to the initial roll rate by the relation δ_{c_i} (deg) $\approx 0.0047 p_o$. The LTP was able to successfully approximate the 6DOF trajectory results for 1.0 seconds of flight for stable cases.

Figure 90 shows results of the LTP model stability analysis as roll rate was varied from 0.0 (rad/sec) $\leq p_o \leq$ 1000 (rad/sec). For small values of roll rate, $p_o <$ 0.1 (rad/sec), the system is observed to be unstable as one root is real and positive. As roll rate increases to $p_o \approx$ 1.0 (rad/sec), the system is stable and fast and slow epicyclic dynamic modes start to appear. Unlike the symmetric 2-finned projectile roll rate study of *Section 5.1.2*, the fast mode epicyclic roots decrease in stability, while the slow mode epicyclic roots become more stable. At a roll rate of $p_o \approx$ 70.8 (rad/sec), the system again becomes unstable as the fast mode roots cross the imaginary axis. Therefore, this projectile configuration can be dynamically stabilized however, unlike the symmetric 2-finned case the V-tail configuration can become dynamically unstable if the roll rate is large enough.

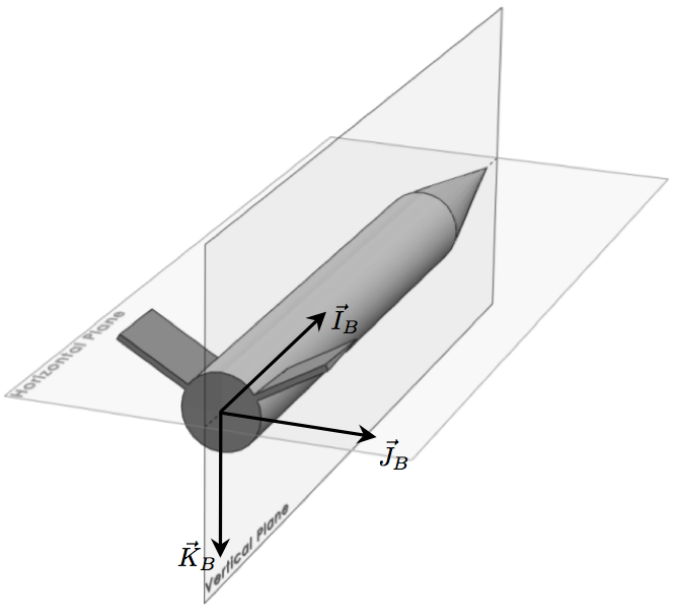

Figure 89: Illustration of a 2-finned V-tail projectile that is aerodynamically asymmetric about the vertical plane of the body frame.

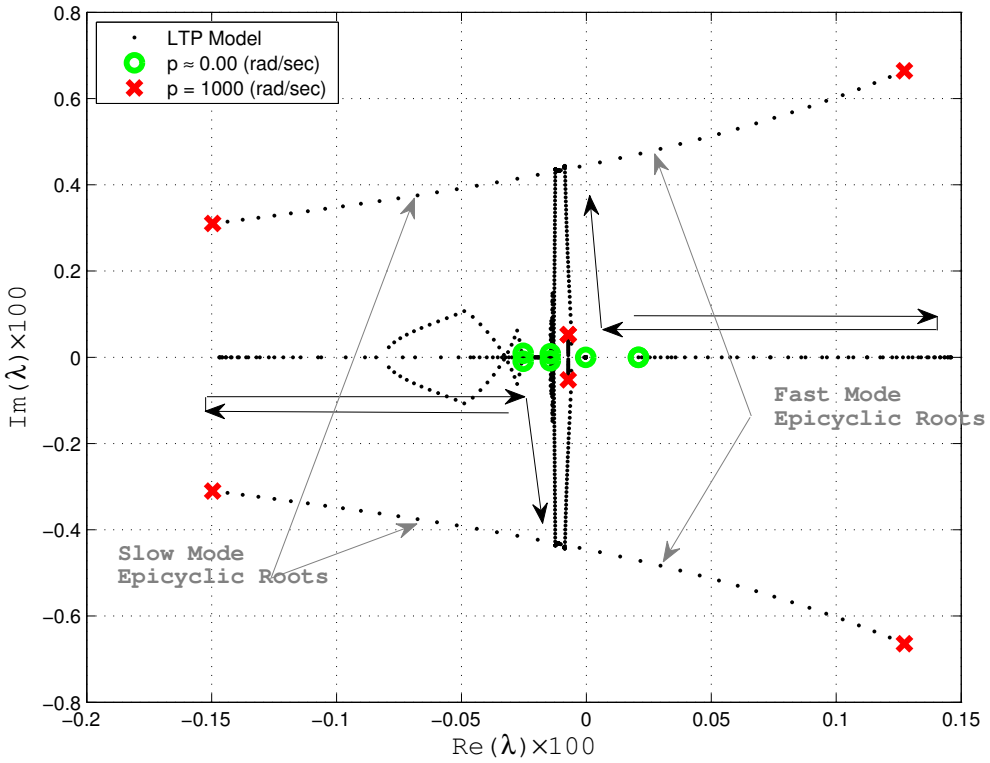

Figure 90: Root Locus: Parameterized by projectile spin rate p at Mach 0.5.

5.3 Trade Study – Vary Fin Parameters Off The Baseline Hybrid Aircraft/Projectile Configuration

The purpose of the following trade studies is to investigate the effects of varying wing and tail parameters off of a baseline hybrid aircraft/projectile. Figure 91 shows an illustration of the baseline hybrid configuration with two wings placed behind the projectile mass center and two fins placed at the rear of the projectile. Table 16 summarizes the nominal lifting surface geometry of the baseline configuration. The i^{th} wing span, chord, stationline, dihedral angle, and cant angle are represented by W_i, C_i, SL_{W_I}, Γ_{W_i}, and α_{W_i}, respectively. The i^{th} fin length, width, V-tail angle, and cant angle are represented by b_i, c_i, θ_V, and δ_{C_i}.

Table 16: Summary Baseline Hybrid Aircraft/Projectile Parameters

Wing#	W_i (ft)	C_i (ft)	Γ_{W_i} (deg)	α_{W_i} (deg)	SL_{W_i} (ft)
W1	0.3936	0.0984	5.0	0.00	0.35
W2	0.3936	0.0984	5.0	0.00	0.35
Fin#	b_i (ft)	c_i (ft)	θ_V (deg)	δ_{C_i} (deg)	
F1	0.0984	0.0984	120.0	0.00	
F2	0.0984	0.0984		0.00	

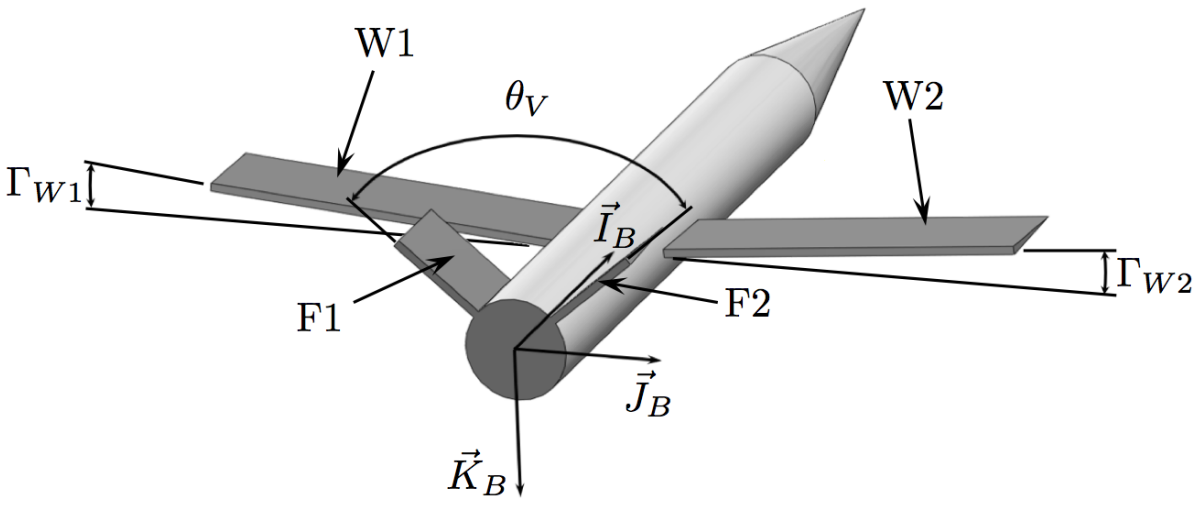

Figure 91: Illustration of the baseline hybrid aircraft/projectile configuration.

5.3.1 Effect of Fight Speed on Stability

In the following trade study, projectile dynamic stability was evaluated for variation of flight speed from $0.50 \leq \text{Ma} \leq 1.00$. Projectile quasi-linear roll rate and roll angle were set to 0.0 (rad/sec) and 0.0 (deg), respectively. Flight dynamic simulation for this study showed that the LTI model was sufficient to approximate the 6DOF model for at least 1.0 (sec) of flight time for Mach numbers where the system was observed to be stable.

Figure 92 shows the root locus for variation in Mach number for the hybrid projectile, and Table 17 shows the LTI mode structure at $b/b_{nom} = 0.0$. Recall from *Chapter 2* that all aerodynamic coefficients are dependent upon Mach number. Therefore within the extended PLT matrix of Equation (65) varying Mach number changes both quasi-linear flight speed V_o and aerodynamic coefficients. As Mach number increases from 0.5 to 0.82, little variation is seen in epicyclic roots. Two vertical plane roots decrease in frequency for near constant damping, and two horizontal roots increase subtly in frequency. Note that as seen in Table 17, the horizontal epicyclic mode is significantly influenced by roll rate. The roll mode root increases significantly in damping along the real axis during this Mach regime, however. As Mach number increases above $\text{Ma} \approx 0.82$, sensitivity of the vertical epicyclic mode to increasing Mach number increases, while sensitivity in the other modes remains relatively unaffected. At $\text{Ma} \approx 0.98$, an instability occurs in the vertical plane, as epicyclic roots collide at the real axis and change into aperiodic modes. Physically speaking, this instability is explained by the movement of the resultant aerodynamic center along the stationline axis ($\vec{I}_B$). As Mach number increases, the aerodynamic center moves in front of the projectile mass center, causing the projectile to change from a stable nose-down tendency to an unstable nose-up tendency. During this transonic Mach regime, horizontal plane epicyclic roots change very little, while the roll mode continues to increase in stability along the real axis.

Table 17: Orthonormalized eigenmatrix for $Ma = 0.82$.

	Velocity Mode	Roll Mode	Horizontal Epicyclic Mode		Vertical Epicyclic Mode	
V	1.00	0.00	0.00	0.00	0.00	0.00
p	0.00	0.99	0.38	0.38	0.00	0.00
$\tilde{v}$	0.00	0.00	0.61	0.61	0.00	0.00
$\tilde{w}$	0.00	0.00	0.00	0.00	0.92	0.92
$\tilde{q}$	0.00	0.00	0.00	0.00	0.08	0.08
$\tilde{r}$	0.00	0.00	0.01	0.01	0.00	0.00

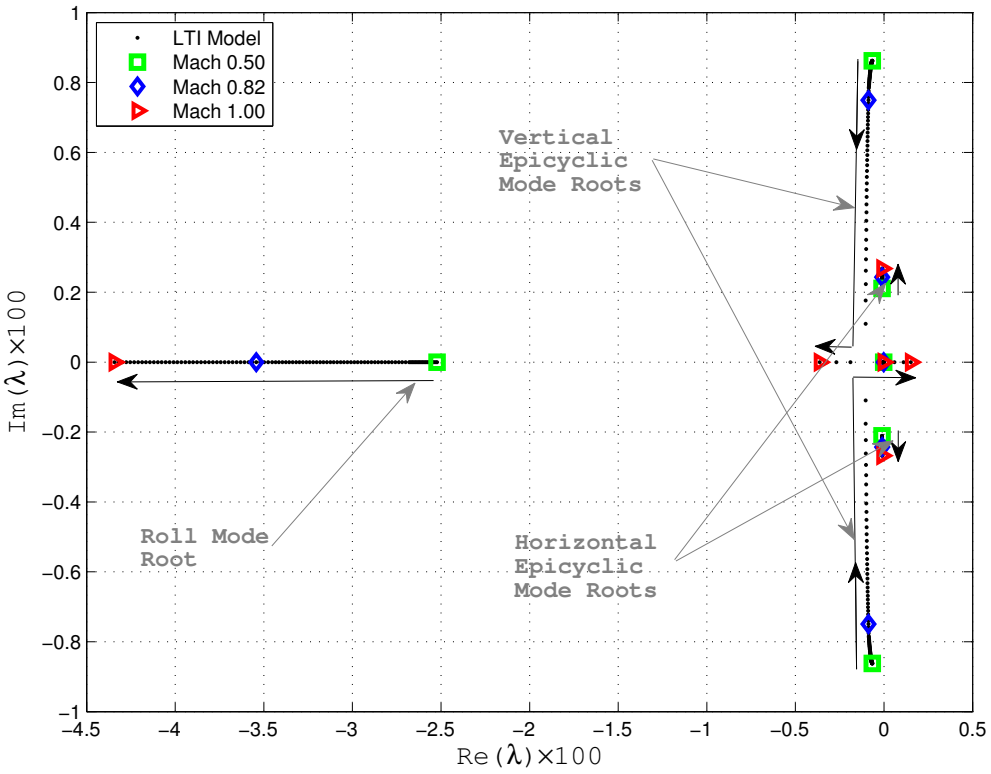

Figure 92: Root Locus: Parameterized by Mach number

5.3.2 Effect of Variation of W1 and W2 Wing Span Lengths on Stability

In the following trade study, projectile dynamic stability was evaluated for symmetric variation of W1 and W2 wing spans (or equivalently wing planform areas). Given the nominal wing lengths previously summarized in Table 16, stability roots were calculated as W1 and W2 wing spans varied between $0 \leq W \leq W_{nom}$. Projectile quasi-linear roll rate and roll angle were set to 0.0 (rad/sec) and 0.0 (deg), and the quasi-linear total velocity was set to 558.0 (ft/sec) (Mach 0.5). Flight dynamic simulation for this study showed that the LTI model was sufficient to approximate the 6DOF model for at least 1.0 (sec) of flight time for values of W where the system was observed to be stable.

Figure 93 shows the root locus for parametric variation of wing span W, and Table 18 shows the LTI mode structure at $W/W_{nom} = 0.0$. As W is reduced, the vertical epicyclic mode roots reduce in frequency and become lightly damped. The horizontal epicyclic mode roots vary in frequency and stability but do not significantly change for all values of W. The roll/yaw mode root is initially heavily damped when $W/W_{nom} = 1.0$ but quickly drives the system unstable for values of wing span below $W/W_{nom} \approx 0.46$. The sensitivity of the roll/yaw mode to changing wing span length greatly diminishes as W approaches 0.0 (ft) to the point where it almost becomes invariant in W.

Table 18: Orthonormalized eigenmatrix for $W/W_{nom} = 0.0$ at $Ma = 0.5$.

	Velocity Mode	Roll/Yaw Mode	Horizontal Epicyclic Mode		Vertical Epicyclic Mode	
V	1.00	0.00	0.00	0.00	0.00	0.00
p	0.00	0.73	0.56	0.56	0.00	0.00
$\tilde{v}$	0.00	0.27	0.43	0.43	0.00	0.00
$\tilde{w}$	0.00	0.00	0.00	0.00	0.95	0.95
$\tilde{q}$	0.00	0.00	0.00	0.00	0.05	0.05
$\tilde{r}$	0.00	0.00	0.01	0.01	0.00	0.00

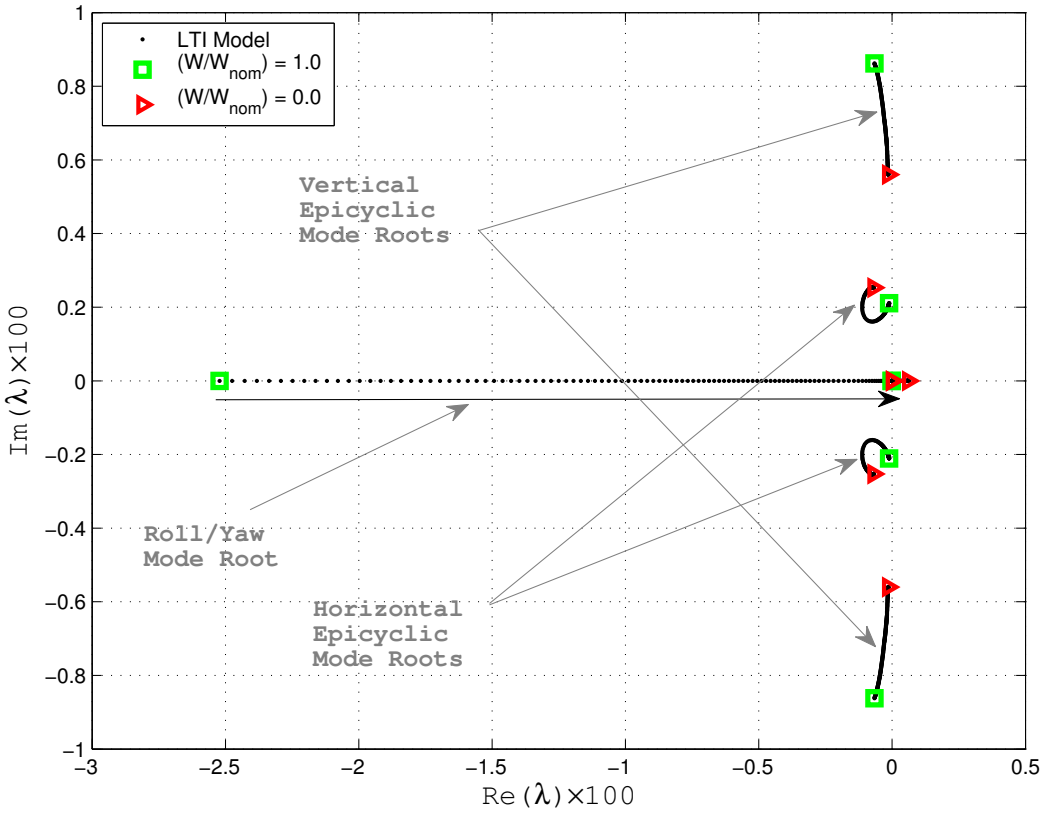

Figure 93: Root Locus: Parameterized by symmetric variation of W1 and W2 wing spans at Mach 0.5.

5.3.3 Effect of Variation of F1 and F1 Fin Lengths on Stability

In the following trade study, projectile dynamic stability was evaluated for symmetric variation of F1 and F2 fin lengths (or equivalently fin planform areas). Given the nominal wing lengths previously summarized in Table 16, stability roots were calculated as F1 and F2 wing spans varied between $0 \leq b \leq 4b_{nom}$. Projectile quasi-linear roll rate and roll angle were set to 0.0 (rad/sec) and 0.0 (deg), and the quasi-linear total velocity was set to 558.0 (ft/sec) (Mach 0.5). Flight dynamic simulation for this study showed that the LTI model was sufficient to approximate the 6DOF model for at least 1.0 (sec) of flight time for values of b where the system was observed to be stable.

Figure 94 shows the root locus for parametric variation of fin length b, and Table 94 shows the LTI mode structure at $b/b_{nom} = 0.0$. As b is reduced, the vertical epicyclic mode roots reduce in frequency and become lightly damped. Also, the horizontal epicyclic mode roots quickly reduce in frequency towards the real axis, approaching each other. The system becomes unstable at approximately $b/b_{nom} \approx 0.7114$ as these roots collide and split into aperiodic modes. The roll mode root decreases along the real axis as b is reduced but remains significantly damped for $b/b_{nom} = 0.0$.

Table 19: Orthonormalized eigenmatrix for $b/b_{nom} = 0.0$ at $Ma = 0.5$.

	Velocity Mode	Roll/Yaw Mode	Horizontal Epicyclic Mode		Vertical Epicyclic Mode	
V	1.00	0.00	0.00	0.00	0.00	0.00
p	0.00	1.00	0.30	0.30	0.00	0.00
$\tilde{v}$	0.00	0.00	0.68	0.68	0.00	0.00
$\tilde{w}$	0.00	0.00	0.00	0.00	0.94	0.94
$\tilde{q}$	0.00	0.00	0.00	0.00	0.06	0.06
$\tilde{r}$	0.00	0.00	0.02	0.02	0.00	0.00

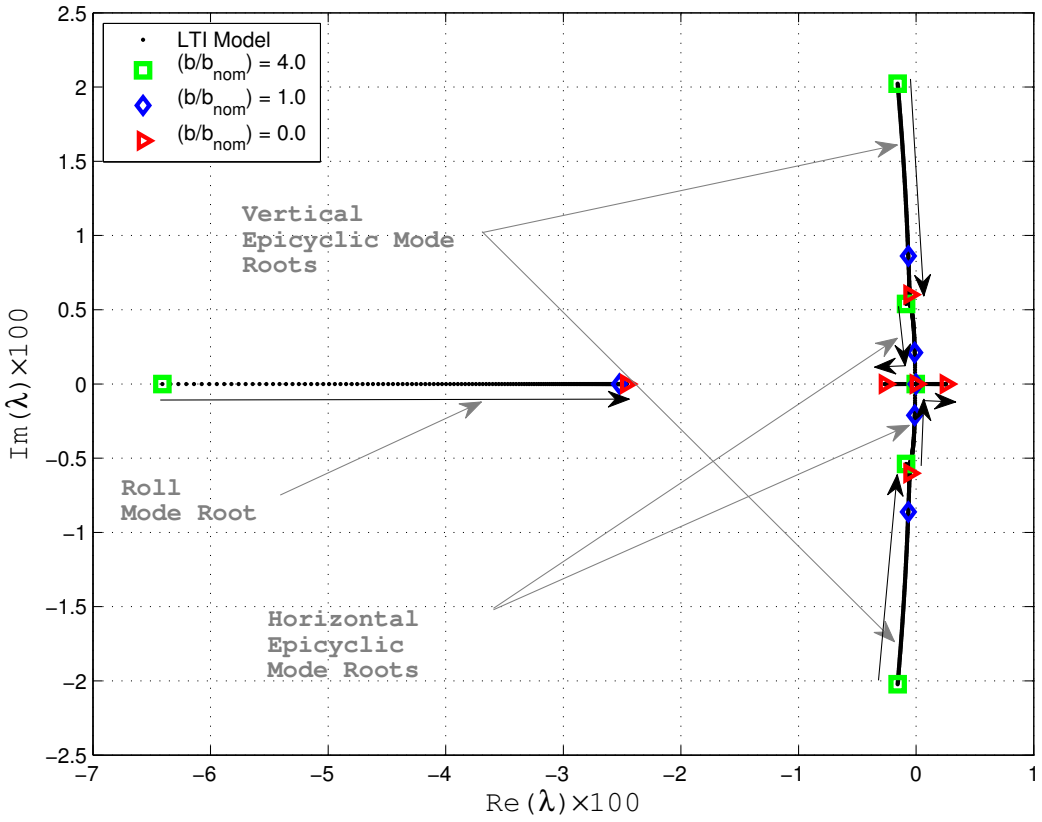

Figure 94: Root Locus: Parameterized by symmetric variation of F1 and F2 fin lengths at Mach 0.5.

5.3.4 Effect of Variation of V-tail Angle on Stability

In the following trade study, projectile dynamic stability was evaluated for variation of fin V-tail angle from 45 (deg) $\leq \theta_V \leq$ 180 (deg). Projectile quasi-linear roll rate and roll angle were set to 0.0 (rad/sec) and 0.0 (deg), and the quasi-linear total velocity was set to 558.0 (ft/sec) (Mach 0.5). Flight dynamic simulation for this study showed that the LTI model was sufficient to approximate the 6DOF model for at least 1.0 (sec) of flight time for values of θ_V where the system was observed to be stable.

Figure 95 shows the root locus for parametric variation of θ_V, and Table 20 shows the LTI mode structure at $\theta_V = 180$ (deg). For all values of θ_V, the roll mode is heavily damped and remained unchanged, meaning that this mode is completely insensitive and invariant to changing θ_V. For $\theta_V = 45$ (deg), the vertical and horizontal epicyclic modes are relatively close in stability and frequency. As θ_V is increased, frequency of the vertical epicyclic mode increases with reducing sensitivity to θ_V, while the damping remaans approximately constant. Conversely, the vertical epicyclic roots reduce in frequency and increase in sensitivity for large θ_V. Eventually these roots collide with each other at the real axis and become aperiodic. This occurs at $\theta_V \approx$ 133.53 (deg), where the system becomes unstable shortly thereafter.

Table 20: Orthonormalized eigenmatrix for $\theta_V = 180.0$ (deg) at $Ma = 0.5$.

	Velocity Mode	Roll Mode	Horizontal Epicyclic Mode		Vertical Epicyclic Mode	
V	1.00	0.00	0.00	0.00	0.00	0.00
p	0.00	1.00	0.30	0.30	0.00	0.00
$\tilde{v}$	0.00	0.00	0.68	0.68	0.00	0.00
$\tilde{w}$	0.00	0.00	0.00	0.00	0.91	0.91
$\tilde{q}$	0.00	0.00	0.00	0.00	0.09	0.09
$\tilde{r}$	0.00	0.00	0.02	0.02	0.00	0.00

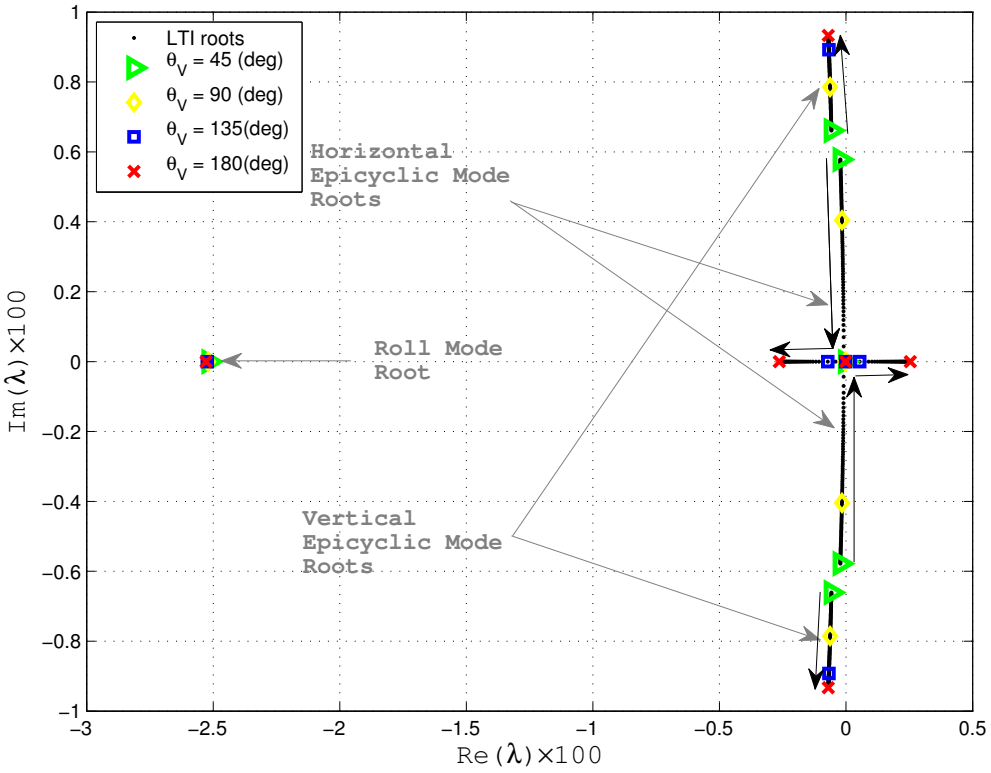

Figure 95: Root Locus: Parameterized by variation of θ_V at Mach 0.5.

5.3.5 Effect of Variation of Wing Dihedral on Stability

In the following trade study, projectile dynamic stability was evaluated for symmetric variation of wing dihedral angles Γ_{W1} and Γ_{W2}. Stability roots were calculated as wing dihedral varied from -45 (deg) $\leq \Gamma \leq 45$ (deg). Projectile quasi-linear roll rate and roll angle were set to 0.0 (rad/sec) and 0.0 (deg), and the quasi-linear total velocity was set to 558.0 (ft/sec) (Mach 0.5). Flight dynamic simulation for this study showed that the LTI model was sufficient to approximate the 6DOF model for at least 1.0 (sec) of flight time for values of Γ where the system was observed to be stable.

Figure 96 shows the root locus for symmetric variation of wing dihedral Γ, and Table 21 shows the LTI mode structure at $\Gamma = -45$ (deg). As Γ is increased from -45 (deg) to 0.0 (deg), the vertical epicyclic roots increase in frequency and become slightly more damped, while the horizontal epicyclic roots decrease in frequency and become less damped. The behavior of roll mode over this range is a net increase in damping, which maximizes at $\Gamma \approx -9.0$ (deg). Also at $\Gamma \approx -9.0$ (deg), the horizontal epicyclic mode roots become very lightly damped. For increasing values of Γ larger than 0.0 (deg), vertical epicyclic root behavior decreases in frequency and damping. For $\Gamma = 45$ (deg), frequency and damping for these roots is equal to what was calculated for the -45 (deg) case. Similarly, the roll mode returns to a value near its calculated root for the -45 (deg) case but is slightly less damped. For wing dihedral larger than $\Gamma \approx 23.74$ (deg), behavior of the horizontal epicyclic roots eventually drives the system to instability as these roots collide with each other at the real axis and become aperiodic in nature.

Recall from *Section 2.5.3* that the effects of gravity were observed not to be depend upon any dynamic states and therefore do not appear in the PLT matrix $\mathbf{A}$. Instead, gravitational effects were included in a forcing vector B. Due to this fact, hybrid configurations with negative dihedral could also be equivalently considered have positive dihedral but with an inverted V-tail (upside down tail configuration).

Therefore the root locus plot suggests that hybrid projectiles with inverted V-tail fin configurations retain stability characteristics for large wing dihedral angles, while projectiles with upright V-tail fin configurations do not.

Table 21: Orthonormalized eigenmatrix for $\Gamma = -45.0$ (deg) at $Ma = 0.5$.

	Velocity Mode	**Roll/Yaw Mode**	**Horizontal Epicyclic Mode**		**Vertical Epicyclic Mode**	
V	0.97	0.00	0.00	0.00	0.00	0.00
p	0.00	1.00	0.80	0.80	0.00	0.00
$\tilde{v}$	0.00	0.00	0.20	0.20	0.00	0.00
$\tilde{w}$	0.03	0.00	0.00	0.00	0.93	0.93
$\tilde{q}$	0.00	0.00	0.00	0.00	0.07	0.07
$\tilde{r}$	0.00	0.00	0.01	0.01	0.00	0.00

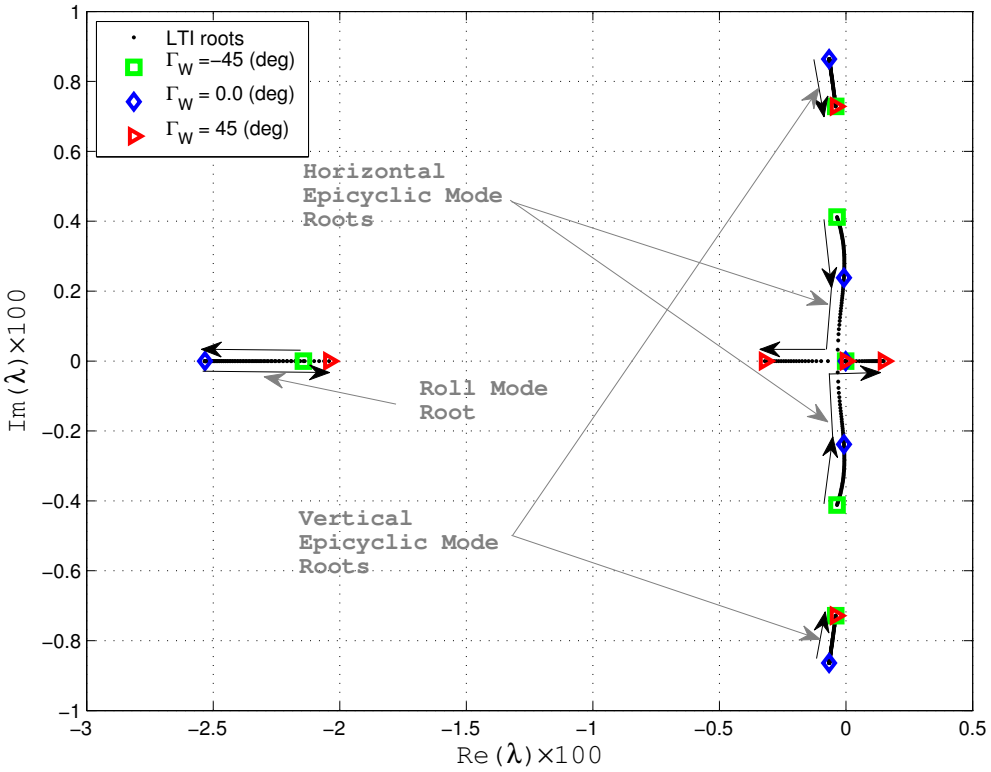

Figure 96: Root Locus: Parameterized by symmetric variation of Γ_{W1} and Γ_{W2} at Mach 0.5.

5.3.6 Nonlinear Effects of Geometric Parameter Space on Stability

The parameter space characterized by lifting surface position and orientation dimensions is highly nonlinear and can be sensitive to small parameter changes. In other words, parametric variation of a single parameter about a non-nominal configuration is not guaranteed to generate even remotely similar root loci. Consequentially, significant portions of the parameter space should be mapped out to gain a more complete understanding how a given system behaves. The objective of this trade study is to map out a portions of the nonlinear parameter space by generating root loci for different wing span lengths (or equivalently wing planform areas), while varying the fin V-tail angle. The V-tail angle is continuously varied from 0.00 (deg) $\leq \theta_V \leq$ 180 (deg), while the wing span lengths W1 ad W2 are symmetrically changed by the discrete values: $W/W_{nom} = 0.0$, 0.50, and 1.00. All other lifting surface parameters were set to the nominal values previously summarized. Projectile quasi-linear roll rate and roll angle were set to 0.0 (rad/sec) and 0.0 (deg), and the quasi-linear total velocity was set to 558.0 (ft/sec) (Mach 0.5). Flight dynamic simulation for this study showed that the LTI model was sufficient to approximate the 6DOF model for at least 1.0 (sec) of flight time for values of Γ where the system was observed to be stable.

Figure 97 shows the root locus for parametric variation of θ_V for the hybrid projectile with no wings $W/W_{nom} = 0.0$. Alternatively, this plot shows the root locus for parametric variation of θ_V as a 2-finned projectile is transformed from a severely asymmetric V-tail projectile (*Section* 5.2.2) to a symmetric 2-finned configuration (*Section* 5.1.2). Inspection of system eigenfunctions revealed the following characteristic modes: a total velocity mode, a roll/yaw mode, a pair of vertical epicyclic modes, and a pair of horizontal epicyclic/roll modes. The roll/yaw mode was observed to vary in characteristic response for changing θ_V. For small θ_V, this mode is heavily influenced by roll rate. As θ_V becomes large, this mode is influenced by the horizontal transverse velocity a moderate amount and the horizontal transverse angular velocity

a small amount.

For all values of θ_V the root locus is unstable, since at $\theta_V = 0.0$ (deg) the roll/yaw mode root and one vertical plane epicyclic root are real and positive. As θ_V increases, the aperiodic vertical epicyclic mode roots converge towards each other along the real axis and collide for a stable value. For $\theta_V \geq 43.2$ (deg), these roots split into oscillatory branches and diverge with increasing frequency and stability. For increasing θ_V, the horizontal epicyclic/roll mode roots diminish in frequency and converge towards each other, first at a near constant damping but then become more stable before meeting at the real axis. For $\theta_V \geq 153.9$ (deg), these roots split into aperiodic branches. One of these aperiodic roots continues to decrease in stability but never cross over the imaginary axis. The roll/yaw mode root continues to increase in instability as θ_V is increased.

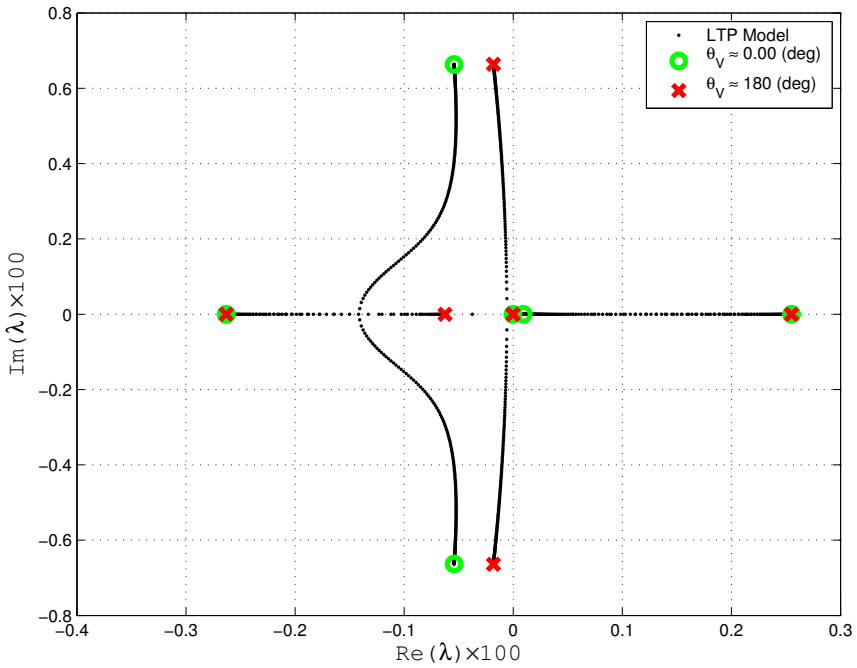

Figure 97: Root Locus: Parameterized by variation of θ_V at $W/W_{nom} = 0.0$ and Mach 0.5.

Figure 98 shows the root locus for parametric variation of θ_V for the hybrid projectile with no wings $W/W_{nom} = 0.5$. Inspection of system eigenfunctions revealed the following characteristic modes: a total velocity mode, a roll/yaw mode, a pair of vertical epicyclic modes, and a pair of horizontal epicyclic/roll modes. The roll/yaw mode was observed to vary in characteristic response for changing θ_V. For small θ_V, the roll/yaw mode is heavily influenced by roll rate, but as θ_V becomes large, this mode influences the transverse velocity a significant amount.

As θ_V increases, the vertical epicyclic mode roots grow in frequency and damping, and the horizontal epicyclic/roll mode roots start to converge towards each other. The motion of the horizontal epicyclic/roll roots is at first nearly constant in stability, but then these roots start to drift towards increasing stability. At $\theta_V = 0.0$ (deg), the roll/yaw mode root is stable but this root eventually drives the system unstable at $\theta_V \geq 123.3$ (deg).

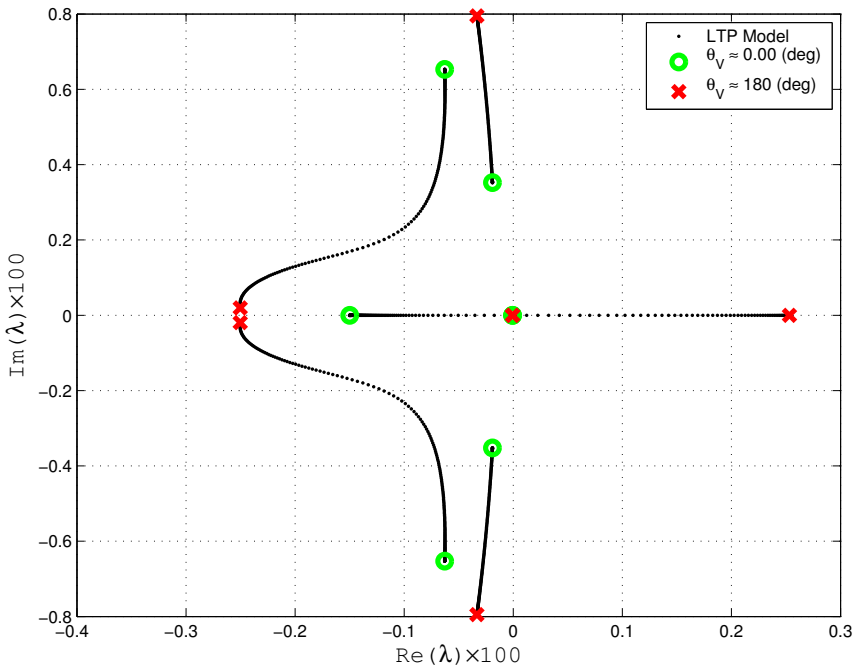

Figure 98: Root Locus: Parameterized by variation of θ_V at $W/W_{nom} = 0.5$ and Mach 0.5.

Figure 99 shows the root locus for parametric variation of θ_V for the hybrid projectile with no wings $W/W_{nom} = 1.0$. Discussion of this root locus was addressed previously in *Section* 5.3.4.

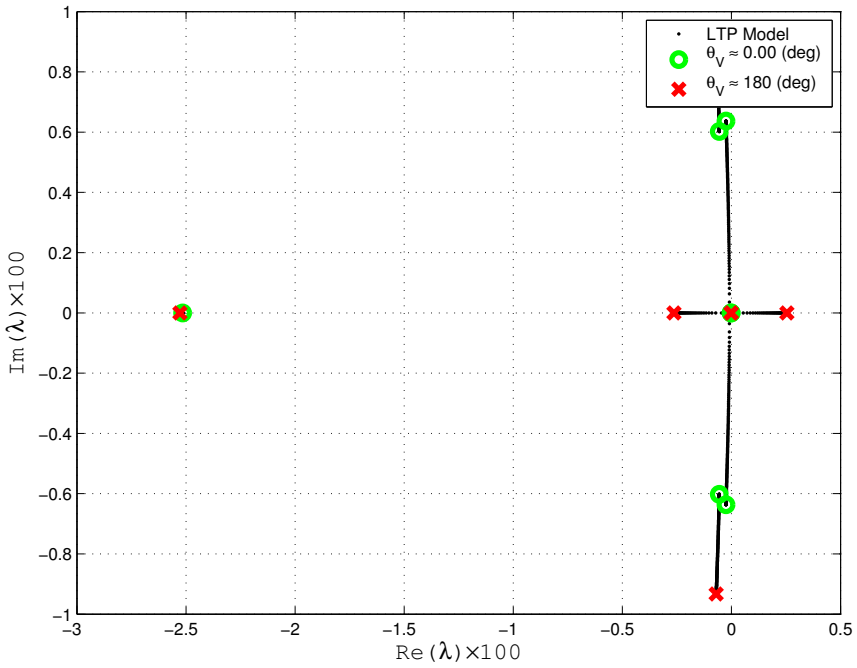

Figure 99: Root Locus: Parameterized by variation of θ_V at $W/W_{nom} = 1.0$ and Mach 0.5.

The root loci in Figures 97-99 shows different dynamic behavior as θ_V was continuously varied. For $W/W_{nom} = 0.0$ both vertical and horizontal epicyclic modes grew unstable but at different extremes of the trade study. For $W/W_{nom} = 0.5$ the roll/yaw mode was the only source for dynamic instability. Finally, for $W/W_{nom} = 1.0$ the horizontal epicyclic/roll mode roots drive the system unstable, while the roll/yaw mode root is invariant with respect to θ_V.

CHAPTER VI

CONCLUSION

6.1 PLT Model Development Summary

A classical aerospace tool for evaluating projectile dynamics and performance called Projectile Linear Theory has been extended to account for asymmetries caused by lifting surface aerodynamics. This was achieved in *Chapter* 2 by applying a series of assumptions and simplifications to a point-force lifting surface aerodynamic model, and then incorporating these linearized aerodynamic effects into the classical PLT system. The additional physics built into the extended PLT model greatly increases the coupling of the linearized dynamic equations of motion. These additional physics are primarily captured within the many extended theory coefficient expressions, summarized in *Appendix C*. For symmetric lifting surface configurations, however, substantial reduction in the model complexity was observed.

Several dynamic states were also observed to appear nonlinearly within the extended PLT coefficient of matrix $\mathbf{A}$ in Equation (67): total velocity–V_o, roll angle–ϕ_o, and roll rate–p_o. First, the PLT model was fully linearized by assuming that these states varied slowly in time, and can therefore be set to constant values of the initial (launch) conditions. This model was referred to as the LTI model. Using *linear systems theory*, stability of LTI models is easily quantified; however, the ability of LTI models to describe a projectile with aerodynamic asymmetries can fall short because the periodic affects of roll angle is lost when setting ϕ_o constant in the PLT coefficient matrix.

Additionally, it was observed that the projectile roll angle appears within the PLT matrix in periodic form (*i.e.* $\sin(\phi_o)$, $\cos(\phi_o)$). It is desirable to include roll periodic

to include the accuracy of the PLT model. If the extended assumption could be made that the projectile p_o was varying in a near linear fashion, then the roll angle could be varied as a linear function of time and proportional to p_o. This model was referred to as the LTP model. For LTP systems, a more advanced stability analysis technique called *Floquet theory* can then be used to quantify dynamic stability.

6.2 PLT Model Validation Summary

The findings of *Chapter* 4 show that the in-house 6DOF and PLT codes accurately predict projectile flight dynamic behavior. Additionally, the lifting surface model was used to represent a symmetric projectile configuration and successfully replicate simulation results for the equivalent projectile description using the body aerodynamic model of Section (2.4.3).

Next, symmetric projectile LTI models were generated for the classical and extended projectile linear theories. Simulation results were shown to be equivalent and able to closely approximate the nonlinear 6DOF model results for at least 1.0 (sec) of flight.

A similar set of simulations was then run using an asymmetric projectile, where it was seen that the LTP model in general outperformed the LTI model; however, both linear theories were only able to approximate the nonlinear 6DOF model over short periods of time (i.e. 0.2 (sec)). This was due to nonlinear state behavior in the roll rate for this configuration. This suggests that the ability of LTP and LTI models to accurately model asymmetric projectiles will need to be determined on a case-by-case basis.

Finally, stability analyses were conducted on both projectile configurations as roll rate was parametrically varied from 0.0 (rad/sec) $\leq p_o \leq$ 1000 (rad/sec). It was shown that for the symmetric projectile, both the LTI and LTP models generated the same stability results. For the asymmetric projectile, differences were observed

between the LTI and LTP stability results; however, the epicyclic modes and roll modes following similar behavior and the two models approached each other as roll rate increased.

6.3 Projectile Configuration Trade Studies Summary

Trade studies were conducted for a series of asymmetric projectile configurations. These included variation of fin parameters off symmetric projectile configurations and variation of quasi-linear states V_o and p_o for special configurations.

For the 4-finned baseline configuration, symmetric variation of F1 and F3 fin lengths (or equivalently planform areas) drove vertical epicyclic roots unstable for values of fin length less than $b/b_{nom} \approx 0.340$ in the subsonic case and $b/b_{nom} \approx 0.528$ in the supersonic case. It was shown that for the case where F1 and F3 fin length was $b \approx 0.0$ (ft) that instabilities could be "rolled-out", as the roll rate was increased above $p_o \approx 1.34$ (deg). It was also see that fast and slow epicyclic modes was appeared as the projectile became stable. For the case of asymmetric variation of two fin lengths, it was observed that epicyclic modes remained stable, while a roll/yaw mode appeared and drove the system to instability for fin length values $b/b_{nom} = 0.0$ in the subsonic case and $b/b_{nom} \leq 0.30$ in the supersonic case.

For the 3-finned baseline configuration, variation of the F1 fin length (or equivalently planform area) drove the roll/yaw mode root unstable for values of fin length less than $b/b_{nom} \approx 0.38$ in the subsonic case and $b/b_{nom} \approx 0.64$ in the supersonic case. It was shown that for the case of the V-tail projectile with $\theta_V = 120$ (deg) that instabilities could be "rolled-out". As p_o was increased above $p_o \approx 1.0$ (deg), the epicyclic mode roots were observed to become stable and form fast and slow mode behavior; however, for this configuration the system would become unstable for roll rate above $p_o \approx 70.8$ (deg).

For the hybrid aircraft/projectile baseline configuration, it was observed that increasing flight speed can cause horizontal epicyclic mode roots to become aperiodic and drive the system unstable at $Ma \approx 0.82$. Physically speaking, these results are intuitive, since it is known in aircraft stability that increasing flight speed can cause an unstable aerodynamic center location with respect to the stationline mass center. The affect of symmetrically reducing wing span length (or equivalently wing planform area) on stability was to drive the roll/yaw mode to become just unstable for wing span lengths less than $W/W_{nom} \approx 0.46$. Symmetrically reducing the fin lengths on the hybrid configuration quickly drives the horizontal epicyclic/roll modes to instability for fin lengths below $b/b_{nom} \approx 0.7114$. Changes in the hybrid configuration V-tail fin angle was observed to have no affect on the roll mode root, but the system becomes unstable for $\theta_V \approx 133.53$ (deg). The wing dihedral angle study yielded the interesting result that for large and positive values of Γ, stability could be conserved if an inverted V-tail was used. Finally, it was observed that the parameter space can have a highly nonlinear affect on stability root loci, and consideration must be taken to completely understand stability characteristics in a given area of the parameter space.

APPENDIX A

PROJECTILE DESCRIPTION

The Army-Navy Basic finner, or sometimes called the standard finner, was used as a testbed for this study. The figure below illustrates the relative configuration of the projectile. Table 22 summarizes the nominal projectile properties [12].

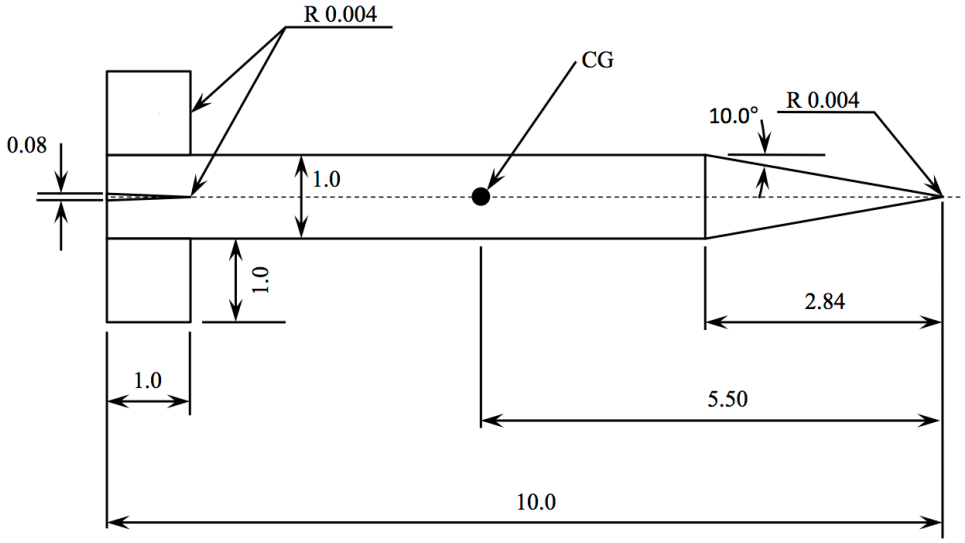

Figure 100: Dimensional Sketch-up of the Basic Finner projectile geometry. All dimensions are in calibers (1.0 caliber is equivalent to the projectile diameter).

Table 22: Summary Basic Finner projectile nominal properties.

D (mm)	m (g)	I_R (g−cm^2)	I_P (g−cm^2)	L (mm)	CG from nose (% /100)
30.0	1589.4	1924.07	98743.38	300	0.55

APPENDIX B

CLASSICAL PLT MODEL SUMMARY

B.1 Dynamic Equations of Motion

Recall the general form for the PLT dynamic equations of motion take on a quasi-linear form $\vec{x}' = [\mathbf{A}]\,\vec{x} + \{B\}$, where total velocity V and roll rate p are assumed to change slowly in several of the linearized coefficients C_{**}.

$$\begin{Bmatrix} V' \\ p' \\ \tilde{v}' \\ \tilde{w}' \\ \tilde{q}' \\ \tilde{r}' \end{Bmatrix} = \begin{bmatrix} C_{VV} & 0 & 0 & 0 & 0 & 0 \\ C_{pV} & C_{pp} & 0 & 0 & 0 & 0 \\ 0 & 0 & C_{\tilde{v}\tilde{v}} & 0 & 0 & C_{\tilde{v}\tilde{r}} \\ 0 & 0 & 0 & C_{\tilde{w}\tilde{w}} & C_{\tilde{w}\tilde{q}} & 0 \\ 0 & 0 & C_{\tilde{q}\tilde{v}} & C_{\tilde{q}\tilde{w}} & C_{\tilde{q}\tilde{q}} & C_{\tilde{q}\tilde{r}} \\ 0 & 0 & C_{\tilde{q}\tilde{v}} & C_{\tilde{r}\tilde{w}} & C_{\tilde{r}\tilde{q}} & C_{\tilde{r}\tilde{r}} \end{bmatrix} \cdot \begin{Bmatrix} V \\ p \\ \tilde{v} \\ \tilde{w} \\ \tilde{q} \\ \tilde{r} \end{Bmatrix} + \begin{Bmatrix} G_V \\ 0 \\ 0 \\ G_{\tilde{w}} \\ 0 \\ 0 \end{Bmatrix} \tag{85}$$

B.2 Classical PLT Coefficient Summary

The classical PLT matrix [**A**] is populated by the following coefficient expressions.

$$C'_{\mathrm{VV}} = -\frac{\pi\rho D^3 C_{\mathrm{X0}}}{8m} \tag{86}$$

$$C'_{\mathrm{pV}} = \frac{\pi\rho D^4 C_{\mathrm{LDD}}}{8I_R} \tag{87}$$

$$C'_{\mathrm{pp}} = \frac{\pi\rho D^5 C_{\mathrm{LP}}}{16I_R} \tag{88}$$

$$C'_{\tilde{v}\tilde{v}} = -\frac{\pi\rho D^3 C_{\mathrm{NA}}}{8m} \tag{89}$$

$$C'_{\tilde{v}\tilde{r}} = -D \tag{90}$$

$$C'_{\tilde{w}\tilde{w}} = -\frac{\pi\rho D^3 C_{\mathrm{NA}}}{8m} \tag{91}$$

$$C'_{\tilde{w}\tilde{q}} = D \tag{92}$$

$$C'_{\tilde{q}\tilde{v}} = -\frac{\pi\rho D^4 C_{\mathrm{YPA}} \Delta \mathrm{SL}_M}{16 I_P V_o} p_o \tag{93}$$

$$C'_{\tilde{q}\tilde{w}} = \frac{\pi\rho D^3 C_{\mathrm{NA}} \Delta \mathrm{SL}}{8 I_P} \tag{94}$$

$$C'_{\tilde{q}\tilde{q}} = \frac{\pi\rho D^5 C_{\mathrm{MQ}}}{16 I_P} \tag{95}$$

$$C'_{\tilde{q}\tilde{r}} = -\frac{D I_R}{V_o I_P} p_o \tag{96}$$

$$C'_{\tilde{r}\tilde{v}} = -\frac{\pi\rho D^3 C_{\mathrm{NA}} \Delta \mathrm{SL}}{8 I_P} \tag{97}$$

$$C'_{\tilde{r}\tilde{w}} = \frac{\pi\rho D^4 C_{\mathrm{YPA}} \Delta \mathrm{SL}_M}{16 I_P V_o} p_o \tag{98}$$

$$C'_{\tilde{r}\tilde{q}} = \frac{D I_R}{V_o I_P} p_o \tag{99}$$

$$C'_{\tilde{r}\tilde{r}} = \frac{\pi\rho D^5 C_{\mathrm{MQ}}}{16 I_P} \tag{100}$$

APPENDIX C

EXTENDED PLT MODEL SUMMARY

C.1 Linearized Lifting Surface Force/Moment Components

Recall that after applying the extended PLT assumptions to the lifting surface model, that the total generated aerodynamic force/moment take the following form.

- x-component of the total generated lifting surface aerodynamic force:

$$\begin{aligned}\tilde{X}'_C = m[&X'_V V + \left(X'_p + X'_{\text{pp}} p_o\right) p + \left(X'_{\tilde{v}} + X'_{\tilde{v}p} p_o\right) \tilde{v} \\ &+ \left(X'_{\tilde{w}} + X'_{\tilde{w}p} p_o\right) \tilde{w} + \left(X'_{\tilde{q}} + X'_{\tilde{q}p} p_o\right) \tilde{q} + \left(X'_{\tilde{r}} + X'_{\tilde{r}p} p_o\right) \tilde{r}]\end{aligned} \tag{101}$$

- y-component of the total generated lifting surface aerodynamic force:

$$\begin{aligned}\tilde{Y}'_C = m[&Y'_V V + \left(Y'_p + Y'_{\text{pp}} p_o\right) p + \left(Y'_{\tilde{v}} + Y'_{\tilde{v}p} p_o\right) \tilde{v} \\ &+ \left(Y'_{\tilde{w}} + Y'_{\tilde{w}p} p_o\right) \tilde{w} + \left(Y'_{\tilde{q}} + Y'_{\tilde{q}p} p_o\right) \tilde{q} + \left(Y'_{\tilde{r}} + Y'_{\tilde{r}p} p_o\right) \tilde{r}]\end{aligned} \tag{102}$$

- z-component of the total generated lifting surface aerodynamic force:

$$\begin{aligned}\tilde{Z}'_C = m[&Z'_V V + \left(Z'_p + Z'_{\text{pp}} p_o\right) p + \left(Z'_{\tilde{v}} + Z'_{\tilde{v}p} p_o\right) \tilde{v} \\ &+ \left(Z'_{\tilde{w}} + Z'_{\tilde{w}p} p_o\right) \tilde{w} + \left(Z'_{\tilde{q}} + Z'_{\tilde{q}p} p_o\right) \tilde{q} + \left(Z'_{\tilde{r}} + Z'_{\tilde{r}p} p_o\right) \tilde{r}]\end{aligned} \tag{103}$$

- x-component of the total generated lifting surface aerodynamic moment:

$$\begin{aligned}\tilde{L}'_C = I_R[&L'_V V + \left(L'_p + L'_{\text{pp}} p_o\right) p + \left(L'_{\tilde{v}} + L'_{\tilde{v}p} p_o\right) \tilde{v} \\ &+ \left(L'_{\tilde{w}} + L'_{\tilde{w}p} p_o\right) \tilde{w} + \left(L'_{\tilde{q}} + L'_{\tilde{q}p} p_o\right) \tilde{q} + \left(L'_{\tilde{r}} + L'_{\tilde{r}p} p_o\right) \tilde{r}]\end{aligned} \tag{104}$$

- y-component of the total generated lifting surface aerodynamic moment:

$$\begin{aligned}\tilde{M}'_C = I_P[&M'_V V + \left(M'_p + M'_{\text{pp}} p_o\right) p + \left(M'_{\tilde{v}} + M'_{\tilde{v}p} p_o\right) \tilde{v} \\ &+ \left(M'_{\tilde{w}} + M'_{\tilde{w}p} p_o\right) \tilde{w} + \left(M'_{\tilde{q}} + M'_{\tilde{q}p} p_o\right) \tilde{q} + \left(M'_{\tilde{r}} + M'_{\tilde{r}p} p_o\right) \tilde{r}]\end{aligned} \tag{105}$$

- z-component of the total generated lifting surface aerodynamic moment:

$$\begin{aligned}\tilde{N}'_C = I_P[&N'_V V + \left(N'_p + N'_{\text{pp}} p_o\right) p + \left(N'_{\tilde{v}} + N'_{\tilde{v}p} p_o\right) \tilde{v} \\ &+ \left(N'_{\tilde{w}} + N'_{\tilde{w}p} p_o\right) \tilde{w} + \left(N'_{\tilde{q}} + N'_{\tilde{q}p} p_o\right) \tilde{q} + \left(N'_{\tilde{r}} + N'_{\tilde{r}p} p_o\right) \tilde{r}]\end{aligned} \tag{106}$$

C.2 Dynamic Equations of Motion

Incorporating the quasi-linearized lifting-surface force/moment expressions into the classical PLT model, the elements of the matrix [**A**] become increasingly more populated. Total velocity V, roll rate p, and projectile roll angle ϕ are assumed to change slowly in several of the linearized coefficients.

$$A = \left[\begin{array}{c|c|c|c|c|c} \tilde{X}'_V + C'_{VV} & \tilde{X}'_p + \tilde{X}'_{pp} p_o & \tilde{X}'_{\tilde{v}} + \tilde{X}'_{\tilde{v}p} p_o & \tilde{X}'_{\tilde{w}} + \tilde{X}'_{\tilde{w}p} p_o & \tilde{X}'_{\tilde{q}} + \tilde{X}'_{\tilde{q}p} p_o & \tilde{X}'_{\tilde{r}} + \tilde{X}'_{\tilde{r}p} p_o \\ \hline \tilde{L}'_V + C'_{pV} & \tilde{L}'_p + \tilde{L}'_{pp} p_o + C'_{pp} & \tilde{L}'_{\tilde{v}} + \tilde{L}'_{\tilde{v}p} p_o & \tilde{L}'_{\tilde{w}} + \tilde{L}'_{\tilde{w}p} p_o & \tilde{L}'_{\tilde{q}} + \tilde{L}'_{\tilde{q}p} p_o & \tilde{L}'_{\tilde{r}} + \tilde{L}'_{\tilde{r}p} p_o \\ \hline \tilde{Y}'_V & \tilde{Y}'_p + \tilde{Y}'_{pp} p_o & \tilde{Y}'_{\tilde{v}} + \tilde{Y}'_{\tilde{v}p} p_o + C'_{\tilde{v}\tilde{v}} & \tilde{Y}'_{\tilde{w}} + \tilde{Y}'_{\tilde{w}p} p_o & \tilde{Y}'_{\tilde{q}} + \tilde{Y}'_{\tilde{q}p} p_o & \tilde{Y}'_{\tilde{r}} + \tilde{Y}'_{\tilde{r}p} p_o + C'_{\tilde{v}\tilde{r}} \\ \hline \tilde{Z}'_V & \tilde{Z}'_p + \tilde{Z}'_{pp} p_o & \tilde{Z}'_{\tilde{v}} + \tilde{Z}'_{\tilde{v}p} p_o & \tilde{Z}'_{\tilde{w}} + \tilde{Z}'_{\tilde{w}p} p_o + C'_{\tilde{w}\tilde{w}} & \tilde{Z}'_{\tilde{q}} + \tilde{Z}'_{\tilde{q}p} p_o + C'_{\tilde{w}\tilde{q}} & \tilde{Z}'_{\tilde{r}} + \tilde{Z}'_{\tilde{r}p} p_o \\ \hline \tilde{M}'_V & \tilde{M}'_p + \tilde{M}'_{pp} p_o & \tilde{M}'_{\tilde{v}} + \tilde{M}'_{\tilde{v}p} p_o + C'_{\tilde{q}\tilde{v}} & \tilde{M}'_{\tilde{w}} + \tilde{M}'_{\tilde{w}p} + C'_{\tilde{q}\tilde{w}} & \tilde{M}'_{\tilde{q}} + \tilde{M}'_{\tilde{q}p} p_o + C'_{\tilde{q}\tilde{q}} & \tilde{M}'_{\tilde{r}} + \tilde{M}'_{\tilde{r}p} p_o + C'_{\tilde{q}\tilde{r}} \\ \hline \tilde{N}'_V & \tilde{N}'_p + \tilde{N}'_{pp} p_o & \tilde{N}'_{\tilde{v}} + \tilde{N}'_{\tilde{v}p} p_o + C'_{\tilde{q}\tilde{v}} & \tilde{N}'_{\tilde{w}} + \tilde{N}'_{\tilde{w}p} + C'_{\tilde{r}\tilde{w}} & \tilde{N}'_{\tilde{q}} + \tilde{N}'_{\tilde{q}p} p_o + C'_{\tilde{r}\tilde{q}} & \tilde{N}'_{\tilde{r}} + \tilde{N}'_{\tilde{r}p} p_o + C'_{\tilde{r}\tilde{r}} \end{array}\right] \tag{107}$$

C.3 Extended PLT Summary

The extended PLT dynamic matrix [**A**] is populated by the following coefficient expressions.

C.3.1 Lifting Surface Force X-Component Summary

$$X'_V = -\frac{\pi\rho D^3 C_{D_o}}{8m} n \tag{108}$$

$$X'_p = \frac{\pi\rho D^3 C_{L_\alpha}}{8m} \sum_{i=1}^{n} \delta_{C_i} (\cos[\phi_{C_i}]\Delta\mathrm{BL}_{C_i} + \sin[\phi_{C_i}]\Delta\mathrm{WL}_{C_i}) \tag{109}$$

$$X'_{\mathrm{pp}} = \frac{\pi\rho D^3 C_{L_\alpha}}{8mV} \sum_{i=1}^{n} (\cos[\phi_{C_i}]\Delta\mathrm{BL}_{C_i} + \sin[\phi_{C_i}]\Delta\mathrm{WL}_{C_i})^2 \tag{110}$$

$$X'_{\tilde{v}} = -\frac{\pi\rho D^3 C_{L_\alpha}}{8m} \sum_{i=1}^{n} \sin[\phi + \phi_{C_i}]\delta_{C_i} \tag{111}$$

$$X'_{\tilde{v}p} = -\frac{\pi\rho D^3 C_{L_\alpha}}{4mV} \sum_{i=1}^{n} \sin[\phi + \phi_{C_i}](\cos[\phi_{C_i}]\Delta\mathrm{BL}_{C_i} + \sin[\phi_{C_i}]\Delta\mathrm{WL}_{C_i}) \tag{112}$$

$$X'_{\tilde{w}} = \frac{\pi\rho D^3 C_{L_\alpha}}{8m} \sum_{i=1}^{n} \cos[\phi + \phi_{C_i}]\delta_{C_i} \tag{113}$$

$$X'_{\tilde{w}p} = \frac{\pi\rho D^3 C_{L_\alpha}}{4mV} \sum_{i=1}^{n} \cos[\phi + \phi_{C_i}](\cos[\phi_{C_i}]\Delta\mathrm{BL}_{C_i} + \sin[\phi_{C_i}]\Delta\mathrm{WL}_{C_i}) \tag{114}$$

$$X'_{\tilde{q}} = -\frac{\pi\rho D^3}{8m} \sum_{i=1}^{n} (\cos[\phi + \phi_{C_i}]C_{L_\alpha}\delta_{C_i}\Delta\mathrm{SL}_{C_i} + C_{D_o}(\sin[\phi]\Delta\mathrm{BL}_{C_i} + \cos[\phi]\Delta\mathrm{WL}_{C_i})) \tag{115}$$

$$X'_{\tilde{q}p} = -\frac{\pi\rho D^3}{4mV} \sum_{i=1}^{n} \cos[\phi + \phi_{C_i}]C_{L_\alpha}\Delta\mathrm{SL}_{C_i}(\cos[\phi_{C_i}]\Delta\mathrm{BL}_{C_i} + \sin[\phi_{C_i}]\Delta\mathrm{WL}_{C_i}) \tag{116}$$

$$X'_{\tilde{r}} = -\frac{\pi\rho D^3}{8m}\sum_{i=1}^{n}(\sin[\phi+\phi_{C_i}]\delta_{C_i}C_{L_\alpha}\Delta\mathrm{SL}_{C_i} - C_{D_o}(\cos[\phi]\Delta\mathrm{BL}_{C_i} - \sin[\phi]\Delta\mathrm{WL}_{C_i})) \tag{117}$$

$$X'_{\tilde{r}p} = -\frac{\pi\rho D^3 C_{L_\alpha}}{4mV}\sum_{i=1}^{n}\sin[\phi+\phi_{C_i}]\Delta\mathrm{SL}_{C_i}(\cos[\phi_{C_i}]\Delta\mathrm{BL}_{C_i} + \sin[\phi_{C_i}]\Delta\mathrm{WL}_{C_i}) \tag{118}$$

C.3.2 Lifting Surface Moment X-Component Summary

$$L'_p = -\frac{\pi\rho D^3(C_{D_o}+C_{L_\alpha})}{8I_R}\sum_{i=1}^{n}(\cos[\phi_{C_i}]\Delta\mathrm{BL}_{C_i} + \sin[\phi_{C_i}]\Delta\mathrm{WL}_{C_i})^2 \tag{119}$$

$$L'_{\mathrm{pp}} = 0 \tag{120}$$

$$L'_{\tilde{v}} = \frac{\pi\rho D^3(C_{D_o}+C_{L_\alpha})}{8I_R}\sum_{i=1}^{n}\sin[\phi+\phi_{C_i}](\cos[\phi_{C_i}]\Delta\mathrm{BL}_{C_i} + \sin[\phi_{C_i}]\Delta\mathrm{WL}_{C_i}) \tag{121}$$

$$L'_{\tilde{v}p} = 0 \tag{122}$$

$$L'_{\tilde{w}} = -\frac{\pi\rho D^3(C_{D_o}+C_{L_\alpha})}{8I_R}\sum_{i=1}^{n}\cos[\phi+\phi_{C_i}](\cos[\phi_{C_i}]\Delta\mathrm{BL}_{C_i} + \sin[\phi_{C_i}]\Delta\mathrm{WL}_{C_i}) \tag{123}$$

$$L'_{\tilde{w}p} = 0 \tag{124}$$

$$\begin{aligned} L'_{\tilde{q}} =& \frac{\pi\rho D^3}{8I_R}\sum_{i=1}^{n}(\cos[\phi_{C_i}]\Delta\mathrm{BL}_{C_i} + \sin[\phi_{C_i}]\Delta\mathrm{WL}_{C_i})((C_{D_o}+C_{L_\alpha})\cos[\phi+\phi_{C_i}]\Delta\mathrm{SL}_{C_i} \\ & - C_{L_\alpha}\delta_{C_i}(\sin[\phi]\Delta\mathrm{BL}_{C_i} + \cos[\phi]\Delta\mathrm{WL}_{C_i})) \end{aligned} \tag{125}$$

$$L'_{\tilde{q}p} = -\frac{\pi\rho D^3 C_{L_\alpha}}{8 I_R V}\sum_{i=1}^{n}(\sin[\phi]\Delta\mathrm{BL}_{C_i}+\cos[\phi]\Delta\mathrm{WL}_{C_i})(\cos[\phi_{C_i}]\Delta\mathrm{BL}_{C_i}+\sin[\phi_{C_i}]\Delta\mathrm{WL}_{C_i})^2 \tag{126}$$

$$\begin{aligned} L'_{\tilde{r}} =& \frac{\pi\rho D^3}{8 I_R}\sum_{i=1}^{n}(\cos[\phi_{C_i}]\Delta\mathrm{BL}_{C_i} + \sin[\phi_{C_i}]\Delta\mathrm{WL}_{C_i})((C_{D_o} + C_{L_\alpha})\sin[\phi + \phi_{C_i}]\Delta\mathrm{SL}_{C_i} \\ &+ C_{L_\alpha}\delta_{C_i}(\cos[\phi]\Delta\mathrm{BL}_{C_i} - \sin[\phi]\Delta\mathrm{WL}_{C_i})) \end{aligned} \tag{127}$$

$$L'_{\tilde{r}p} = \frac{\pi\rho D^3 C_{L_\alpha}}{8 I_R V}\sum_{i=1}^{n}(\cos[\phi]\Delta\mathrm{BL}_{C_i} - \sin[\phi]\Delta\mathrm{WL}_{C_i})(\cos[\phi_{C_i}]\Delta\mathrm{BL}_{C_i} + \sin[\phi_{C_i}]\Delta\mathrm{WL}_{C_i})^2 \tag{128}$$

C.3.3 Lifting Surface Force Y-Component Summary

$$Y'_V = \frac{\pi\rho D^3 C_{L_\alpha}}{8m}\sum_{i=1}^{n}\sin[\phi + \phi_{C_i}]\delta_{C_i} \tag{129}$$

$$Y'_p = \frac{\pi\rho D^3 (C_{D_o} + C_{L_\alpha})}{8m}\sum_{i=1}^{n}\sin[\phi + \phi_{C_i}](\cos[\phi_{C_i}]\Delta\mathrm{BL}_{C_i} + \sin[\phi_{C_i}]\Delta\mathrm{WL}_{C_i}) \tag{130}$$

$$Y'_{\mathrm{pp}} = 0 \tag{131}$$

$$Y'_{\tilde{v}} = -\frac{\pi\rho D^3 (C_{D_o} + C_{L_\alpha})}{8m}\sum_{i=1}^{n}\sin[\phi + \phi_{C_i}]^2 \tag{132}$$

$$Y'_{\tilde{v}p} = 0 \tag{133}$$

$$Y'_{\tilde{w}} = \frac{\pi\rho D^3 (C_{D_o} + C_{L_\alpha})}{16m}\sum_{i=1}^{n}\sin[2(\phi + \phi_{C_i})] \tag{134}$$

$$Y'_{\tilde{w}p} = 0 \tag{135}$$

$$\begin{aligned} Y'_{\tilde{q}} = &- \frac{\pi\rho D^3}{8m}\sum_{i=1}^{n}\sin[\phi+\phi_{C_i}]((C_{D_o}+C_{L_\alpha})\cos[\phi+\phi_{C_i}]\Delta\mathrm{SL}_{C_i} \\ &- C_{L_\alpha}\delta_{C_i}(\sin[\phi]\Delta\mathrm{BL}_{C_i}+\cos[\phi]\Delta\mathrm{WL}_{C_i})) \end{aligned} \tag{136}$$

$$\begin{aligned} Y'_{\tilde{q}p} = &\frac{\pi\rho D^3 C_{L_\alpha}}{8mV}\sum_{i=1}^{n}\sin[\phi+\phi_{C_i}](\sin[\phi]\Delta\mathrm{BL}_{C_i}+\cos[\phi]\Delta\mathrm{WL}_{C_i}) \\ &\cdot(\cos[\phi_{C_i}]\Delta\mathrm{BL}_{C_i}+\sin[\phi_{C_i}]\Delta\mathrm{WL}_{C_i}) \end{aligned} \tag{137}$$

$$\begin{aligned} Y'_{\tilde{r}} = &- \frac{\pi\rho D^3}{8m}\sum_{i=1}^{n}\sin[\phi+\phi_{C_i}]((C_{D_o}+C_{L_\alpha})\sin[\phi+\phi_{C_i}]\Delta\mathrm{SL}_{C_i} \\ &+ C_{L_\alpha}\delta_{C_i}(\cos[\phi]\Delta\mathrm{BL}_{C_i}-\sin[\phi]\Delta\mathrm{WL}_{C_i})) \end{aligned} \tag{138}$$

$$\begin{aligned} Y'_{\tilde{r}p} = &- \frac{\pi\rho D^3 C_{L_\alpha}}{8mV}\sum_{i=1}^{n}\sin[\phi+\phi_{C_i}](\cos[\phi]\Delta\mathrm{BL}_{C_i}-\sin[\phi]\Delta\mathrm{WL}_{C_i}) \\ &\cdot(\cos[\phi_{C_i}]\Delta\mathrm{BL}_{C_i}+\sin[\phi_{C_i}]\Delta\mathrm{WL}_{C_i}) \end{aligned} \tag{139}$$

C.3.4 Lifting Surface Force Z-Component Summary

$$Z'_V = -\frac{\pi\rho D^3}{8m}\sum_{i=1}^{n}\cos[\phi+\phi_{C_i}]C_{L_\alpha}\delta_{C_i} \tag{140}$$

$$Z'_p = -\frac{\pi\rho D^3(C_{D_o}+C_{L_\alpha})}{8m}\sum_{i=1}^{n}\cos[\phi+\phi_{C_i}](\cos[\phi_{C_i}]\Delta\mathrm{BL}_{C_i}+\sin[\phi_{C_i}]\Delta\mathrm{WL}_{C_i}) \tag{141}$$

$$Z'_{\mathrm{pp}} = 0 \tag{142}$$

$$Z'_{\tilde{v}} = \frac{\pi\rho D^3(C_{D_o}+C_{L_\alpha})}{16m}\sum_{i=1}^{n}\sin[2(\phi+\phi_{C_i})] \tag{143}$$

$$Z'_{\tilde{v}p} = 0 \tag{144}$$

$$Z'_{\tilde{w}} = -\frac{\pi\rho D^3(C_{D_o} + C_{L_\alpha})}{8m}\sum_{i=1}^{n}\cos[\phi + \phi_{C_i}]^2 \tag{145}$$

$$Z'_{\tilde{w}p} = 0 \tag{146}$$

$$\begin{aligned} Z'_{\tilde{q}} =& \frac{\pi\rho D^3}{8m}\sum_{i=1}^{n}\cos[\phi + \phi_{C_i}]((C_{D_o} + C_{L_\alpha})\cos[\phi + \phi_{C_i}]\Delta\mathrm{SL}_{C_i} \\ & - C_{L_\alpha}\delta_{C_i}(\sin[\phi]\Delta\mathrm{BL}_{C_i} + \cos[\phi]\Delta\mathrm{WL}_{C_i})) \end{aligned} \tag{147}$$

$$\begin{aligned} Z'_{\tilde{q}p} =& -\frac{\pi\rho D^3 C_{L_\alpha}}{8mV}\sum_{i=1}^{n}\cos[\phi + \phi_{C_i}](\sin[\phi]\Delta\mathrm{BL}_{C_i} + \cos[\phi]\Delta\mathrm{WL}_{C_i}) \\ & \cdot(\cos[\phi_{C_i}]\Delta\mathrm{BL}_{C_i} + \sin[\phi_{C_i}]\Delta\mathrm{WL}_{C_i}) \end{aligned} \tag{148}$$

$$\begin{aligned} Z'_{\tilde{r}} =& \frac{\pi\rho D^3}{8m}\sum_{i=1}^{n}\cos[\phi + \phi_{C_i}]((C_{D_o} + C_{L_\alpha})\sin[\phi + \phi_{C_i}]\Delta\mathrm{SL}_{C_i} \\ & + C_{L_\alpha}\delta_{C_i}(\cos[\phi]\Delta\mathrm{BL}_{C_i} - \sin[\phi]\Delta\mathrm{WL}_{C_i})) \end{aligned} \tag{149}$$

$$\begin{aligned} Z'_{\tilde{r}p} =& \frac{\pi\rho D^3 C_{L_\alpha}}{8mV}\sum_{i=1}^{n}\cos[\phi + \phi_{C_i}](\cos[\phi]\Delta\mathrm{BL}_{C_i} - \sin[\phi]\Delta\mathrm{WL}_{C_i}) \\ & \cdot(\cos[\phi_{C_i}]\Delta\mathrm{BL}_{C_i} + \sin[\phi_{C_i}]\Delta\mathrm{WL}_{C_i}) \end{aligned} \tag{150}$$

C.3.5 Lifting Surface Moment Y-Component Summary

$$M'_V = -\frac{\pi\rho D^3}{8I_P}\sum_{i=1}^{n}(-\cos[\phi + \phi_{C_i}]C_{L_\alpha}\delta_{C_i}\Delta\mathrm{SL}_{C_i} + C_{D_o}(\sin[\phi]\Delta\mathrm{BL}_{C_i} + \cos[\phi]\Delta\mathrm{WL}_{C_i})) \tag{151}$$

$$M'_p = \frac{\pi\rho D^3}{8I_P}\sum_{i=1}^{n}(\cos[\phi_{C_i}]\Delta\mathrm{BL}_{C_i} + \sin[\phi_{C_i}]\Delta\mathrm{WL}_{C_i})((C_{D_o} + C_{L_\alpha})\cos[\phi + \phi_{C_i}]\Delta\mathrm{SL}_{C_i} + C_{L_\alpha}\delta_{C_i}(\sin[\phi]\Delta\mathrm{BL}_{C_i} + \cos[\phi]\Delta\mathrm{WL}_{C_i})) \tag{152}$$

$$M'_{\mathrm{pp}} = \frac{\pi\rho D^3 C_{L_\alpha}}{8I_P V}\sum_{i=1}^{n}(\sin[\phi]\Delta\mathrm{BL}_{C_i} + \cos[\phi]\Delta\mathrm{WL}_{C_i})(\cos[\phi_{C_i}]\Delta\mathrm{BL}_{C_i} + \sin[\phi_{C_i}]\Delta\mathrm{WL}_{C_i})^2 \tag{153}$$

$$M'_{\tilde{v}} = -\frac{\pi\rho D^3}{8I_P}\sum_{i=1}^{n}\sin[\phi + \phi_{C_i}]((C_{D_o} + C_{L_\alpha})\cos[\phi + \phi_{C_i}]\Delta\mathrm{SL}_{C_i} + C_{L_\alpha}\delta_{C_i}(\sin[\phi]\Delta\mathrm{BL}_{C_i} + \cos[\phi]\Delta\mathrm{WL}_{C_i})) \tag{154}$$

$$M'_{\tilde{v}p} = -\frac{\pi\rho D^3 C_{L_\alpha}}{4I_P V}\sum_{i=1}^{n}\sin[\phi + \phi_{C_i}](\sin[\phi]\Delta\mathrm{BL}_{C_i} + \cos[\phi]\Delta\mathrm{WL}_{C_i}) \cdot (\cos[\phi_{C_i}]\Delta\mathrm{BL}_{C_i} + \sin[\phi_{C_i}]\Delta\mathrm{WL}_{C_i}) \tag{155}$$

$$M'_{\tilde{w}} = \frac{\pi\rho D^3}{8I_P}\sum_{i=1}^{n}\cos[\phi + \phi_{C_i}]((C_{D_o} + C_{L_\alpha})\cos[\phi + \phi_{C_i}]\Delta\mathrm{SL}_{C_i} + C_{L_\alpha}\delta_{C_i}(\sin[\phi]\Delta\mathrm{BL}_{C_i} + \cos[\phi]\Delta\mathrm{WL}_{C_i})) \tag{156}$$

$$M'_{\tilde{w}p} = \frac{\pi\rho D^3 C_{L_\alpha}}{4I_P V}\sum_{i=1}^{n}\cos[\phi + \phi_{C_i}]\ (\sin[\phi]\Delta\mathrm{BL}_{C_i} + \cos[\phi]\Delta\mathrm{WL}_{C_i}) \cdot (\cos[\phi_{C_i}]\Delta\mathrm{BL}_{C_i} + \sin[\phi_{C_i}]\Delta\mathrm{WL}_{C_i}) \tag{157}$$

$$M'_{\tilde{q}} = -\frac{\pi\rho D^3}{8I_P}\sum_{i=1}^{n}((C_{D_o} + C_{L_\alpha})\cos[\phi + \phi_{C_i}]^2\Delta\mathrm{SL}_{C_i}^2 + C_{D_o}(\sin[\phi]\Delta\mathrm{BL}_{C_i} + \cos[\phi]\Delta\mathrm{WL}_{C_i})^2) \tag{158}$$

$$M'_{\tilde{q}p} = -\frac{\pi\rho D^3 C_{L_\alpha}}{8 I_P V}\sum_{i=1}^{n}\cos[\phi+\phi_{C_i}]\Delta\mathrm{SL}_{C_i}(\sin[\phi]\Delta\mathrm{BL}_{C_i}+\cos[\phi]\Delta\mathrm{WL}_{C_i}) \cdot(\cos[\phi_{C_i}]\Delta\mathrm{BL}_{C_i}+\sin[\phi_{C_i}]\Delta\mathrm{WL}_{C_i}) \tag{159}$$

$$M'_{\tilde{r}} = -\frac{\pi\rho D^3}{16 I_P}\sum_{i=1}^{n}(C_{L_\alpha}\Delta\mathrm{SL}_{C_i}(\sin[2(\phi+\phi_{C_i})]\Delta\mathrm{SL}_{C_i}+2\delta_{C_i}(\cos[\phi_{C_i}]\Delta\mathrm{BL}_{C_i}+\sin[\phi_{C_i}]\Delta\mathrm{WL}_{C_i})) + C_{D_o}(\sin[2(\phi+\phi_{C_i})]\Delta\mathrm{SL}_{C_i}^2-2\cos[2\phi]\Delta\mathrm{BL}_{C_i}\Delta\mathrm{WL}_{C_i}+\sin[2\phi](-\Delta\mathrm{BL}_{C_i}^2+\Delta\mathrm{WL}_{C_i}^2))) \tag{160}$$

$$M'_{\tilde{r}p} = -\frac{\pi\rho D^3 C_{L_\alpha}}{16 I_P V}\sum_{i=1}^{n}\Delta\mathrm{SL}_{C_i}(-\cos[\phi_{C_i}](-3\cos[\phi_{C_i}]+\cos[2\phi+\phi_{C_i}])\Delta\mathrm{BL}_{C_i}^2 + (\sin[2\phi]+3\sin[2\phi_{C_i}])\Delta\mathrm{BL}_{C_i}\Delta\mathrm{WL}_{C_i}+\sin[\phi_{C_i}](3\sin[\phi_{C_i}]+\sin[2\phi+\phi_{C_i}])\Delta\mathrm{WL}_{C_i}^2) \tag{161}$$

C.3.6 Lifting Surface Moment Z-Component Summary

$$N'_V = \frac{\pi\rho D^3}{8 I_P}\sum_{i=1}^{n}(\sin[\phi+\phi_{C_i}]C_{L_\alpha}\delta_{C_i}\Delta\mathrm{SL}_{C_i}+C_{D_o}(\cos[\phi]\Delta\mathrm{BL}_{C_i}-\sin[\phi]\Delta\mathrm{WL}_{C_i})) \tag{162}$$

$$N'_p = \frac{\pi\rho D^3}{8 I_P}\sum_{i=1}^{n}(\cos[\phi_{C_i}]\Delta\mathrm{BL}_{C_i}+\sin[\phi_{C_i}]\Delta\mathrm{WL}_{C_i})((C_{D_o}+C_{L_\alpha})\sin[\phi+\phi_{C_i}]\Delta\mathrm{SL}_{C_i} - C_{L_\alpha}\delta_{C_i}(\cos[\phi]\Delta\mathrm{BL}_{C_i}-\sin[\phi]\Delta\mathrm{WL}_{C_i})) \tag{163}$$

$$N'_{\mathrm{pp}} = -\frac{\pi\rho D^3 C_{L_\alpha}}{8 I_P V}\sum_{i=1}^{n}(\cos[\phi]\Delta\mathrm{BL}_{C_i}-\sin[\phi]\Delta\mathrm{WL}_{C_i})(\cos[\phi_{C_i}]\Delta\mathrm{BL}_{C_i}+\sin[\phi_{C_i}]\Delta\mathrm{WL}_{C_i})^2 \tag{164}$$

$$N'_{\tilde{v}} = -\frac{\pi\rho D^3}{8 I_P}\sum_{i=1}^{n}\sin[\phi+\phi_{C_i}]((C_{D_o}+C_{L_\alpha})\sin[\phi+\phi_{C_i}]\Delta\mathrm{SL}_{C_i} - C_{L_\alpha}\delta_{C_i}(\cos[\phi]\Delta\mathrm{BL}_{C_i}-\sin[\phi]\Delta\mathrm{WL}_{C_i})) \tag{165}$$

$$N'_{\tilde{v}p} = \frac{\pi\rho D^3 C_{L_\alpha}}{4 I_P V} \sum_{i=1}^{n} \sin[\phi + \phi_{C_i}](\cos[\phi]\Delta\mathrm{BL}_{C_i} - \sin[\phi]\Delta\mathrm{WL}_{C_i}) \cdot (\cos[\phi_{C_i}]\Delta\mathrm{BL}_{C_i} + \sin[\phi_{C_i}]\Delta\mathrm{WL}_{C_i}) \tag{166}$$

$$N'_{\tilde{w}} = \frac{\pi\rho D^3}{8 I_P} \sum_{i=1}^{n} \cos[\phi + \phi_{C_i}]((C_{D_o} + C_{L_\alpha})\sin[\phi + \phi_{C_i}]\Delta\mathrm{SL}_{C_i} - C_{L_\alpha}\delta_{C_i}(\cos[\phi]\Delta\mathrm{BL}_{C_i} - \sin[\phi]\Delta\mathrm{WL}_{C_i})) \tag{167}$$

$$N'_{\tilde{w}p} = -\frac{\pi\rho D^3 C_{L_\alpha}}{4 I_P V} \sum_{i=1}^{n} \cos[\phi + \phi_{C_i}](\cos[\phi]\Delta\mathrm{BL}_{C_i} - \sin[\phi]\Delta\mathrm{WL}_{C_i}) \cdot (\cos[\phi_{C_i}]\Delta\mathrm{BL}_{C_i} + \sin[\phi_{C_i}]\Delta\mathrm{WL}_{C_i}) \tag{168}$$

$$N'_{\tilde{q}} = \frac{D^3\pi\rho}{16 I_P} \sum_{i=1}^{n} (C_{L_\alpha}\Delta\mathrm{SL}_{C_i}(-\sin[2(\phi + \phi_{C_i})]\Delta\mathrm{SL}_{C_i} + 2\delta_{C_i}(\cos[\phi_{C_i}]\Delta\mathrm{BL}_{C_i} + \sin[\phi_{C_i}]\Delta\mathrm{WL}_{C_i})) + C_{D_o}(-\sin[2(\phi + \phi_{C_i})]\Delta\mathrm{SL}_{C_i}^2 + 2\cos[2\phi]\Delta\mathrm{BL}_{C_i}\Delta\mathrm{WL}_{C_i} + \sin[2\phi](\Delta\mathrm{BL}_{C_i}^2 - \Delta\mathrm{WL}_{C_i}^2))) \tag{169}$$

$$N'_{\tilde{q}p} = \frac{\pi\rho D^3 C_{L_\alpha}}{16 I_P V} \sum_{i=1}^{n} \Delta\mathrm{SL}_{C_i}(\cos[\phi_{C_i}](3\cos[\phi_{C_i}] + \cos[2\phi + \phi_{C_i}])\Delta\mathrm{BL}_{C_i}^2 - (\sin[2\phi] - 3\sin[2\phi_{C_i}])\Delta\mathrm{BL}_{C_i}\Delta\mathrm{WL}_{C_i} - \sin[\phi_{C_i}](-3\sin[\phi_{C_i}] + \sin[2\phi + \phi_{C_i}])\Delta\mathrm{WL}_{C_i}^2) \tag{170}$$

$$N'_{\tilde{r}} = -\frac{\pi\rho D^3}{8 I_P} \sum_{i=1}^{n} ((C_{D_o} + C_{L_\alpha})\sin[\phi + \phi_{C_i}]^2\Delta\mathrm{SL}_{C_i}^2 + C_{D_o}(\cos[\phi]\Delta\mathrm{BL}_{C_i} - \sin[\phi]\Delta\mathrm{WL}_{C_i})^2) \tag{171}$$

$$N'_{\tilde{r}p} = \frac{\pi\rho D^3 C_{L_\alpha}}{8 I_P V} \sum_{i=1}^{n} \sin[\phi + \phi_{C_i}]\ \Delta\mathrm{SL}_{C_i}(\cos[\phi]\Delta\mathrm{BL}_{C_i} - \sin[\phi]\Delta\mathrm{WL}_{C_i}) \cdot (\cos[\phi_{C_i}]\Delta\mathrm{BL}_{C_i} + \sin[\phi_{C_i}]\Delta\mathrm{WL}_{C_i}) \tag{172}$$

APPENDIX D

SUMMARY OF SEPARATING BASIC FINNER AERODYNAMIC MODELS

Using an industry standard aero-prediction software Prodas [1], decomposition of symmetric projectile aerodynamics is accomplished according to the models discussed in section 2.4.3. According to the Prodas User's Manual, decomposition of the Army-Navy finner aerodynamic coefficients can be expressed by the following:

- The total projectile axial force coefficient C_{X0}, found in Equation (24), can be broken down into contributions from the 4 fins $C_{X0_{4F}}$ and the cylindrically shaped projectile body C_{X0_B}.

$$C_{X0} = C_{X0_B} + C_{X0_{4F}} \tag{173}$$

  The axial force coefficient for a single fin $C_{X0_{1F}}$ can be found by taking a quarter of $C_{X0_{4F}}$.

$$C_{X0_{1F}} = \frac{1}{4} C_{X0_{4F}} \tag{174}$$

- The total projectile normal force coefficient C_{N_α}, found in Equation (24), can be broken down into contributions of an in-plain 2-fin set $C_{N\alpha_{2F}}$ and the cylindrically shaped projectile body $C_{N\alpha_B}$.

$$C_{N\alpha} = C_{N\alpha_B} + C_{N\alpha_{2F}} \tag{175}$$

  The normal force coefficient for a single fin $C_{N\alpha_{1F}}$ can be found by taking half of $C_{N\alpha_{2F}}$.

$$C_{N\alpha_{1F}} = \frac{1}{2} C_{N\alpha_{2F}} \tag{176}$$

- The single fin lift and drag coefficients, found in Equation (39) can be approximated for small angles of attack, according to McCoy [23] by:

$$C_{L\alpha_{1F}} \approx C_{N\alpha_{1F}} + C_{X0_{1F}} \tag{177}$$

$$C_{Do_{1F}} \approx C_{X0_{1F}} \tag{178}$$

In order to ensure that the aerodynamic moments are equivalent between the two models, position vector components for the i^{th} lifting surface computation point must be calculated. This can be done by a moment balance equation about the projectile mass center. Figure 101 illustrates aerodynamic COP points for both models.

Using aerodynamic theory previously discussed, Equation (179) summarizes the total aerodynamic moment for the total aero case, and Equation (180) shows and equivalent expression for the separated aero case.

$$\mathbb{C}_B\left(\vec{M}_A\right) = \mathbb{S}_B\left(\vec{r}_{\oplus\rightarrow COP}\right) \cdot \mathbb{C}_B\left(\vec{F}_A\right) \tag{179}$$

$$\mathbb{C}_B\left(\vec{M}_A\right) = \mathbb{S}_B\left(\vec{r}_{\oplus\rightarrow COP_B}\right) \cdot \mathbb{C}_B\left(\vec{F}_B\right) + \sum_{i=1}^{4} \mathbb{S}_B\left(\vec{r}_{\oplus\rightarrow COP_{F_i}}\right) \cdot \mathbb{C}_B\left(\vec{F}_{4F}\right) \tag{180}$$

For convenience, the i^{th} lifting surface computation points will be described by two lengths, transverse location e_i and axial location f_i, which is measured from the butt of the projectile. Expanding out the moment balance expressions yields identical expressions in the transverse planes and a moderately complicated expression in the roll plane; however, assuming from linear theory that the lifting surface angles of attack are small allows for the following approximation.

$$\alpha_{F_i} = -\frac{p\ e_i}{V} + \delta_{F_i} \tag{181}$$

The final expression for the transverse location e_i with $\delta_{F_i} = 0.00$ (deg) was found to be:

$$e_i = D\sqrt{-\frac{C_{lp}}{8C_{L_\alpha}}} \tag{182}$$

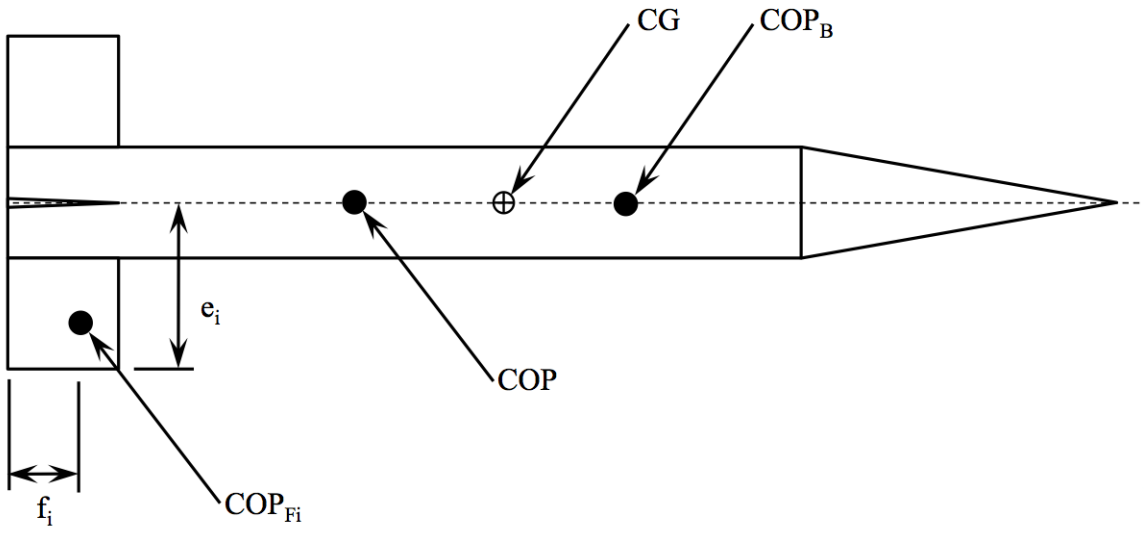

Figure 101: Dimensional Sketch-up of the Basic Finner projectile geometry that illustrates the different aerodynamic computation points used by the two models.

From Prodas, the axial location f_i can easily be found, but the stationline location of the new cylindrical body aero location SL_{COP_B} can be found by:

$$SL_{COP_B} = \frac{C_{N\alpha}}{C_{N\alpha_B}} \cdot SL_{COP} - \frac{C_{N\alpha_{2F}}}{C_{N\alpha_B}} \cdot f_i \tag{183}$$

Table 23 summarizes the fin parameters for the standard Army-Navy fin configuration, where Table 24 summarizes the Mach number dependent fin aerodynamic data. Note that parameters e_i and f_i have been normalized by the fin chord length c, which can be used to scale fin size at a constant aspect ratio. For the standard fin configuration $c = D$.

Table 23: Summary Standard Finner Fin Parameters

Canard 1	**Canard 2**
$\Delta SL_{C_1} = SLCG - D\left(\frac{f}{c}(Ma)\right)$ (ft)	$\Delta SL_{C_2} = SLCG - D\left(\frac{f}{c}(Ma)\right)$ (ft)
$\Delta BL_{C_1} = D\left(\frac{e}{c}(Ma)\right)$ (ft)	$\Delta BL_{C_2} = 0.00$ (ft)
$\Delta WL_{C_1} = 0.00$ (ft)	$\Delta WL_{C_2} = D\left(\frac{e}{c}(Ma)\right)$ (ft)
$\phi_{C_1} = 0.00$ (deg)	$\phi_{C_2} = 90.0$ (deg)
$\delta_{C_1} = 0.00$ (deg)	$\delta_{C_2} = 0.00$ (deg)
Canard 3	**Canard 4**
$\Delta SL_{C_3} = SLCG - D\left(\frac{f}{c}(Ma)\right)$ (ft)	$\Delta SL_{C_4} = SLCG - D\left(\frac{f}{c}(Ma)\right)$ (ft)
$\Delta BL_{C_3} = -D\left(\frac{e}{c}(Ma)\right)$ (ft)	$\Delta BL_{C_4} = 0.00$ (ft)
$\Delta WL_{C_3} = 0.00$ (ft)	$\Delta WL_{C_4} = -D\left(\frac{e}{c}(Ma)\right)$ (ft)
$\phi_{C_3} = 180$ (deg)	$\phi_{C_4} = 270$ (deg)
$\delta_{C_3} = 0.00$ (deg)	$\delta_{C_4} = 0.00$ (deg)

Table 24: Summary Standard Finner Fin Parameters

Ma	C_{D_o}	C_{L_α}	e/c	f/c
0.01	0.043196899	3.864198234	0.6384	0.899410325
0.4	0.043687773	4.321947918	0.7189	0.898935912
0.6	0.043943027	4.556683794	0.7602	0.89873009
0.7	0.052150438	4.854114079	0.8219	0.899220818
0.75	0.056273778	5.002829221	0.8527	0.899442685
0.8	0.060377484	5.151563998	0.8835	0.899654213
0.85	0.069213213	5.387654686	0.9223	0.900152426
0.875	0.073631078	5.505680395	0.9416	0.900389
0.9	0.078048942	5.623706104	0.961	0.90061171
0.925	0.080994186	5.743440054	0.9804	0.900714011
0.95	0.083939429	5.863174004	0.9999	0.900808405
0.975	0.086884672	5.983025764	1.0195	0.900897428
1	0.089829915	6.102877524	1.039	0.900986517
1.025	0.090202979	6.216662083	0.948	0.900891432
1.05	0.090576043	6.330446642	0.857	0.900803198
1.1	0.083448555	6.569266588	0.675	0.900090161
1.2	0.074121952	6.135118118	0.6323	0.899815441
1.35	0.068192196	5.379800705	0.5969	0.900079663
1.5	0.063322727	4.596208957	0.5645	0.900566027
1.75	0.056745017	4.397719206	0.562	0.900178227
2	0.05350525	2.957436419	0.5269	0.902479601
2.25	0.050324387	2.693189207	0.5232	0.902746672
2.5	0.04712389	2.4290009	0.5195	0.903060797
3	0.042706025	1.924794914	0.507	0.904298607
3.5	0.040860339	1.537986319	0.5035	0.90623344
4	0.039034289	1.151158088	0.4999	0.909467086

REFERENCES

[1] "Prodas v3 technical manual," tech. rep., Arrow Tech.

[2] Blosser, O. K., "Naval surface fires and the land battle," *Field Artillery*, pp. 41–45, September-October 1996.

[3] Burchett, B. and Peterson, A., "Prediction of swerving motion of a dial-spin projectile with lateral pulse jets in atmospheric flight," *Mathematical and Computer Modeling*, vol. 35, no. 1-2, pp. 1–14, 2002.

[4] Carlucci, D. and Jacobson, S., *Ballistics: Theory and Design of Guns and Ammunition*. CRC Press, 2007.

[5] Cobb, K. K. and Whyte, R. H., "Effects of moving components on the motion of a 20-mm projectile," 11th AIAA Aerodynamics Testing Conference, New York, pp. 94–103, 1983.

[6] Cooper, G., "Influence of yaw canards on the yaw growth of spin stabilizxed projectiles," *Journal of Aircraft*, vol. 38, no. 2, pp. 266–270, 2001.

[7] Cooper, G. and Fresconi, F., "Flight stability of an asymmetric projectile with activating canards," AIAA Atmospheric Flight Mechanics Conference, Toronto, CA, May 2010.

[8] Costello, M., "Range extension and accuracy improvement of an advanced projectile using canard control," AIAA Atmospheric Flight Mechanics Conference, Baltimore, MD, 1995.

[9] Costello, M., "Extended range of a gun launched smart projectile using controllable canards," *Shock and Vibration*, vol. 8, no. 3-4, pp. 203–213, 2001.

[10] Costello, M. and Anderson, D., "Effect of internal mass unbalance on the terminal accuracy and stability of a projectile," in *Proceedings of the 1990 AIAA Flight Mechanics Conference*, pp. 29–31, July, San Diego, CA.

[11] Costello, M. and Peterson, A., "Linear theory of a dual-spin projectile in atmospheric flight," *Journal of Guidance, Control and Dynamics*, vol. 23, no. 4, pp. 789–797, 2000.

[12] Dupuis, A., "Aeroballistic range and wind tunnel tests of the basic finner reference projectile from subsonic to high supersonie velocities," tech. rep., Defense Research and Development Canada ValcartierD Canada Valcartier, October 2002.

[13] Dykes, J. and Costello, M., "Use of micro spoilers for control of finned projectiles," AIAA Atmospheric Flight Mechanics Conference, Toronto, CA, 2010.

[14] Etkin, B., *Dynamics of Atmospheric Flight*. Dover, 2005.

[15] Fink, R. D., "The usaf stability and control datcom," *Air Force Wright Aeronautical Labs.*, pp. TR–83–3048, April 1978.

[16] Franklin, G. F. and Powell, J. D., *Feedback Control of Dynamic Systems*. Prentice Hall, 6 ed., 2005.

[17] Fresconi, F. and Brown, T., "Very affordable precision projectile system and flight experiments," Proceedings of the 27th Army Science Conference, Orlando, FL, 2010.

[18] Ginsberg, J., *Engineering Dynamics*. New York, NY: Cambridge University Press, 2008.

[19] Grubb, N. D. and Belcher, M. W., "Excalibur: New precision engagement asset in the warfight," *Fires*, pp. 14–15, October-December 2008.

[20] Guidos, B. and Cooper, G., "Closed form solution of finned projectile motion subjected to simple in-flight lateral impulse," *AIAA Paper 2000 0767*, 2000.

[21] Hodapp, A. E., "Passive means for stabilizing projectiles with partially restrained internal members," *Journal of Guidance, Control and Dynamics*, vol. 12, no. 2, pp. 1–11, 1989.

[22] Hodapp, A. E., "Effect of mass asymmetry on ballistic match of projectiles," *Journal of Spacecraft and Rockets*, vol. 31, no. 1, pp. 130–134, 1994.

[23] McCoy, R. L., *Modern Exterior Ballistics*. Atgen, PA: Schiffer Military History, 1999.

[24] Miller, R. and Michel, A., *Ordinary Differential Equations*. Dover, 2007.

[25] Montalvo, C., "Effect of canard stall on projectile roll and pitch damping," *Journal of Aerospace Engineering*, vol. 225, 2011.

[26] Moore, F. G. and Moore, L. Y. AIAA Aerospace Sciences Meeting Including The New Horizons Forum and Aerospace Exposition, Orlando, FL, 5 - 8 January 2009.

[27] Moore, F. G., *Approximate Methods for Weapon Aerodynamics*, vol. 186 of *Progress in Astronautics and Aeronautics Series*. Naval Surface Warfare Center: AIAA, 2000.

[28] Moorhead, J. S., "Precision guidance kits (pgks): Improving the accuracy of conventional cannon rounds," *Field Artillery*, pp. 31–33, January-February 2007.

[29] Morrison, P. H., "A lesson learned about cannonlaunched guided projectiles," *Journal of Guidance, Navigation, and Control*, vol. 3, pp. 154–157, April 1980.

[30] Morrison, P. H. and Amberntson, D. S., "Guidance and control of a cannon-launched guided projectile," *Journal of Spacecraft and Rockets*, vol. 14, pp. 328–334, June 1977.

[31] Murphy, C. H., "Free flight motion of symmetric missiles," Tech. Rep. 1216, Ballistic Research Laboritories, Aberdeen Proving Fround, MD, July 1963.

[32] Murphy, C. H., "Symmetric missile dynamic instabilities: A survey," 18th AIAA Aerospace Sciences Meeting, January 1980.

[33] Murphy, C. H., "Instability of controlled projectiles in ascending or descending flight," *Journal of Guidance and Control*, vol. 4, no. 1, pp. 66–69, 1981.

[34] Murphy, C. H., "Angular motion of a spinning projectile with a viscous liquid payload," *Journal of Guidance, Control and Dynamics*, vol. 6, pp. 280–286, July-August 1983.

[35] Ollerenshaw, D. and Costello, M., "Model predictive control of a direct fire projectile equipped with canards," *Journal of Dynamic Systems, Measurement, and Control*, vol. 130, 061010-1 – 061010-11, September 2008.

[36] Prasad, J. V. R., "Aerospace engineering class lecture notes." Georgia Institute of Technology.

[37] Rogers, J. and Costello, M., "Design of a roll-stabilized mortar projectile with reciprocating canards," *Journal of Guidance, Control and Dynamics*, vol. 33, July-August 2010.

[38] Smith, J. A. and Smith, K. A., "Feasibility study for application of modular guidance and control units to existing icm projectiles," *U.S. Army Armament Research and Development Command*, ARLCD-CR-79001, November 1978.

[39] Soper, W. G., "Projectile instability produced by internal friction," *AIAA Journal*, vol. 16, no. 1, pp. 1–11, 1978.

[40] Stang, G., *Linear Algebra and Its Applications*. Brooks Cole, 4 ed., 2005.

[41] Szidarovsky, F. and Bahill, A. T., *Linear Systems Theory*. CRC Press, 2nd ed., 1998.

[42] Tang, L. and Liu, D. D., "Extension of projectile range using oblique-wing concept," *Journal of Aircraft*, vol. 44, pp. 774–779, May-June 2007.

[43] Weber, D. J., "Simplified method for evaluating the flight stability of liquid-filled projectiles," *Journal of Spacecraft and Rockets*, vol. 31, no. 1, pp. 130–134, 1994.

[44] YAGER, J. K. and FROYSLAND, J. L., "Improving the effects of fires with precision munitions," *Field Artillery*, pp. 5–7, March-April 1997.